POLITECNICO DI TORINO

MASTER THESIS

Metal Oxide gas sensors for Volatile Organic Compounds detection

---

Author:
Giulio TIDEI

Supervisors:
Dr. Andrea FASOLI
Prof. Carlo RICCIARDI

*A thesis submitted in fulfillment of the requirements
for the degree of Nanotechnologies for ICTs*

in the

Sensing Group
IBM Almaden Research Center

October 13, 2019

POLITECNICO DI TORINO

Abstract

Department of Applied Science
IBM Almaden Research Center

Nanotechnologies for ICTs

Metal Oxide gas sensors for Volatile Organic Compounds detection

by Giulio TIDEI

The ability to detect, distinguish and categorize odors finds valuable uses in several fields such as automotive, industrial safety and consumer products. Volatile Organic Compounds (VOCs) are of particular relevance in these fields, as key components of many complex mixtures of gases to be detected. The electronic nose (e-nose) is a device which mimics the functionalities of the human nose through an array of gas sensors coupled with machine learning algorithms. One class of sensors used to detect low gas concentrations are the metal-oxide-semiconductor (MOX) gas sensors, sensors which change their conductivity upon gas exposure. This family of devices are generally made of a single material and are not characterized by an excellent selectivity with respect to different gases; moreover they suffer additional problems like long term stability and interference from the environment. Recent results reported in the literature show however how a combination of MOX materials can improve both selectivity and sensitivity, key figure of merit of sensor performance. Nevertheless reported results were obtained through geometries difficult to integrate and hard to produce on an industrial scale. The aim of this work is to investigate the effect of thickness and annealing processes on the performance of MOX bilayer gas sensor devices. The devices were fabricated by DC sputtering with a geometry which aims to an easy integrability. In the first part of the thesis the general theory of e-nose and gas sensor devices is discussed, with particular attention to the latest results in MOX gas sensing technology. Then, the fabrication and testing processes of the devices are fully described. At the end, the thickness and annealing experiments are described. Results show that a remarkable improvement in device response to VOCs can be achieved. It is also shown how different annealing techniques impact the device morphology in order to choose the optimal one in the devices fabrication.

Acknowledgements

First, I would like to express my gratitude to my advisor Andrea Fasoli who, with his positivity and his spontaneity has continuously supported me through this project. Thanks to him I have learned an approach to research and technology which I will cherish for the present and for the future. Besides my advisor, I would like to thank my close colleagues Lisa Thornquist and Gabriele Tombesi who with their skills and knowledge have been fundamental in this project. I would like to thank my manager Luisa Bozano who gave me the opportunity to join this project and has been since the first moment available for any help. My sincere thanks also goes to my colleagues Alberto Mannari, Ron Labby for the technical help and to Linda Sunberg, Krystelle Lionti, Gabriele Gatani and Theophile Dubrueil for the sol-gel part of the project. I thanks Amy e Charlie for the help in cleanroom, Teya Topuria, Lisa Lofano, Holt Bui, Anthony Fong and the whole characterization group for the analysis of my samples. A special thanks to the whole IBM Almaden Research Center for the wonderful experience.

Contents

List of Figures

List of Abbreviations

MOX Metal Oxide Semiconductor
VOC Volatile Organic Compound
ARC Almaden Research Center
SAW Surface Acustic Wave
QCM Quartz Crystal Microbalance
SNR Signal to Noise Ratio
MOSFET Metal Oxide Semiconductor Field Effect Transistor
MS Mass Spectrometry
IMS Ion Mobility Sepctrometry
GC Gas Chromatography
IR Infrared Spectroscopy
ANN Artificial Neural Network
TDC Thermal Conductive Detectors
NW Nanowire
PR Phororesist
PVD Physical Vapor Deposition
VLS Vapor Liquid Solid
MFC Mass Flow Controller
RBS Rutherford Backscattering Spectrometry
XRD X-ray Diffraction
XPS X-ray Photoelectron Spectroscopy
SEM Scanning Electron Microscope
TEM Transmission Electron Microscope
EELS Electron energy loss spectroscopy
RTA Rapid Thermal Annealing
HP Hot Plate Annealing
OA Oven Annealing
IDE Interdigitated Electrode

Chapter 1

Introduction & working enviroment

The objective of this work is to report on the results of the 6 months fabrication, characterization, and testing activity of Metal Oxide gas sensing devices to be integrated in an electronic nose (e-nose): a device able to distinguish and categorize odors. The development of this odor-detecting platform is performed in the Sensor Group at the IBM Almaden Research Center (ARC) where I have carried out my activity.

Existing technologies will be discussed together with the current and future applications and markets. The fabrication process of the sensor will be illustrated together with testing setup and protocols. Physics and engineering of the device will be explained in the context of recent literature results. Most importantly, the experimental objectives and results obtained will be shown and discussed.

1.1 Gas Sensors Project

Development of devices able to detect and categorize odors is equally driven by market needs and by the progress in recent years of nanoscale fabrication technology as applied to gas sensors, in terms of control of the nanoscale properties of the materials. Examples of gas sensing applications are: toxic gases detection (Wilson, 2012, Tsow et al., 2010), food and beverage quality check (Natale et al., 2003, Cocina et al., 2012), military scopes (Goschnick and Harms, 2002), air quality monitoring (Zhang et al., 2012, Leidinger et al., 2014) and healthcare (Natale et al., 2003). Several examples of electronic nose or odor detecting devices are present in the market (figure A.1). It is important to stress that there is no clear boundary between lab analytical systems, electronic nose and specific substance detectors; some manufacturers avoid the term electronic nose to define their odor detecting product (Rock et al., 2008).

Despite the wide availability of products, no commercial breakthrough thus far (Rock et al., 2008) enabled a general purpose device delivering suitable odor identification performance across all these fields. For this reason, Sensor Group is working at the development of a several purpose electronic nose, which is able to fully categorize odors in a smart, faster, cheaper and portable way.

Sensor Group is part of the IBM Almaden Research Center (ARC) set in San Jose California, where they work at the level of research to the implementation of this device. The team is composed of physicists, chemists, engineers and scientists in general developing all the aspects of the device. For what concern the devices, they are fabricated in a cleanroom environment as well as various chemical and testing labs where, materials synthesis and characterization take place. Testing in the labs allow to correlate the devices performances and features with the different properties of the device (morphology, crystallinity, composition) and to model and explain the undergoing mechanisms. Data acquired from the testing are analyzed and processed with different methodologies and algorithms in order to find the most efficient model capable to distinguish the odors out of the sensing results.

1.2 Gas Sensors Overview

In general, several types of gas sensors can be integrated in an electronic nose, in order to leverage their individual advantages. At a high level, these sensors share a common mechanism for detection: a gas interacts with the sensing material by adsorption, absorption or chemical reaction, a change of a physical and/or chemical property of the material takes place, such change is then transduced to an electrical signal (Arshak et al., 2004). In the following sections, the different gas sensing technologies categorized according to their working principle.

1.2.1 Conductometric

In general these devices are based on the change of the electrical conductivity of the sensing material upon exposure to gas/odors. Depending on the mechanism which lead to the change of this conductance (or resistance) it is possible to distinguish three different categories: Conducting Polymer Composite sensors, Intrinsically Conductive Polymeric sensors and Metal-Oxide-Semiconductor sensors (Arshak et al., 2004). All these conductometric gas sensors can benefit from similar device geometries, as shown in figure 1.1.

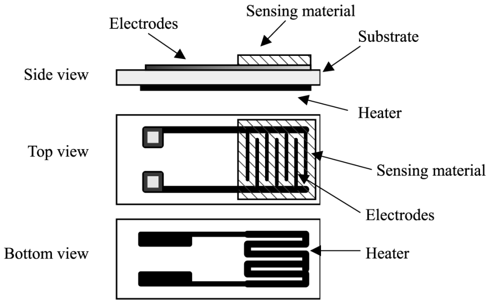

FIGURE 1.1: General structure of a conductometric gas sensor.

Interdigitated electrodes are deposited on a substrate and are used to measure the conductance change on the sensing layer which is deposited on top of it (and in direct contact with the gas/odor on the other side). Microheaters are instead placed below the substrate and electrically driven to bring the sensor to the operating temperature; indeed for some conductometric gas sensors a temperature higher than the ambient one (around 300°C) is necessary for the correct functioning of the device.

Conducting Polymer Composite gas sensors have a sensing layer made of conducting particles interspersed into an insulating polymer matrix (Albert et al., 2000). In such a structure conduction occurs due to percolations effects of these particles. When the polymer gets in contact with the gas some of this permeate into the matrix expanding it, this expansion reduces the number of percolating paths changing the resistance (Muñoz et al., 1999). For some materials there is a similar but more complex mechanism, this is the case of polypyrrole filled composite where even the polypyrrole conducting particles are influenced too from the gas. This conductometric gas sensing category has in general a good response time (Muñoz et al., 1999) and can achieve high discrimination due to the large variety of polymers available in the market (Arshak et al., 2004). While fabrication of such organic devices is in general easy and cheap, at the same time they suffer from aging, drift, temperature and humidity. In addition, a valuable feature is that the operating temperature is low, which limits the power consumption.

Unlike Conducting Polymer Composite sensors, in the Intrinsically Conducting Polymers conduction of the sensing layer does not occur through the particles interspersed into the polymer but through the polymer itself: more precisely along the polymer chains and between the polymer chains. Depending on the material used these polymers can be conducting or semiconducting, either n-type or p-type. Conductivity of the polymer interacting with the gas can occur in three different ways (Albert et al., 2000): interchain conductivity (within the chain), intermolecular conductivity (from chain to chain) and ionic conductivity (movement of an ion from one site to another). Similarly to the Conducting Polymer Composite technology, these devices have in general good response time (Arshak et al., 2004), cheap and easy fabrication, but low reproducibility and suffer from drift, aging, humidity and temperature (Albert et al., 2000). Still the low temperature allow low power consumption and the large variety of polymers available in the market make them interesting candidates to target a wide range of gases (Albert et al., 2000). In this regard a fundamental property of polymers is the possibility to tune their interaction to various gases, enhancing a fundamental property of the device called "selectivity".

Metal Oxide (generally referred as MOX or MOS) sensors take advantage of the ability of the sensing layer material to interact with the gas via redox reactions. Sensors can be n-type (electrical conduction occurs through electrons) or p-type (electrical conduction occurs through holes). In the absence of gas the sensing material conduction take place thanks to the presence of defects and oxygen vacancies, when the material is open to ambient air, oxygen (either molecular or atomic) can interact with the metal oxide surface and trap the electrons out of the conduction band of the conducting metal oxide resulting in a larger (p-type) or smaller (n-type) conductance compared to the oxygen-less case (Arshak et al., 2004). In a n-type sensor when a reducing gas reaches the sensing material it reacts with the oxygen releasing the electrons which become newly available for the conduction increasing correspondingly the conductivity of the sensing layer. Conversely if an oxidizing gas reaches the sensing material it will trap electrons too as the oxygen, decreasing correspondingly the conductivity of the sensing layer. For a p-type sensors the behavior is the opposite, indeed for a reducing/oxidizing gas there is a decreases/increases of the sensing layer conductivity. A deeper discussion of the conduction mechanism will follow in the next chapter. This category of devices are characterized by a really fast response, the price to pay are operating temperatures that can exceed 300°C. Really low detection limits can be reached but due to the detection mechanism, selectivity is not particularly good; an adopted solution is generally doping (Arshak et al., 2004). Fabrication is relatively easy and cheap.

In general conductometric gas sensors have all a good integrability and require simple circuitry. While the polymeric ones have low operating temperature and not excellent detection limits (ppm) opposite is for the MOX where detection limit can reach the ppb level but operating temperatures are elevated.

1.2.2 Piezoelectric

Surface Acoustic Wave (SAW) and Quartz Crystal Acustic Wave (QCM) devices are part of the category of piezoelectric gas sensors; in these devices the piezoelectric sensing layer absorbs the gas, thereby increasing its mass which change accordingly the resonant frequency of the structure (Arshak et al., 2004, Albert et al., 2000).

In SAW devices, on a piezoelectric substrate (generally ZnO) are deposited two transducers (input and output, Khlebarov et al., 1992), between them is placed the gas sensing layer (generally polymeric). The AC signal applied to input traducer to generate a wave which travel through the surface to the output transducer (Pearce, 2003). A gas interaction with the sensing layer generate the following change of frequency:

$$\Delta f = \frac{\Delta f_p c_v K_p}{\rho_p}$$

Here Δf_p is the change of frequency due the sensing layer, c_v is the gas concentration, K_p is the partition coefficient and ρ_p is the density of the polymeric membrane (Albert et al., 2000). These devices are characterized by a low detection limit and a good response in general; fabrication is easy because of the planar structure. The circuitry required is not simple (Pearce, 2003), they have a low SNR (due to the operating frequencies, Arshak et al., 2004) and reproducibility is hard to achieve (Arshak et al., 2004). Large variety of coatings available allow these devices to respond to a broad spectrum of gases.

QCM sensors are equal to the SAW except for the fact that wave propagation is not limited to the surface but travel through the entire bulk. When a voltage is applied the quartz, this starts to oscillate at a resonant frequency generally between 10 and 30 MHz (Schaller et al., 1998). Sensing layer is deposited on the surface of the crystal, adsorption of the gas on this generate a shift in the resonant frequency which is measured on the side of the quartz disk (Albert et al., 2000). Corresponding sensitivity is:

$$\frac{\Delta f}{\Delta c} = \frac{-2.3 * 10^{-6} f^2}{A}$$

Here f is the fundamental frequency, c is the concentration and A is the area of the sensitive film (Carey and Kowalski, 1986), a smaller area and a higher frequency determine a higher sensitivity. These devices have the characteristic to be selective and sensitive (Pearce, 2003), their geometry complicates the fabrication process and interface circuitry (Schaller et al., 1998); additionally they have a poor SNR and a low reproducibility (Schaller et al., 1998).

1.2.3 Optical

Optical sensors are based on the change of optical properties. In the most common configuration an optical fiber is used, which, is coated at the tips or at the sides with a fluorescent dye encapsulated in a polymer matrix (Arshak et al., 2004, Schaller et al., 1998). When the gas gets in contact with the fluorescent dye, it alters its polarity thereby changing the optical properties of the coating such as: intensity, spectrum, lifetime or wavelength fluorescence. These sensing devices are in general characterized by a very fast response, less than 10 s overall between sensing and analysis (Walt et al., 1998). At the same time associated circuitry is rather complex making them more expensive compared to the other gas sensing technologies (Nagle and Schiffman, 1998).

1.2.4 MOSFET

Metal-Oxide-Semiconductor Field-Effect-Transistor sensors are based on same the technology of the most common transistors used in both analog and digital electronics applications. Differently from the MOX gas sensors where the sensing material has the characteristics of being a metal-oxide and a semiconductor, the MOS acronym refers to the stack of metal-oxide-semiconductor layers of the structure. As a general functioning in this devices the threshold voltage of the devices change upon interaction of the gate with the gas (Pearce, 2003). This is possible either functionalizing the gate metal with a polymer or using as gate metal a catalytic metal which change its work function on exposure with the gas (Pearce, 2003). These devices have a good reproducibility, an easy to CMOS technology incorporation (Arshak et al., 2004) and a cheap fabrication process. Response time can be decreased through high temperature operation and the main disadvantage is the baseline drift (Nagle and Schiffman, 1998).

1.2.5 Analytical techniques

General analytical lab techniques can be applied to gases too for identification.

This is the case for Mass Spectrometry (MS) a well known technique based on the mass-to-charge ratio of ions, generally applied in labs analysis to identify chemicals, both individual gases and mixtures. Compounds gets ionized either chemically by interaction with reagent ions or removing electrons thermoionically. Ions derived are then separated according to their mass-to-charge ratio by means of an electric and/or magnetic field and are measured after a electron multiplier amplification (Rock et al., 2008). Such technique guarantees high precision and accuracy, the price to pay is of course in terms of money and the bulky apparatus. For a compound prior to Mass Spectrometry no chromatographical step is applied (no mixture separation into the components), mass-to-charge ratio spectrum can however be treated as recognizable pattern (Rock et al., 2008).

Ion Mobility Spectrometry (IMS) is similar to MS from the fact that ions are filtered, this time according to their mobilities. Indeed different size and shape determine different collisions influencing the separability of the ions (Rock et al., 2008, Creaser et al., 2004). Characteristic is the fact that since the collisions with ambient air is used the measurement does not need a vacuum condition as in mass spectrometry. After ionization, the ions in a tube are accelerated by an electric field colliding or reaching the detector at the end of the tube. Out of the impact a current is measured deriving the corresponding time of flight.

A further chemical analytic technique to detect gases is Gas Chromatography (GC). Mobile gas phase transport the sample on the surface of the stationary phase which is solid or liquid and is placed onto the walls of a column, the gaseous compound interact with this latter phase and depending on the physical and chemical properties, a different retention times for the different components separates the parts of the compound (Rock et al., 2008). Ultrafast mode is possible in the cases of the real time gas detection, indeed changing different parameters is possible to change the separation speed of the analysis.

Common Infrared Spectroscopy (IR) is a further analytical technique in which, through the interaction of infrared light with the compound molecular, vibrations and higher energy levels are excited (Rock et al., 2008). Out of this interaction absorption bands define the chemical bonds. The spectrum generated represents a unique fingerprint of the substance which can be further analyzed with pattern recognition algorithms. Two affordable methods for mobile devices are possible. Photoacustic infrared spectroscopy where intensity modulation of an IR contract or expand the gas by means of the temperature variation: this gas extension or contraction is measured through a microphone. In the second technique the absorbed energy derived from a narrow spectrum of the IR is determined.

1.3 Goal & Innovation of this Work

As seen in the previous section MOX gas sensors have good sensing characteristics except for the selectivity, this is due in general to the similar interaction of the sensing layer with the different gases. Usually these sensors consist of a single material (most commonly n-type), often with the addition of doping in order to improve performances; this approach however does not give always an optimal results (Tricoli et al., 2008, Lu et al., 2006). Recent results in literature have shown that is possible to achieved good performances combining a n-type and p-type materials on the same sensing device. In particular through decoration of an n-type sensing structure (layer, nanorod, nanowire,...) with p-type nanostructures (Kim and Lee, 2014, Na et al., 2012b, Kim et al., 2011a). What it is suspected is the enhancement of the otherwise single material device through two sensitization effects: Chemical Sensitization and Electronic Sensitization. Research activity described in this work focused on the investigation of these structure, targeting the enhancement effects of the literature through a manufacturable fabrication technique such as sputtering. Devices with $SnO_2(n-type)/NiO(p-type)$ bilayers have consequently been studied from the performance and morhology point of view. In the first experimental part a systematic thickness analysis of the sensing film was performed. Devices of different thicknesses of SnO_2 and NiO were fabricated, characterized (SEM, XPS, TEM) and tested. Results showed that for a specific thicknesses of NiO deposited on top of SnO_2 the response magnitude of the latter can be effectively be improved. In the second experimental part, for two different combinations of thickness of the $SnO_2(n-type)/NiO(p-type)$ bilayer the impact of annealing on the films physical and sensing properties was investigated. Annealing represents a powerful technique in the metal-oxide fabrication, especially because of its effect on the film morphology. Several nominally equivalent sensing layers were deposited and have undergone different annealing processes for different temperatures and time. The corresponding results were analyzed with conventional characterization technique like SEM and XRD to identify which process gives the most useful morphological configuration.

1.4 Thesis Content

In the current section (Chapter 1) a general overview of the student project was presented with an introduction to the Gas Sensors Project and the working environment. Existing gas sensors technology were introduced, followed by the objective of the project. In Chapter 2 electronic nose working principles and theory are discussed, including a brief description of multivariate analysis. Chapter 3 explains in details the history, working principle and challengers of MOX gas sensors. At the end of the chapter recent relevant results on this class of devices are introduced. What follows in Chapter 4 is a full description of the devices fabrication and testing procedures. Experiment on the thickness systematics is first covered, from the objectives to the results in Chapter 5. Chapter 6 shows the annealing systematics experiment with the results which follow the motivations and the approach of the experiment. Finally Chapter 7 draws conclusions about the results in general and the benefits brought to the Gas Sensors Project.

Chapter 2

Electronic Nose

As mentioned in the previous chapter (Chapter 1) the Sensor Group is working at the development of an electronic nose (e-nose), a device able to detect, categorize and recognize odors. In this chapter is shown how through biological inspired engineering and sensing technology the concept of e-nose was born to respond to an increasing market in the field of odor detection.

2.1 Applications and market

Reasearch on the possibility to recognize and detect odor in general is driven by several markets (1.1). One of the main potential field for electronic nose ability is food and beverage, where it can applied for qualitative inspection of ingredients and manufacturing process supervision (Rock et al., 2008). Distinction between different quality products is fundamental to protect both customers and quality producer: this is the case for example of olive oil for which is of fundamental importance to distinguish between regular, virgin or extravirgin olive oil (Rock et al., 2008). Another relevant question is the type of ingredients present within a product, even if the product content is supposed to be specified in the label it is fundamental to verify if the producer effectively respects the law (Rock et al., 2008): a simple example regards the feta cheese which is supposed to contain only goat and/or sheep milk only. Fraud to the customer is not the only possible application in food industry, e-nose can highly contribute in the production process monitoring to detect irregularities, detecting off-odors, off-flavors or in some cases harmful substances (Rock et al., 2008). An interesting application is certainly food spoilage (Rock et al., 2008); preservation technique are of course well known and used nowadays, but the possibility to detect of or eventually predict food spoilage is certainly interesting (Dainty, 1996).

Increased awareness on environmental pollution and its effect on the human health has boosted the necessity of sensors for environmental monitoring (Rock et al., 2008). Toxic compounds are regularly present in the everyday environment in concentrations which calls for close, continuous monitoring. Monitoring of substances is done both at the source and a the place where people live. Some of these are: nitrogen oxides, carbon monoxide, ammonia and volatile organic compounds (VOCs) (Rock et al., 2008).

In particular, this last family of substances generates concern because of the potential negative effects derived from long exposures, including skin irritation (Jones, 1999) and sickbuilding syndrome (Brinke et al., 1998, Burge, 2004). The monitoring of VOCs has become of increasing importance in all the environments with particular strict conditions for indoor air quality. Currently monitoring is performed either by human panel olfactory measurements or analytical instrument, this of course bring high operating costs and not-real time monitoring (Nagle and Schiffman, 1998).

Practical examples of detection are smoke compounds for automotive ventilation, odorous emission from industrial factories (Rajamaki et al., 2005), animal production facilities (Nimmermark, 2001) or even waste disposal sites (Micone and Guy, 2007).
Possibility to diagnose diseases by smell is something which is considered in several traditional medicines. The electronic nose represents from this point of view an ideal device for health monitoring in some cases, working on diagnosis of infections, intoxications and metabolic diseases through the markers (Rock et al., 2008). Several clinical research results have shown the potential of th e-nose for a large variety of diseases through analysis of swabs, sputum, serum or urine; several further diseases can be detected through skin, sweat and breath. In particular, in breath analysis fishy breath can be associated to uremtia patients, feculent odor may derive from intestinal obstruction and diabetes can be correlated to sweet fruity smell. The main advantage of the electronic nose in diagnosis is without any doubt the speed and the non invasivity (Rock et al., 2008).

2.2 Selectivity

As described in Chapter 1 the structure of gas sensors is simple if compared to analytical systems such as Gas Chromatography, Mass Spectroscopy, Ion Mobility Spectrometry, Infrared Spectrometry or even human sensory panels. Indeed while the first techniques (GC, MS, IRS, IR) are slow, bulky, and expensive, human-based methods does not give optimal results since they are subject to variations from person to person (Pearce, 2003, Nagle and Schiffman, 1998). At the same time, individual gas sensors tends to lack selectivity (ability to respond differently to different gases), since the pathways of interaction with different gases are often similar. High selectivity can be achieved but in most part of the cases is inversely related to reversibility of the interaction to which can correspond an increased long term drift (Reimann and Schütze, 2013). To overcome this generic problem two solutions are in general used: Multivariate Analysis and Multisensor Arrays (electronic nose).

2.3 Multivariate analysis

In this approach still an individual gas sensor is used, this time with a multivariable transducer with different fully o partially independent outputs. To these outputs correspond a response pattern which is then analyzed by a pattern recognition algorithm which relate it to the specific odor detected (Potyrailo, 2016). Fundamental for the sensing material is to have diverse vapor response mechanisms to be probed, by the multivariable transducer. The number of independent outputs (sometimes defined as dispersion or dimensionality) it is fundamental and determine the performance capabilities of the device. If a single output is used, this corresponds to a one-dimensionality, in this case, even if two gases give different responses for different concentrations their discrimination is not possible. This is shown in case A) of figure 2.1. If more than one output is used then each gas has its own response direction, as you can see in case B) of figure 2.1, this, allows a better discrimination between closely related analytes and interference from the environment (Potyrailo, 2016). If the dimensionality is increased, this discrimination capability of the device increases further.

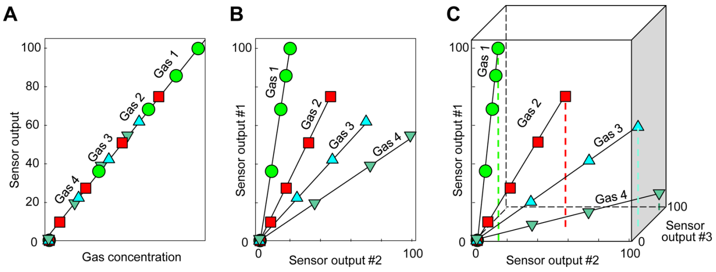

FIGURE 2.1: Comparison of responses for different gases and a different number of outputs for a multivariable sensor. (A) One output case, (B) Two outputs case, (C) Three outputs case. Adapted from Potyrailo, 2016.

For metal oxides gas sensors for example, discrimination can be obtained using resistance and capacitance change as outputs. This is shown in figure 2.2, for the cases of a In_2O_3 sensors measured at 1 kHz for Acetone (C_3H_6O), CO, NH_3, NO and NO_2.

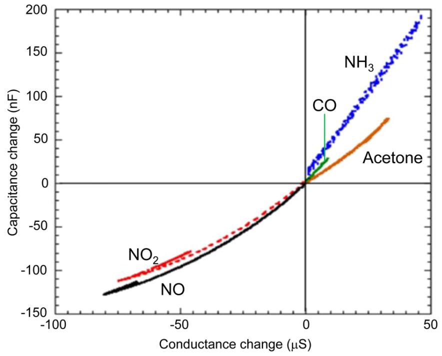

FIGURE 2.2: Gases discrimination in a In_2O_3 sensing device through resistance and capacitance change measurement at 1 kHz. Adapted from Potyrailo, 2016.

To further improve the discrimination it is possible to increase the dimensionality (number of outputs), adding for example the surface work function measurement and the adsorption-induced stress measurement (Potyrailo, 2016). A further idea behind this approach regards the stability of the measurement, indeed in this case any eventual drift in the measurement comes from a single device only, as a consequence is limited and more controllable than the Multisensor arrays case.

2.4 Multisensor arrays (Electronic Nose)

Multisensor arrays (as the name specifies) is a configuration which consist of an array of different single gas sensors, based on the same or different working principles. As in the virtual multisensors, a pattern (fingerprint) is associated with an odor through pattern recognition algorithms. A Gas Multisensing Array is an alternative name to electronic nose (e-nose), which can even be defined as an electronic device which mimics the human nose abilities to recognize odors and categorize them (Reimann and Schütze, 2013). Examples of commercial e-nose and the integrated gas sensor devices is shown in figure A.1.
Mammalian olfactory system indeed as we know well, is highly sensitive and highly capable to distinguish odors, interesting pioneering work from this point of view is made from Persaud and Dodd, 1982.

2.4.1 Working Principles

In the work of Persaud and Dodd, 1982 first the mammalian olfactory system is described in the above simplified way, then a working device out of that is built capable to distinguish different odors, the described simplified system is the following (Shurmer and Gardner, 1992).
In the sensing mucosa around tens of millions of sensing cells are present reacting with the odorant molecules of the ambient. These are associated with 10-20000 primary neurones which synapse with the single secondary neurones situated in the olfactory bulb (other neurones types are however present which cross-connect the secondary neurones). Such parallel configuration suggests a corresponding electronic implementation of this architecture as the one shown in figure 2.3.

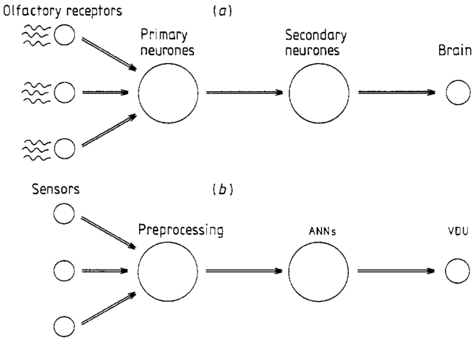

FIGURE 2.3: Schematic representation of (a) a biological nose and (b) electronic analogue. Adapted from Shurmer and Gardner, 1992.

In the electronic version of the nose the array of sensing cells (or olfactory receptors) is realized through the multisensor array made out of single gas sensing devices, the number of these is orders of magnitude lower than one in the human counterpart. Primary neurones are represented by a preprocessing level, here a simple processing like normalization and functions is realized by simple analog or digital electronics, this step is necessary to remove some dependency like in concentration. Finally the secondary neurones role is realized through the pattern recognition algorithm part.
In his work Persaud and Dodd, 1982 takes three different commercially MOX sensors and connect the output of each of them such that the ratio of the output signals remove the concentration dependence, which, can be separated form the information related to the type of odour. This final signals become the input of an artificial neural network (ANN).
Results showed how, thanks to the signal processing and choices of the designer, discrimination of odors is possible and partially maintained with time. The achieved result was without any doubt optimistic, in particular it was shown how since already in 1982 was possible to implement a device capable of mimic the mammalian nose and categorize odors. Despite this, still today many challenges are still on the field, which stop the electronic nose to show breakthrough results in the odors distinction and categorization.

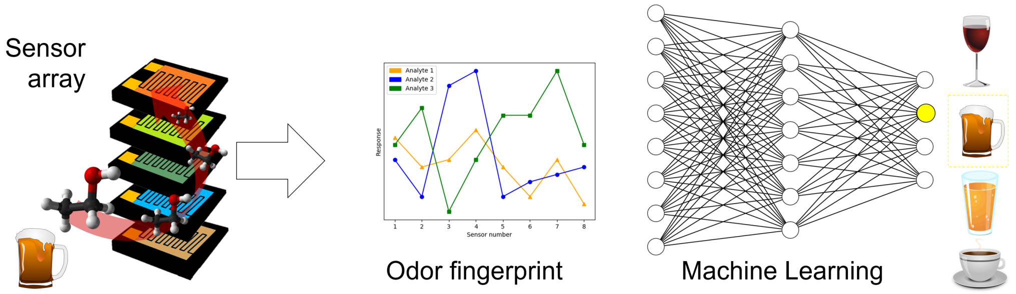

FIGURE 2.4: Simplified representation of electronic nose odor recognition process

As just discussed, at the base of the electronic nose architecture there are two main parts (a preprocessing part eventually matches the two): a sampling part realized by the sensor array and a data classification part realized by the pattern recognition algorithm. About the latter several methods are possible (multivariate regression, vectorial decomposition,..), but the most used (since Persaud and Dodd, 1982 and in particular nowadays) is Artificial Neural Network (ANN). The research of the best analytical technique is certainly important but it is out of the scope of this work.
For what concern the sensor array, it is necessary to feed the ANN in such a way that it can fully associate a response pattern to an odor (fingerprint), indeed multisensor array architecture solve the problem of single gas/odor sensing, only if single sensors which respond in a particular manner are used.
If odors A and B give the same output pattern scaled by a given factor this is problematic. What is first determined to be A can than be detected to be B in a second moment, because of different physical effect like humidity: even removing the intensity information the shape of the pattern does not allow us to differentiate the two. An important feature of the single sensors embedded in the e-nose is therefore their partial selectivity (ability to respond differently to different gases). Is important to remark however, that as a general rule the high selectivity of the single sensor implies a strong interaction of the sensor with the gas which correspond to long recovery times or signal drift. At the same time according to Persaud and Dodd, 1982, to have a correct analogous version of the human nose is fundamental the assumption, for the single gas sensors of the electronic nose, to respond to as many gases as possible.
Another fundamental features is that the single sensors in the array are different from each, in particular with different interaction mechanisms with the gas.
As mentioned before even in the e-nose single sensors stability is crucial, the ANN is trained for specific fingerprints, of course if the response of the devices changes over the time, an odor generated pattern will be different from the same in the past and consequently no longer recognizable. Barsan and Weimar, 2001 show for example how the humidity influences the behavior of CO to CuO (p-type) increasing its baseline resistance and decreasing its response.

2.5 Challenges

Gas sensors performance can be in general be assessed by three fundamental parameters: Sensitivity, Stability and Selectivity.

The word sensitivity defines in general the response magnitude of the gas sensor, this is in general different from the low detection limit which is the smallest value that the sensor is capable to measure; in all the cases both characteristics are requested in a good gas sensor. An example of the need to measure low gaseous concentrations is clear in the indoor air quality field (Schütze et al., 2017). Here the guidelines threshold concentrations (for these critical VOCs) reported from the World Health Organization (*World Health Organization. WHO Guidelines for Indoor Air Quality: Selected Pollutants*) and the European Union (*European Parliament, Council of the European Union: Directive 2008/50/EC of the European Parliament and of the Council of 21 May 2008 on Ambient Air Quality and Cleaner Air for Europe.*) are consistently low: 81 ppb for formaldehyde, 1.9 ppb for naphthalene and 1.6 ppb for benzene.

Ability to generate reproducible measurements over time is in general defined as stability. One of the main challenges in the gas sensing development is indeed the drift of the parameters, immediate consequence of the drift of the physical properties (Korotcenkov and Cho, 2011). While a potential solution would be the frequent substitution of the device, this represents however an expensive approach which cannot in some fields be always applied (i.e. space application). In addition to time stability, it is also crucial to guarantee reproducibility of the device output in various operating conditions, as different applications have indeed different working environments which embed different physical influences.

The last and most evident gas sensor parameter is ability to respond differently to different gas and odors. Whether the device is used to categorize odors or to detect a specific gas, this represents a crucial feature. A clear example is in alarm applications where false positives are undesirable or unacceptable (Reimann and Schütze, 2013). Additionally in a odor categorization we want to be sure to have a response uniquely associated to one odor and not a different one. Looking at the single sensors is often hard to distinguish the odors to different analyte, this since as already said, different gases might have similar interaction (Reimann and Schütze, 2013).

As previously described, different gas sensing technologies relies on different physical mechanism and principles to which different sensitivities, stability, sensitivity and other parameters correspond. Different fields of application can also express diverse needs and be characterized by different working conditions. It is consequently key for the gas sensor design to adapt to choose the most feasible technology for the target field of application. At the same time, designing a general gas sensing device meeting the needs of different fields is recommended too, getting the advantage of a device deployable to different markets. This is the case of this study and of the Sensor Group which aims at a general purpose gas sensing device.

2.6 Conclusions

This chapter discussed the technical choices driving the Sensing Group to move towards the development of a device like the e-nose, in order to satisfy the market of gas sensing and odor recognition. In particular the challenges shown in the last section show that research is required to overcome several roadblocks and realize an optimally working device.

Chapter 3

Metal oxide semiconductor gas sensors

As mentioned in Chapter 2 this family of devices is part of the larger family of conductometric gas sensing devices, devices which when exposed to a certain amount of gas change their conductance (or resistance). The physics behind this behavior is in general well known in literature and will be shown within this chapter, additionally several new interesting results from literature will be shown: representing a research pathway in which this work focused.

3.1 History of conductometric metal oxide sensors

First demostration of gas sensing property from a semiconductor comes from John Bardeen and Walter Brattain (Neri, 2015) (inventors of the transistor with William Shockley) which in 1953 in the Bell System Technical Journal (Brattain and Bardeen, 1953) showed the effect on the conductivity of a n-type Ge piece of semiconductor exposed to specific gases: ozone and peroxide vapors in their case. In 1962 (Seiyama et al., 1962) showed that by means of a ZnO thin film sensing layer, under certain temperature conditions gas detection was possible with an sensitivity 100 times better than the one of the standard technology of that time: thermal conductive detectors (TCD). After this work, investigations in this area continued without major breakthroughs until 1967 when Shaver (Shaver, 1967) brought to light the effects of noble metals (e.g. Pt, Pd, Ir, Rh) on oxide semiconductors. In his work Shaver uses a Tungsten-oxide thin film which define "activated" by the presence of platinum on the surface, the effect is an improvement of the sensitivity and of the response time of the sensor. From that moment there has been in general an improvement of the gas sensors selectivity and sensitivity to which has corresponded an expanding research of new formulations of the gas sensing materials. First commercial conductometric gas sensor arrived in 1970 when Naoyoshi Taguchi (*Gas Detecting Device*) realized a semiconductor element capable of detecting low concentrations of inflammable and reducing gases for home or industrial usage. The sensing element designated by its extensive research was SnO_2 and the name of the company selling the device was Figaro Engineering Inc. (name comes from the passion of Mr. Taguchi for opera). A step from Figaro would be in the next years the addition of Pd as metal catalyst. In the late 1980s research in semiconductor gas sensor increased consistently becoming one of the most attractive in the sensor community, this, supported by a the growth of material chemistry and material science enlarged the spectrum of sensing materials available and took to the development of high performance solid state gas sensors (Neri, 2015). Nowadays thanks to the opportunities given by nanoscale fabrication technologies more chances are given to the development of high performance semiconductor gas sensors. Figaro gas sensor was an authentic success and nowadays this with some other companies are on the market offering this type of gas sensor: Nissha FIS, SGX Sensortech, UST Umweltsensortechnik, City Technology, AppliedSensors, NewCosmos Electric.

3.2 Working principle

Ceramic materials like metal-oxides have in general large bandgap energy resulting in an insulating behavior. Taking for example Tin-oxide (SnO_2), this material is characterized by a 3.6 eV bandgap, nevertheless its resistivity is smaller than the one of common semiconductors. The reason behind this particular phenomenon has been associate for long time with the presence of donor levels near the conduction band (electrons conduction) due to the presence of oxygen vacancies in the material: in particular to the non-stoichiometry and oxygen-related intrinsic defects (Kılıç and Zunger, 2002). This particular and popular family of materials in the metal oxide gas sensing technology is defined as n-type because of the conduction driven mainly from the electrons. Of course this implies even the presence of materials which are defined p-type and whose behavior will be specified later in this chapter. In this respect oxygen is crucial to the functioning of the device not only because of its absence (vacancies) in the material structure but also because of his presence in ambient atmosphere ultimately gives rise to the conduction modulation effect. Indeed for temperatures around between 150 and 450°C when the sensing material is in contact with an air mixture (and correspondingly with O_2 oxygen) a peculiar mechanism occurs generally defined as "ionosorption model". Atmospheric oxygen adsorbs reversely on the metal-oxide open air surface as molecular (O_2^-) or atomic (O^{2-}, O^-) ions which capture an electron from the conduction band (CB) of the semiconductor (figure 3.1). The oxygen is reduced in this reaction, for the case of atomic ions for example we have:

$$O_2 + 2e^- \rightleftharpoons 2O^-$$

When the electrons move from the semiconductor to the surface leave behind the positive charges of the lattice, creating a so-called positive space charge region whose total charge is equal to the total charge of the electrons at the surface. This charge depletion induces an upward band bending at the surface compared to the oxygen free case (Fermi level is still flat). Since in this area a lower number of electrons compared to the bulk is present (correspondingly is more resistive than the bulk), it is defined as electron-depleted region or layer. At a certain point an equilibrium between the electrons which can move to the surface and the barrier creation will be reached. The magnitude of the barrier will be equal to qVs with Vs which is a surface potential (figure 3.1), this barrier will determine a surface conductance of $G = G_0 exp(-qVs/kT)$. The depth of the depleted surface region is defined as Debye Lenth:

$$L_D = \sqrt{\frac{\epsilon\epsilon_0 kT}{q^2 n_b}}$$

Where ϵ is the material dielectric coefficient, n_b is the bulk electrons concentration, ϵ_0 is the vacuum permittivity, q is the electron charge, k is the Boltzmann constant and T is the temperature (Gurlo, 2006). Several assumptions are necessary in this model. First it is assumed that there are no other adsorbed oxygen species beside physisorbed oxygen and oxygen ions. Second the electron movement concern the electrons only. For what concern the nature of adsorbed oxygen both molecular and atomic ions are always present at the same time. However it has been shown that in general at low temperature (100-200°C) mainly the molecular form dominates while at higher temperatures (200-400°C) is the atomic form which dominates (Gurlo, 2006).

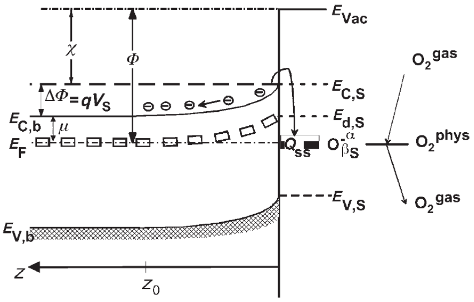

FIGURE 3.1: Energy band diagram of the surface of a MOX material after oxygen adsorption. Adapted from Barsan and Weimar, 2001.

Once the surface of the MOX is oxygen rich, if the gas is introduced in the atmosphere it will interact with the oxygen adsorbed. If the gas is a reducing gas, it will reduce the oxygen which will release the electron previously taken from the CB of the MOX and will bond instead to the electron of the reducing gas. Opposite behavior if the gas is an oxidizing gas, in this case, an analogous and competitive phenomenon to the oxygen adsorption will happen and the oxidizing gas molecule/atom will take an electron from the CB of the MOX. This redox reactions will of course impact the electrical behavior of the MOX in opposite manners (Yamazoe and Shimanoe, 2008 Ionescu et al., 2003). For a reducing gas, the electron previously bonded to the oxygen will be released back into the CB, where, it will be available again for conduction increase the conductivity at the surface of the material:

$$R + O^- \rightarrow RO + e^-$$

Where R represents a reducing gas.

For an oxidizing gas, if the adsorption of the oxidizing gas is stronger than oxygen one, the already reduced conductivity of the material surface will be further reduced because of the further decrease of the electrons in the CB:

$$A + e^- \rightleftharpoons A^-$$

Where A represents an oxidizing gas.

This microscopic local change in the number of carriers at the surface impact the total conductivity of the conductive material, which is fundamental for the functioning of the device. In order for this local conductivity change or gas modulation effect to impact effectively, is necessary for the MOX to be highly exposed to the atmosphere or more precisely to have a high surface-to-volume ratio. For this reason this type of devices have generally a porous morphology, since is necessary for the gas interact with most part of the conducting volume, modulating positively or negatively the surface barrier created by the oxygen adsorption.

From now on the sensing film will be assumed to be porous, even if this is not always the case.

Within this assumption, it is important to distinguish between different cases and morphologies of the porous layer which depends on the relative size between the Debye length and the grain size defined generally as d.

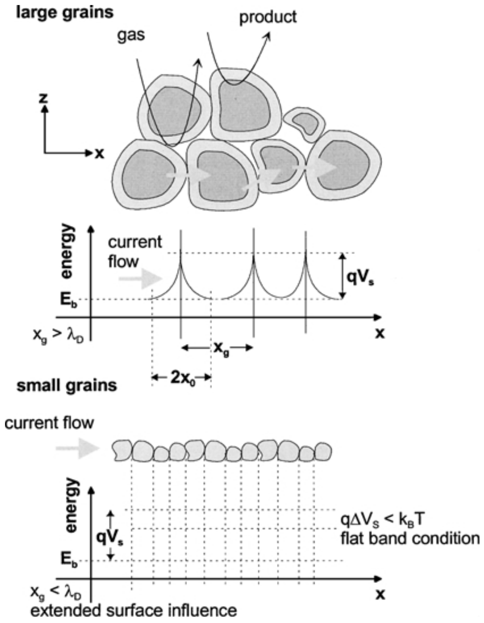

FIGURE 3.2: Energy band diagram of MOX grains after oxygen adsorption for the cases of small grains ($d < L_D$) and large grains ($d > L_D$). Adapted from Barsan and Weimar, 2001.

If $d < L_D$ the entire layer is depleted and is influenced by the surface phenomena; a structure like this is shown in the lower part of figure 3.2. In this situation exposure to reducing gas can highly influence the conduction switching from a completely depleted case to a partly depleted one. Opposite case for an oxidizing gas which can make the structure switch from a partly depleted structure to a completely depleted one. The band bending ΔE, evaluated from the grain surface to its bulk, covers an important role. If this value is comparable with the thermal energy then the electron concentration in the grain is constant and band can be considered flat. Additionally mean free path becomes comparable with the grains dimension and the number of surface collisions influenced by the adsorbed species (which act as scattering centers) become comparable with the bulk ones.

The $d > L_D$ case (upper part of figure 3.2) shows the situation in which some part of the grains are unaffected by the surface adsorption and at the same time are not sintered together. In this situation the charges will see a single Vs barrier when moving from grain to grain. If the grains are instead sintered we can have two different conditions as shown in figure 3.3.

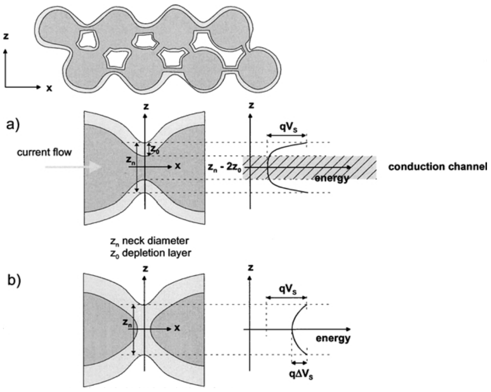

FIGURE 3.3: Energy band diagram of sintered MOX grains after oxygen adsorption in the case of sintered grains. In a) the contact area between the grains is large enough to do not be influenced by the surface effects, in b) the contact area between the grains is small enough to be influenced from the surface effects. Adapted from Barsan and Weimar, 2001.

For the b) case of the previous figure, since the contact area between the grains (z_n in the figure) is large and comparable to L_D, if $qV_S > k_B T$ the carriers moving from grain to grain will experience different Vs barriers according to the z position. In this regard is possible to consider an average value for the potential barrier. If instead $qV_S < k_B T$ all these carriers moving from grain to grain will feel the same potential. In the case a) of the same figure (3.3), the contact area is large enough to do not be influenced by the surface effects ($z_n >> \lambda D$), in this situation a conduction channel unaffected by the surface phenomena is created. (Barsan and Weimar, 2001).
To summarize this first part, smaller grains are requested because of the high surface-to-volume ratio which favor the device interaction with the atmosphere, as the fraction of material within the Debye length (therefore directly influenced by the surface phenomena) is larger.

A topic which is generally underreported in literature is the stability issue, especially compared with other parameters like sensitivity and selectivity. If we think about market applications this parameter has however a major role which should guarantee a reliable working period of around 2-3 years. In all the cases, stability of MOX sensors represents one of the main issues with influence of factors like: structural and phase transformation, poisoning, heaters and contacts degradation, bulk diffusion, change of humidity and other interference effects (Korotcenkov and Cho, 2011).

As mentioned in section 2.4.1 humidity represents a fundamental problem for MOX devices since increase their surface conductivity. Despite this effect is well known and confirmed in literature that there are three mechanism which try to given and explanation for this: two direct mechanisms proposed by Heiland and Kohl, 1988 and an indirect one suggested by Morrison, 1990. As shown in Barsan and Weimar, 2001 between 100 and 500°C interaction of the metal-oxide with water vapor brings to the adsorption of molecular water or hydroxyl groups, the latter whose presence is dominant above 200°C are fundamental for the hypothesized mechanisms.
In the first hypothesis from Heiland and Kohl (Heiland and Kohl, 1988), water molecule homolytically dissociates into OH which interact with Sn, and into H which interact with the lattice oxygen, this latter interaction generate a OH which

because of its electron affinity ionize in OH^+ injecting a free electron in the conduction band:

$$H_2O + Sn_{Sn} + O_O \rightleftharpoons (Sn^+_{Sn} - OH^-) + (OH)^+_O + e^-$$

Where the subscripts Sn and O refers to the lattice elements.
In the second (Heiland and Kohl, 1988) hypthesis the mechanism is similar, except from the fact that hydroxyl group generated from the lattice oxygen binds with Sn, the additional electron is created by the oxygen vacancy produced:

$$H_2O + 2Sn_{Sn} + O_O \rightleftharpoons 2(Sn^+_{Sn} - OH^-) + Vo^{++} + 2e^-$$

Indirect mechanisms are instead suggested by Morrison, 1990 and Henrich and Cox, 1994, in this case the hypothesis is either the interaction of the hydroxyl group or the hydrogen atom with an acid or basic group, either a displacement of the adsorbed oxygen by water; several other indirect mechanisms are hypothesized as well.
In general, structural transformation refers to the change in grains size, key parameter for MOX sensors performance; as just described, this brings to a change in the conduction mechanism and correspondingly of the device performances. First and fundamental condition of this growth is associated with coalescence: while a large surface-to-volume ratio increases the device repose, at small grain dimensions driving forces for diffusion are stronger and cause the grain growth over the sensor lifetime (Thornquist, 2019). This grain growth increases indeed the contact area creating necks (Korotcenkov, 2005, Korotcenkov, 2008). In general it is found (Thevenin et al., 2001, Korotcenkov and Cho, 2011) that this material transport is due to: vapor transport, surface diffusion, grains boundaries and crystal lattice diffusion.
A solution which is generally approached is annealing, which is basically the application of heat to the material in order to give the atoms enough energy to rearrange in a more equilibrium configuration (Thornquist, 2019), in general for a MOX film, positive and negative effects can derive. When the as-deposited metal-oxide is amorphous, annealing can promote crystallization, leading to a polycrystalline structure. At the same time this favors surface reconstruction and diffusions reducing the surface to volume ratio, this correspondingly reduce the crystal growth driving forces reducing the cause of the instability. At the same time however this, lowers the performances since the film is packed more densely and the surface-to-volume ratio is low, moreover the vacancies (which allow the film to conduct) are reduced (Thornquist, 2019). A further effect which accompanies the grains size is the change in crystallographic orientation as established in Korotcenkov, 2005, different planes have different electronic configurations which influence the adsorption and catalytic properties as well as the inter-grain transport (Korotcenkov and Cho, 2011).
For what concern phase transformation, for long-term operation, additives can segregate into separate phases (Korotcenkov, 2005, Wang et al., 2007). It is established that grain size and crystallinity can influence the solubility of additives in the material: increasing the size decreases the solubility (Straumal et al., 2009), potentially leading to segregation and other chemical and electrophysical changes. It is worth to mention that the phase composition may change because of reactions with the surrounding atmosphere.

Doping represents an important opportunity in the MOX gas sensors implementation. For solution-based processes doping is possible through annealing driven diffusion of a metal layer or through dopants dispersion inside the solution. For sputtering processes (fabrication technique used in this internship) doping is again

possible through diffusion or directly using a pre-doped MOX target (deposited material). Because of the elevated numbers of parameters (dopants, percentage of doping,..) in doping, phenomenological results in literature are present by far more than theoretical ones (Segantini, 2017). Moreover these results show sometimes opposite influences from the doping, for example for sensitivity and stability: increasing in some case (Tricoli et al., 2008, Matsuura and Takahata, 1991) and decreasing in some other (Lu et al., 2006). In spite of that some conclusions can be reach, like the fact that the most useful metals for this applications are Pd, Pd, Au and Ag. Two reason can be behind the effects of doping: the catalytic activity and the structural change.
For the catalytic activity for example is well known for Pd to act as special adsorption site for oxygen with increase of oxygen ions to the surface (Göpel and Schierbaum, 1995). Catalytic power of Pd brings consequently to a lowering of the activation energy of the surface chemical reactions, with corresponding shift of sensitivity towards lower operating temperatures.
In the hypothesis of structural change in of the material the stoichiometry changes changing parameters like gas diffusion (Korotcenkov, 2005).

3.3 P-type metal oxide sensors

As mentioned in section 3.2 additionally to n-type gas sensors p-type gas sensors exist, which (as the name suggests), are based on holes-based conduction and differ from the first for its behavior and a consistent number of other characteristics.
In general the most popular materials used in the MOX gas sensors are n-type, in particular (Kim and Lee, 2014) SnO_2 (Comini et al., 2002, Kolmakov et al., 2003) and ZnO (Wan et al., 2004, Jing and Zhan, 2008). Some other largely explored n-type materials are TiO_2 (Kim et al., 2006, Devi et al., 2002), WO_3 (Moon et al., 2012, Li et al., 2004), In_2O_3 (Li et al., 2003, Zhang et al., 2004) and Fe_2O_3 (Chen et al., 2005, Kim et al., 2011b). The same attention is not received from p-type materials such as NiO, CuO, Co_3O_4, Cr_2O_3, Mn_3O_4. For this semiconducting family indeed related research is relatively new because of a quite simple reason: the general response of these devices is lower than that of n-type ones. A curious fact is that a search of web of knowledge of July 15th, 2013 (using the chemical formula and "gas sensor" as keywords, i.e. "SnO_2" and "gas sensor") on the 8504 total articles on metal-oxide-semiconductor-based gas sensor, less than 10% was related to p-type semiconductors as shown in figure 3.4.

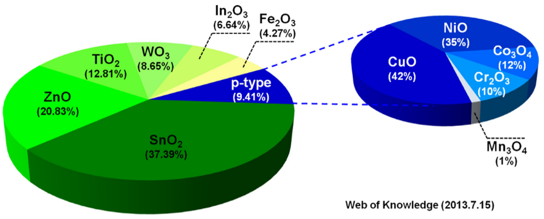

FIGURE 3.4: Studies on n- and p-type metal oxide semiconductor gas sensors (internet search of Web of Knowledge on July 15, 2013). Adapted from Kim and Lee, 2014.

Nevertheless p-type sensing devices are still promising materials thanks to their distinctive oxygen adsorption and rapid recovery kinetics (Kim et al., 2011a, Kim et al., 2010).
Differently from n-type devices, in p-type one conduction is related to the presence

of acceptor levels near the valence band (holes conduction) due to metal ion vacancies and metal ionization states (Thornquist, 2019). Like in n-type materials these devices are based on the oxygen ionosorption for temperatures between 150 and 450°C and the further interaction of the reducing and oxidizing gases. A fundamental difference comes from the fact that while in n-type materials ionosorption create at the surface a electron depleted region, in p-type ones this correspond to a holes accumulation region, which is consequently more conductive than the bulk region at the center of the holes. First consequence of this is the opposite response to reducing and oxidizing gases with respect to the n-type case:

- n-type
  - Reducing gas: $R_{baseline} > R_{gas}$
  - Oxidizing gas: $R_{baseline} < R_{gas}$
- p-type
  - Reducing gas: $R_{baseline} < R_{gas}$
  - Oxidizing gas: $R_{baseline} > R_{gas}$

Indeed when a gas reduces the ionosorbed oxygen, the electrons given back to the CB recombine with holes decreasing the number of majority carriers and correspondingly the conductivity of the surface. The second consequence of p-type mechanism is the decrease of sensitivity compared to the n-type counterpart. The sensor resistance for the latter (n-type) is determined by the shell-to-shell contact of the grains, this correspond electrically to serial connections of semiconducting cores (R_{core}) and resistive grain-to-grain contacts ($R_{surface}$) as explained by Kim and Lee, 2014. On the other side conduction on p-type grains can electronically be seen as a competition of the wide resistive core (R_{core}) and the thin conductive surface region ($R_{surface}$). According to Hübner et al., 2011 for the same morphology and geometry a p-type sensing device show a sensitivity equal to the square root of a n-type one:

$$S_p = \sqrt{S_n}$$

Considering such a low sensitivity, to work with single p-type sensors is necessary to enhance the response in some manner, nevertheless p-type materials are still promising to develop new functionalities in the devices (Kim and Lee, 2014) as will be shown in the next section.

3.3.1 New functionalities

Despite n-p semiconductor junctions are well known for their applications in diodes, transistors and solar cells, interesting results have been obtained too in the gas sensing research, combining n-type and p-type gas sensing materials.

Kawakami and Yanagida, 1979 for example were the first to use a junction of polycrystalline n-type (Li doped NiO) and p-type (ZnO) as humidity sensor, this application then have been expanded to other gases (Kim and Lee, 2014). The functioning of these devices is based on the measurement of the longitudinal (through the junction) IV characteristics of the p-n junction which varies under reducing/oxidizing gas exposure. The fundamental advantage of these structures is the different selectivity to gases given by the possibility of using different combinations of materials. As example Devi et al., 1995 reported that $CuO(p)/SnO_2(n)$ heterocontacts have good sensitivity and selectivity to H_2S, attributed probably to the chemical affinity with CuO which is then converted to metallic CuS upon exposure to the gas. In general reproducibility and stabilization of these sensors (longitudinal p-n) is difficult, moreover in the case of a perfect heteroepitaxial interface the response is not strong because of the low accessibility of the gases.

Another family of p-n junction based gas sensors is the one of n-type and p-type nanocomposites. Here n-type nanoparticles are dispersed into p-type ones and vice versa, correspondingly n-n, p-p and p-n nanocontact points are created and the current is correspondingly no longer asymmetric. According to ratio, concentration, size and dispersion of the two types, different conduction paths are possible. If more n-type or p-type particles are present the conduction is relatively through n-n and p-p contacts, when the presence of p-n contacts dominate the resistane is of course maximum. Several example of selectivity towards H_2S exist, still by means of $CuO(p)$ loaded on n-type materials: SnO_2 (Zhou et al., 2001, Tamaki et al., 1992), ZnO(Kim et al., 2012, Datta et al., 2012), MoO_3 (Wang et al., 2012); again the CuO is converted to metallic CuS near the junctions decreasing or eliminating the built in n-p potential and highly decreasing the resistance.

The last category of p-n junction based gas sensors is the one generally made of a n-type material decorated with p-type particles or cluster. In general 1D structures like NWs, nanotubes and nanorods have good long-term stability and strong-response (Kolmakov and Moskovits, 2004, Sysoev et al., 2007,Comini, 2006, Kim and Lee, 2014), at the same time however for fabrication techniques like vapor-liquid-solid (VLS) these wires have a size generally thicker than 70 nm (Mathur et al., 2005, Nguyen et al., 2003, Yang et al., 2002) where a 5-10 nm surface depletion region is consequently not highly effective (Ghosh and Raychaudhuri, 2008): an interesting approach shown by Na et al., 2012b shows interesting results.
Na et al., 2012b fabricated pure and $Mn_3O_4(p)$-decorated $ZnO(n)$ nanowires (NWs), pure $Mn_3O_4(p)$ NWs and $ZnO(n)$-$ZnMn_3O_4(p)$ core-shell nanocables. The former two showed n-type behavior while the latter two p-type behavior, showing that the conduction in the nanocable occurred through the $ZnMn_3O_4(p)$ shell section. In figure 3.5 is shown the response to ethanol (C_2H_5OH), as you can see the two p-type samples show low sensitivity because of the intrinsic conduction mechanism type, at the same time n-type $ZnO(n)$ NWs show an higher response compared to these which is even bigger in the $Mn_3O_4(p)$-decorated version increasing (considering sensitivity as $R_{baseline}/R_{gas}$) from 7.2 to 30.8. As just seen p-type decoration seems to

increase the response of n-type 1D nanostructures.

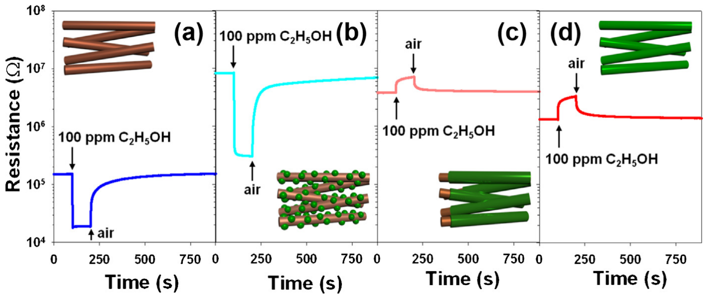

FIGURE 3.5: Response transient for (a) a pure $ZnO(n)$ NWs, (b) $Mn_3O_4(p)$ decorated $ZnO(n)$ NWs, (c) $ZnO(n)$-$Mn_3O_4(p)$ core-shell nanocables and (d) pure $Mn_3O_4(p)$ NWs. Adapted from Na et al., 2012b and Kim and Lee, 2014.

To this sensitivity increase, as shown in figure 3.6 (c), corresponds even a baseline resistance (defined even as resistance in air) of the ZnO NWs. This is probably related to the extension of the electron depleted region further inside the wire decreasing the conductive cross section. Still in figure 3.6 (a) and (b) you see similar results for the case of $NiO(p)$ and $Cr_2O_3(p)$ decoration of the same NWs (Na et al., 2012a,Woo et al., 2012).

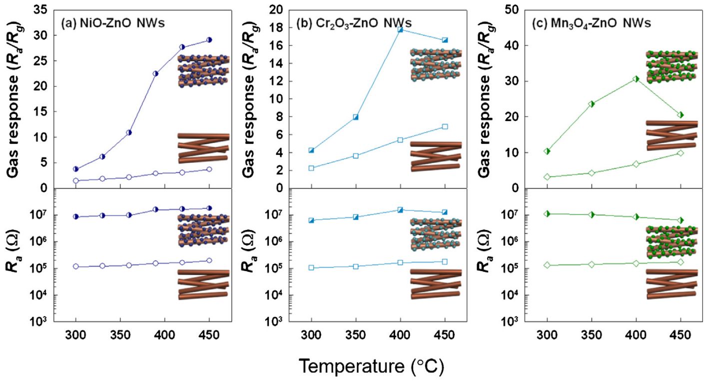

FIGURE 3.6: Response (where R_a is resistance in air and R_g is resistance under gas) and baseline resistance (equivalent to R_a) for (a) $NiO(p)$ decorated $ZnO(n)$ NWs, (b) $Cr_2O_3(p)$ decorated $ZnO(n)$ NWs, (c) $Mn_3N_4(p)$ decorated $ZnO(n)$ NWs. Adapted from Kim and Lee, 2014, Na et al., 2012b, Woo et al., 2012, Na et al., 2012a.

The previous phenomenon (of response enhancement and baseline resistance increase) has been defined in recent literature as electronic sensitization, to distinguish from another demonstrated sensitization defined as chemical sensitization. Indeed in some cases of n-type NWs decorated with p-type clusters, these particles showed catalytic activity for specific gases increasing the selectivity of the device. This is the case of Hwang et al., 2009 which decorated $SnO_2(n)$ NWs with $CuO(p)$ increasing the selectivity towards H_2S. Interesting result was presented by Kim et al., 2010 which created $NiO(n)$-decorated SnO_2 hollow SnO_2 spheres which showed a 90% recovery time smaller than 5 s at 450°C. Additionally it was demonstrated that loading commercially produced $SnO_2(n)$ nanoparticles with $NiO(p)$ it is possible to decrease the response to 20-100 ppm of ethanol from 100-700 s to 30 s (figure 3.7). Similarly Wang et al., 2012 showed that $NiO(p) - SnO_2(n)$ hollow spheres showed a recovery around 4 s from 20 ppm of NH_3 at 300°C.

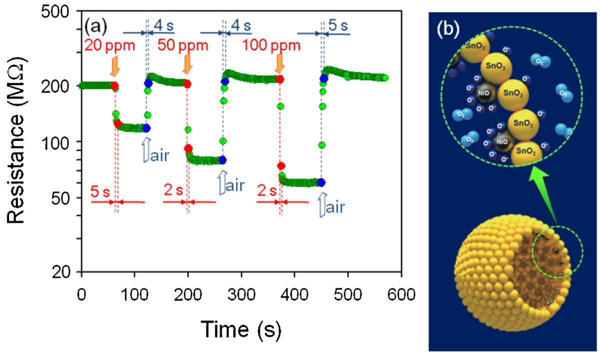

FIGURE 3.7: Dynamic sensing to ethanol (C_2H_5OH) at 450°C (a) and (b) structure of $NiO(p)$-functionalized $SnO_2(n)$ hollow spheres. Adapted from Kim et al., 2010.

These results have been correlated with the well known the ability of $NiO(p)$ to adsorb high oxygen quantities which is then transfered to $SnO_2(n)$, were diffusing and reacting in higher quantities determine a faster recovery. This chemical sensitization phenomenon is generally defined as chemical-spillover. It is found that the large amount of oxygen adsorbed on NiO is due to its characteristics of being a transition metal oxide which have low stability promoted by the variable oxidation state (Kim and Lee, 2014, Iwamoto et al., 1978, Kohl, 2001, Védrine, 2016).

Another successful result of $SnO_2(n)$ performance enhancement by $NiO(p)$ loading was achieved by Kim et al., 2011a which showed how for certain conditions humidity influence can be highly reduced. Kim et al., 2011a prepared pure and $NiO(p)$ loaded $SnO_2(n)$ hierarchical nanostructures, with a weight of Nickel-oxide equal to 0.64% and 1.27%, then, tested their response to CO in dry and 25% humid atmosphere. Pure SnO_2 showed significant variation under humidity influence, under this condition a lower resistance was measured (as expected from 3.2) with a worse response, recovery time and response time compared to the case of dry atmosphere. On the contrary the 1.27 wt% NiO-loaded counterpart showed the same gas detection characteristics in dry and in 25% humid atmosphere, similar result for the 0.64 wt%, for which the only difference between the two atmospheres was in the baseline resistance. These results are visible in figure 3.8 and shows that in addition to recovery and response enhancement, low humidity independent gas sensors can be realized too by p-type decoration.

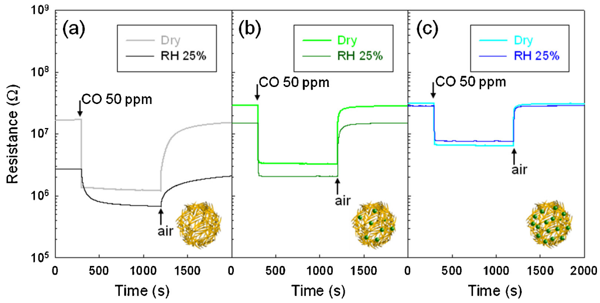

FIGURE 3.8: Dynamic sensing for hierarchical spheres made of pure SnO_2 (a), 0.64 wt% NiO-loaded SnO_2 (b) and 1.27 wt% NiO-loaded SnO_2 (c), response is tested in dry and 25% relative humidity atmospheres to 50 ppm of CO at 400°C. Adapted from Kim et al., 2011a and Kim and Lee, 2014.

3.4 Conclusions

As shown in the previous section the combination of both n-type and p-type gas sensing materials shows interesting results in terms of gas-sensors selectivity, sensitivity and other features. This represents a interesting direction for the gas sensor researchers to move over the performances of classic gas sensing technology. Results like Woo et al., 2012 are clear examples of how starting from well known classical gas-sensing materials and engineering the geometrical structure and fabrication it is possible tune the different gas sensing parameters according to your final application: an electronic nose in our case. In Woo et al., 2012 we see 1D structures, structures not trivial to realize with the current nanofabrication technology. Full manufacturability, in terms of ease of integration with existing process technologies and scalability of the approach, remains to be demonstrated.
An interesting prospective from this point of view is the sputtering technology. For this reason this study aims to achieve those physical effects shown in the previous section (chemical and electronic sensitization as shown in figure 5.1) with this relatively simple fabrication technique.

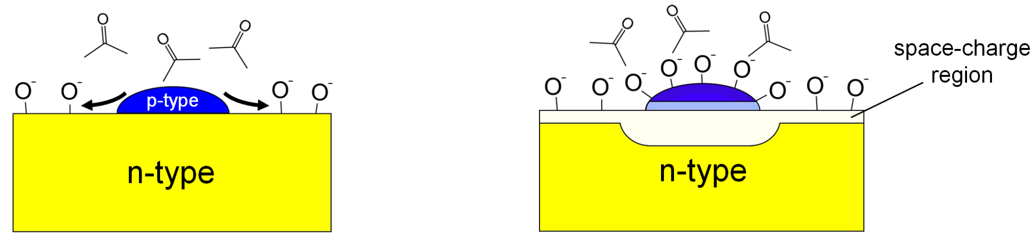

Chemical Sensitization (spillover and/or catalysis)

Electronic Sensitization (depletion region modulation)

FIGURE 3.9: Chemical and Electronic sensitization: possible physical explanations of the response enhancement in n-type gas sensing structures decorated with p-type ones. Adapted from *Sputtering of metal oxide semiconductor n-p stacks*.

Chapter 4

Device fabrication and testing

MOX sensors fabricated by the Sensor Group have the common geometry of conductometric gas sensors as explained in 1.2.1. As you can see in figure 4.1 interdigitated electrodes (IDEs) and the relative connection are patterned on a substrate, then the sensing layer is deposited on top of them leaving a part of the connection with the IDEs uncovered to then deposit the Gold contact which make possible the device testing on the probe station.

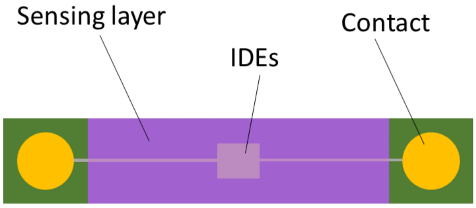

FIGURE 4.1: Structure of the conductometric gas sensors fabricated.

First part of fabrication (from Silicon wafer to IDEs deposition) is made in a cleanroom environment, the second part (sensing layer and Gold contact deposition) is made in another fabrication room (not cleanroom features) while testing of the device is made instead in a testing lab.

4.1 Nanofabrication (or cleanroom process)

Fabrication starts from a 8 inch Silicon wafer with 1 μm of SiO_2 on top, this is enough to guarantee insulation from the substrate (figure 4.2). Process flow of the IDEs fabrication from the substrate is shown in figure 4.3.

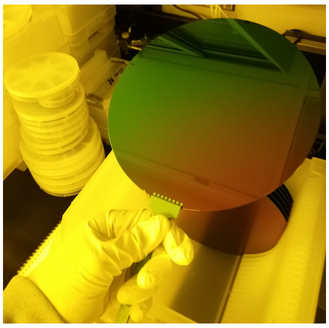

FIGURE 4.2: 8 inch Silicon wafer used for the device fabrication. Upper surface has $1\mu of SiO_2$

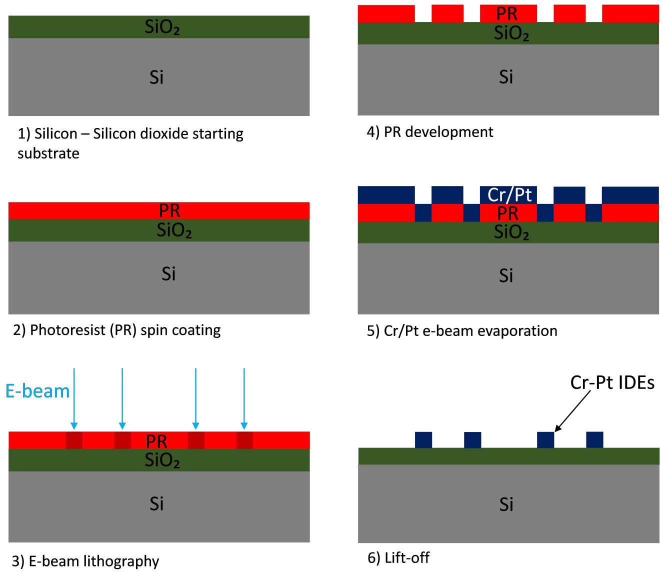

FIGURE 4.3: Process flow of the IDEs fabrication.

The next main step is to spin-coat the photoresist (PR) which will then be patterned to created the metal IDES.

Generally the wafers used remain inside the box on open cleanroom air for a consistent amount of time, therefore, before proceeding to the next step (adhesion layer deposition) an Oxygen plasma cleaning is made for some seconds. This guarantees the removal of the species which have adsorbed or deposited on the wafer surface over time. After this cleaning and before the photoresis spin-coating, it is necessary to deposit the adhesion layer, this is made using the proper high-T, vacuum machine where HDMS (Hexamethyldisilazane) is used as adhesion material. Next step is the spin-coating of the photoresist. The photoresist used is an IBM-proprietary formulation. A specific amount of solution is dripped on the center syringe through 0.2 μm filter to remove the larger particles of the solution, once the liquid is on the wafer it necessary to select the correct recipe, this with a specific amount of the solution and a specific amount of time (some seconds in our case) guarantee the correct thickness of the photoresist.

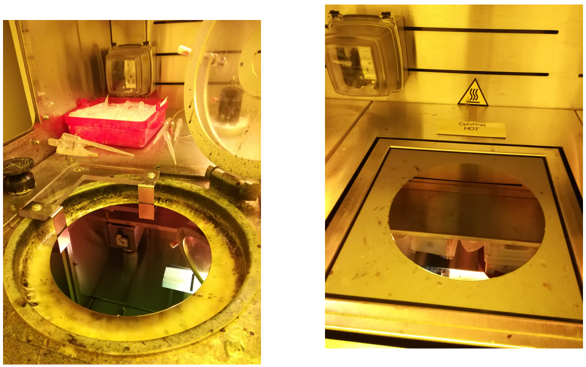

(A) Wafer centering on the station prior to spin-coating.

(B) Soft-baking on the hot plate at 120°C for few seconds right-after spin-coating.

FIGURE 4.4: Two steps of the photoresist deposition process.

Right-after the spin-coating the wafer is immediately placed on a 120°C hot plate for a short amount of time as soft baking process like is shown in figure 4.4b. After cooling the wafer, it is possible to check the result, in some cases the characteristics "shooting starts" from the center to the edge of the wafer will be visible. These are due to particles deposited on the wafer before the spin-coating, however in rare cases they impact the final result. Next step is the patterning of the freshly deposited photoresist.

The wafer is loaded in the electron beam lithography machine (e-beam lithography machine) which is operated by a technician, the machine is capable to contain around 4, 8 inch wide wafers at the same time, a pre chamber is used in this step in order to do not break the vacuum of the bigger writing chamber. The pattern used is a set of interdigitated electrodes (IDE), such as the one shown in figure 4.5b. As a positive photoresist was used, the e-beam exposed pattern will be developed away leaving the pattern space where the IDEs metal is deposited.


(A) Electron beam litography machine (e-beam).

(B) IDEs CAD layout.

FIGURE 4.5

Development post e-beam writing is made with TMAH (tetramethylammonium hydroxide), this developer requires particular attention compared to developers like NMP used in one of the next processes because extremely toxic. To handle TMAH are indeed generally used Stansolv A-10 gloves and a special plastic basin. To develop the photoresist the wafer is dipped into the basin for a couple of minutes, once the development is completed the wafer contains now a photoresist pattern corresponding to the negative of the IDEs pattern.

Before the metal deposition an Oxygen plasma cleaning is made to remove the species deposited newly on the wafer, etching time depends on the amount of time the wafer has remained to ambient air. To deposit the IDEs metal the wafer is loaded into the electron-beam evaporator shown in figure 4.6.

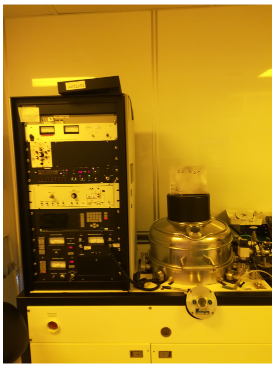
FIGURE 4.6: E-beam evaporator for the IDEs metal deposition.

This machine as many vacuum technology machines consists of an upper chamber where the wafer is loaded and a lower chamber which contains the crucibles. Generally before the deposition a pressure smaller than $2 * 10^{-6}$ Torr is expected in order to obtain a clean enough process. In this machine the evaporation of the metal is possible thanks to a beam of electrons which accelerated hit the metal in the crucible, this avoid contamination from the liner and from the filament (present instead in the thermal evaporation). In this step we deposit first a thin (some nm) layer of Chromium which favor the adhesion the substrate with the Platinum which is deposited right after. For Platinum we targeted 50 nm. To complete the IDEs fabrication is necessary to develop the photoresist used as negative pattern for the IDEs, this process is called lift-off, since the photoresist and the metal above are lifted away. Working on the wet bench the wafer is first placed in a plastic holder to be then dipped in the NMP (N-Methyl-2-pyrrolidone) bath. In our case since an around 50°C temperature of the solvent is used generally, for the complete lift off 20 min is enough, a longer time is necessary for a lower temperature. After development the wafer is placed in IPA (Isopropyl alcohol) to remove the NMP, to then remove the IPA the wafer is washed with the water nozzle and placed in the rinse dryer machine. It is important to move the wafer from bath to bath in a quick way in order to avoid the ambient drying, for the same reason the rinse dryer machine is used at last. The final result is visible in figure 4.7a, as you can out of one wafer is possible to obtain 7 groups of 5 IDEs.

(A) Final results of the IDEs fabrication, 7 groups of 5 IDEs each are obtained for single wafer.

(B) Microscope image of the IDEs fabrication result.

FIGURE 4.7

Before the sensing layer deposition, the result is verified on the optical microscope, an example is shown in figure 4.7b. It important to mention that the layout shown in figure 4.5b is different from the one of figure 4.7b, this, since two different layout are used in the Sensor Group: one more resistive for the vacuum based technology (sputtering) sensing layers and the other less resistive for the solution based technology (sol-gel) sensing layers. The next immediate step in the sensors fabrication is the sensing layer deposition by sputtering which will be explained in the next session.

4.2 Metal oxide sputtering

Although sputtering technology is not the main focus of this study, it is nevertheless important to understand how the physics and the parameters of this technique influences the sensing layer morphology. Sputtering technology is a Physical Vapor Deposition (PVD) well known technology in the field of nanoscale fabrication since capable of depositing an unlimited number of materials. The operational principle is based on ion bombardment of a target material from which atoms are ejected depositing on the substrate forming a film. In order to create and drive the ions (generally made of Ar) a plasma is fundamental, in particular the glow discharge which is created through a DC or a AC (RF) current which is always applied between the target (material to deposit) and the substrate. In the DC version the cathode is represented by the target while the anode by the substrate, when a voltage is applied between the two in the Argon volume the free electrons are accelerated colliding with atoms ionizing electrons or exciting eventually gas atoms (which then relax emitting the characteristic light of the glow discharge). New free electrons are then accelerated again contributing to the process of ionization, it is said that this process sustains the plasma, made of: atoms, ions, electrons and radicals.

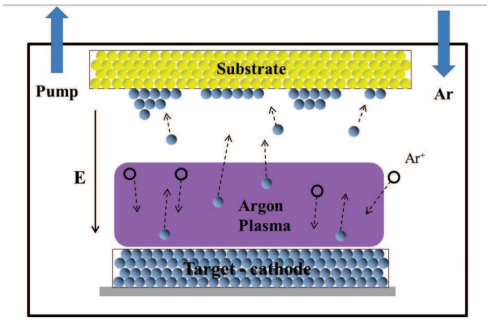

FIGURE 4.8: Simplified representation of a sputtering process. Adapted from: Xie, 2013.

A general example of sputtering structure is shown in figure 4.8. Ions present in the plasma are instead accelerated towards the cathode (target) sputtering off the atoms which traveling through the plasma deposit on the substrate. It is fundamental to keep in mind that the plasma is a conductor with not consistent voltage drops except close to the electrodes. In DC sputtering the potential profile of the plasma has a slope in proximity of the cathode which correspond to an acceleration of the ions, this because compared to the far off region there are less chances of collision. A different profile is instead present in RF sputtering, here the plasma is biased positively with respect to both electrodes, the solution for this to use electrodes of different dimensions, in particular using a smaller area for the target electrode is possible to increase the current density increasing the sputtering rate at this side. RF has been introduced in general for non conductive materials deposition since alternating current avoid the accumulation of charges.

A particular solution to deposit oxides is reactive sputtering. In reactive sputtering, in addition to the solid target to deposit, a reactive gas is introduced to the chamber which is further incorporated into the film. A complete representation of this process running within the chamber is shown in figure 4.9.

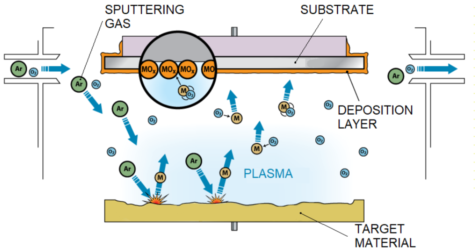

FIGURE 4.9: Simplified representation of a reactive sputtering process. Adapted from: *Sputter Deposition*.

4.2.1 Tool

Sputtering tool used for the sensing layer fabrication is shown in figure 4.10a.

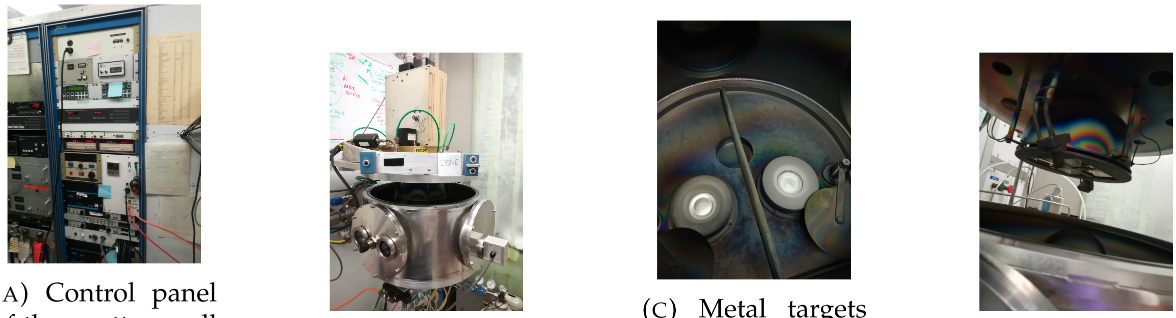

(A) Control panel of the sputterer, all the deposition parameters are controlled from this side.

(B) Deposition chamber, currently open.

(C) Metal targets and the relative open shutters at the bottom of the chamber.

(D) Substrate, attached at the chamber roof.

FIGURE 4.10: Sputtering tool.

The machine is composed of two main parts interfaced with the operator: the control panel and the chamber. Compared to the conventional industrial machines this system is custom, this because working in a research environment the user wants to be able to change the different parameters to create different morphologies. The sputterer employs a rough pump and a high vacuum pump, connected to the chamber through a controllable valve which allow to set the desired pressure within the chamber. Gas switch and mass flow controllers allow to enable and tune the flows of Argon and Oxygen to the chamber: the former (as specified before) is used as sputtering gas while the second as will be further explained later is used to create the oxide. As shown in figure 4.10c the chamber contains two different targets, in this case Tin and Nickel, on top of them we find the relative shutters fundamental to launch the on substrate deposition and confine the plasma on the target. Each shutter is controlled by a thin film deposition controller which can monitor the deposited thickness through a quartz micro balance (QCM), disactivated in this cases. Both a DC and a RF generator can be connected with the target for the deposition, for the latter an RF matching box is present to automatically match the sputtering circuit. An RF generator (and the relative matching box) too is present and connected to the substrate situated on the roof on the chamber. Additionally a temperature control is connected with the substrate to change the deposition conditions while heater is connected to the chamber walls to allow outgasing.
To fabricate the metal-oxide sensing layer reactive, sputtering is used; indeed while

metallic atoms are provided from the target, the Oxygen ones are provided by the gaseous O_2. A precise ratio of Oxygen and Argon determine the desired stoichiometry of the film. An alternative way to deposit the metal-oxide would be to use a regular non-reactive configuration using only Argon as gas and a compound target necessarily (reason explained in section 4.2) to sputter in RF. With this latter technique the substrate stoichiometry is forced to be the same of the target, moreover custom target with custom stoichiometries are more expensive than the reactive counterpart. A fundamental problem of the reactive deposition of metal-oxide is the target oxidation occurring during the deposition, this determine first a non constant sputtering rate (as will be shown in the experiment characterizations) and an oxidized metal target after each deposition. Because of this oxidation each deposition is followed by a target cleaning which reduce the throughput in the fabrication, for this process RF power is used and the shutter is closed to limit the plasma on the target area and avoid any deposition on the substrate holder which is generally empty during this step. An example of oxidized targets is shown in figure 4.11, after cleaning the result is the one shown in figure 4.10c.

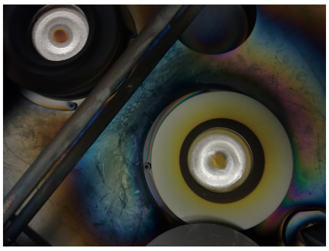

FIGURE 4.11: Oxidized metal targets after reactive sputtering deposition.

Another aspect reducing the throughput of the machine is the fact that a prechamber is missing, for this reason everytime a new sample has to be loaded into the chamber this has to be entirely vented (brought back to atmospheric pressure and opened) and repumped again for a time which last around the entire night. Moreover everytime the chamber is pumped after the venting is necessary to outgas it, during the outgas the walls of the chamber are heated to desorb the species which during the contact with ambient air have adsorbed on the walls.

4.2.2 Protocol

As said in the previous chapter this sputterer machine is less automated compared to conventional industrial nanoscale fabrication machines, this because it leaves more degrees of freedom to the user especially in a research environment. For our experiments were followed a sputtering recipe previously developed at IBM. Before loading, the substrates needs to be adapted to the sputterer mask shown in figure 4.12. Wafer shown in figure 4.7a is then cleaved in 7 squares of 5 IDEs each with a specific size; for these in addition to the figure 4.12 are added some other masks which shadow the connection wire where will be deposited the final contacts. Squares of the same shape are obtained out of Silicon - Silicon dioxide regular wafer, these are loaded on the mask and will act as witness wafers which will further be used for SEM, TEM and XRD analsysis. Additionally on the mask (attached with kapton to withstand the conditions), are placed some graphite chips which will be used in compositional analysis like RBS and XPS. The mask can fit up to 4 substrate squares, depending on the experiment more or less IDEs or witness squares are loaded.

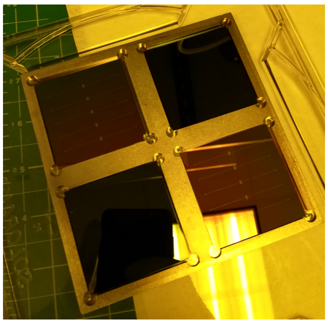

FIGURE 4.12: Sputterer mask used in the sputter deposition. In this case 2 IDEs squares and 2 witness wafer squares have been added, the further mask requested for contact shadowing of the IDEs is not shown.

Once the mask is ready, is loaded in the holder, the chamber is closed and the the rough pump is started, at this point the pressure will start decreasing down to a low pressure level such that the high-vacuum pump start functioning. From the pump switching the machine will take the entire night to reach the desired low pressure level (generally 10^{-7} *Torr*), this value is fundamental to obtain a clean process (and not for the deposition), indeed (as mentioned before) during this step the chamber walls are heated for some hours to desorb away the species adsorbed during the venting. Before starting the deposition it is important not only that the pressure has reached the desired value but even that the chamber walls have return to the ambient temperature, otherwise we run the risk to integrate unwanted species on our film or obtain a film morphology different from the expected one. Indeed in order to avoid a crystal film, deposition is made on the ambient temperature substrate which is less favored for crystallinity. Another condition adopted for the film requirement of porosity is a pressure higher than the one used in crystalline sputtered films. A fundamental step is to turn on the substrate rotation, this is fundamental to obtain a uniform process on the substrate. Before starting the deposition it is necessary first to clean the substrate of course still taking advantage of the machine plasma. The voltage generator used in this case is a RF one since the substrate is non-metallic. First the pressure is brought back to a specific value in 10^{-3} *Torr* order (the entire protocol from now on will work around this order ofr magnitude for the pressure), the Argon flow is then introduced to the chamber and set as well as the RF generator power setpoint. When the power is enabled to the chamber the plasma is created cleaning the substrate, a couple of seconds are sufficient for this process. Disabling the power is at this point possible to set the conditions for metal-oxide deposition. First the Oxygen is enable to the chamber, then its flow and the Argon flow are set to the specific value to obtain the desired stoichiometry. For the deposition the DC power is generally used, the use of the RF power is possible as well but the recipe is not developed for this type of deposition. Once the right pressure is set, at this point it is possible to ignite the plasma, the power is first enabled from the generator to the chamber turning on the plasma, this power is then ramped up slowly up to the deposition value. This power ramping is fundamental in order to do not create stress which will break the metallic part. At this point the shutter are still closed and nothing is depositing on the substrate, when the shutter is opened the substrate deposition starts, the shutter will be closed again after the deposition time has lasted. Since the recipe is calibrated to obtain a deposition rate of 1 nm/min the deposition time is equal to the desired film thickness in nm (i.e. 10minutes - 10nm), this is valid for both the metal-oxides to deposit which differ in the recipe uniquely from the deposition parameter values. Once the deposition is finished and the shutter is closed it is necessary to ramp down again the power (to avoid thermal stress) before disabling it. Before venting the chamber the gases are disabled to the chamber and pressure valve is set to open, moreover at this point the substrate rotation is no longer necessary. When the chamber is vented the pump is stopped and the venting mechanism brings the chamber pressure to the atmospheric one injecting Nitrogen. As mentioned before after each deposition the sputtered targets are oxidized and needs a further cleaning step. As for the deposition protocol the cleaning is made after pumping down the chamber (with corresponding outgasing) overnight. In this procedure Oxygen is of course requested since we are just sputtering the substrate, moreover since the material is oxidized on the surface RF power is necessary. A recipe with specific parameter values was developed for the cleaning as well.

4.3 Gold contact deposition

After the sensing layer deposition to obtain a testable device is finally added the Gold contacts visible in figure 4.1.

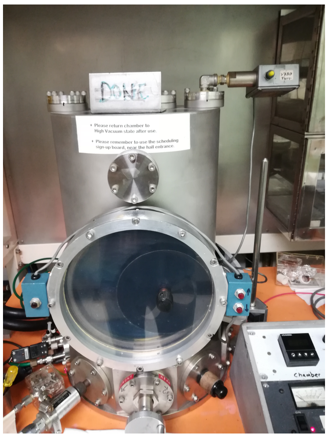

FIGURE 4.13: Thermal evaporator used for the Gold contacts deposition.

The substrates are loaded with the specific mask in the machine where Chromium and Gold crucible are added. As in the e-beam evaporation the Chromium is added just to favor the Gold adhesion, 100 nm of the second follow few nm of the first; this guarantees that when the probing station needle stretch the contact surface the electric connection is still possible. This machine works in a simple way, being vacuum based a first pumping step is requested, evaporation occurs thermally heating the metal with a voltage. Deposition is monitored by means of the QCM (quartz crystal micro balance) and the thin film controller. With the Gold contacts the devices are finally ready to be tested, to fit the single devices into the chamber is necessary to cleave and separate in five devices the substrate square handled. An images of a real final fabricated sensor is shown in figure 4.14, as you can see (because of the colors) between the center and the edges of the device a clear thickness step is present, this is the border between the sensing layer area and the substrate.

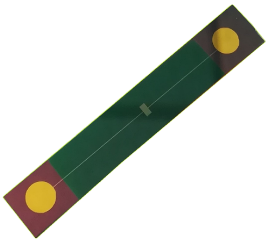

FIGURE 4.14: Gas sensing device obtained from fabrication and used for testing.

4.4 Gas sensing system

Sensing devices are tested in a testing lab where the measurement setup is placed over an optical table, the entire system is shown in figure 4.15.

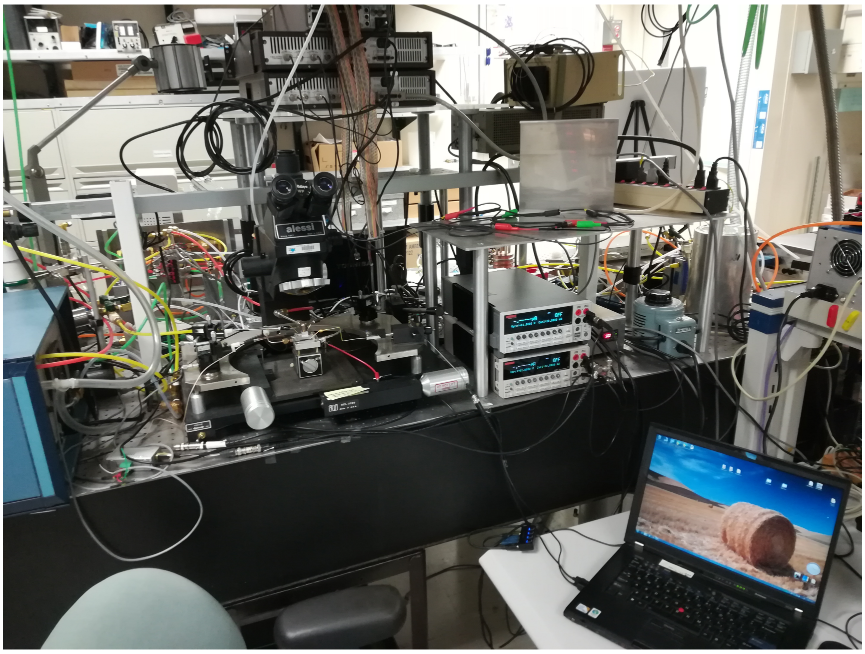

FIGURE 4.15: Gas measurement setup inside the testing lab.

The setup is general composed of chamber placed in a probe station; while the former is connected with a gas controlling system the latter is instead connected with the measurement and control instruments interfaced with the laptop. As you can see from figure 4.16a the chamber is composed of an Aluminum base on which the devices are sitting, above the devices still an Aluminum lead cover them without sealing. In this lead an inlet connects the chamber volume with the analyte (gas) coming from the gas control system. The Aluminum based is connected from one side with a heater and from the other with a thermocouple, these two are fundamental to control the temperature of the device and consequently of the gas sensing mechanism. The chamber has the limit capability of two devices, which limits the testing throughput, an additional defect is the fact the chamber is not perfectly sealed, this determine of course a minimum influence from the lab atmosphere; a partial solution is to use a consistent amount of incoming flux (around 500 sccm) during the testing to try reduce this effects. Because of this, the Sensor Group is working to a new version of this chamber, sealed and capable of testing 5 devices per time. Each of the device is connected through both the Gold contacts to the probing needles which are then connected to each single sourcemeter, one of the connection represents the positive while the other represenst the common which is then connected with the chamber and the optical table.

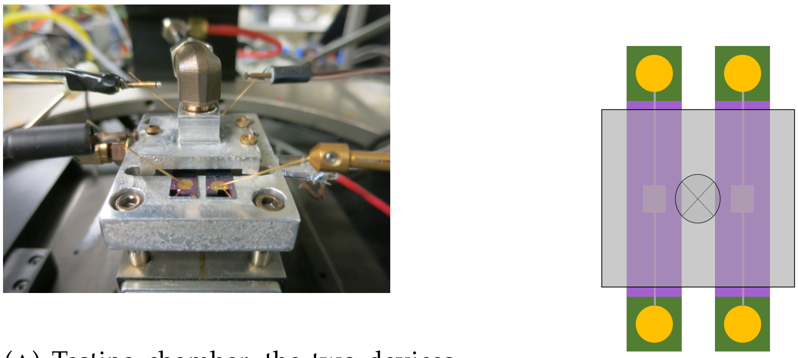

(A) Testing chamber, the two devices under test are connected with the probing needles. Above the chamber the analyte flux coming from the gas controlling system. Adapted from: Segantini, 2017.

(B) Representation of two sensing devices under test inside the chamber. The circle with the cross represents the analyte inlet to the chamber.

FIGURE 4.16

To test the devices it is used a mix of synthetic air and vapor coming from an evaporation oven, the role of the gas control system is to set the different flows of the system in order to obtain a desired concentration given by the ratio of analyte over air. The air used in this experiment is "synthetic air", the term "synthetic" refers to the fact that it is generated by a machine mixing Nitrogen and Oxygen and removing humidity. This allows to obtain more reliable results than using ambient air which is additionally influenced by the elements present in the atmosphere of the testing lab. For what concern the analytes in the current system, it is possible to test up to three different compounds: Acetone ($(CH_3)_2CO$), Ethanol (C_2H_5OH) and Toluene (C_7H_8). Vapors of these gases are obtained through two evaporation ovens: a Vici Metronics Dynocalibrator with two oven chambers and an Owlstone OVG-4 with a single oven chamber. The way the sources are connected to the sample and to the other components of the gas control system is shown in figure 4.17.

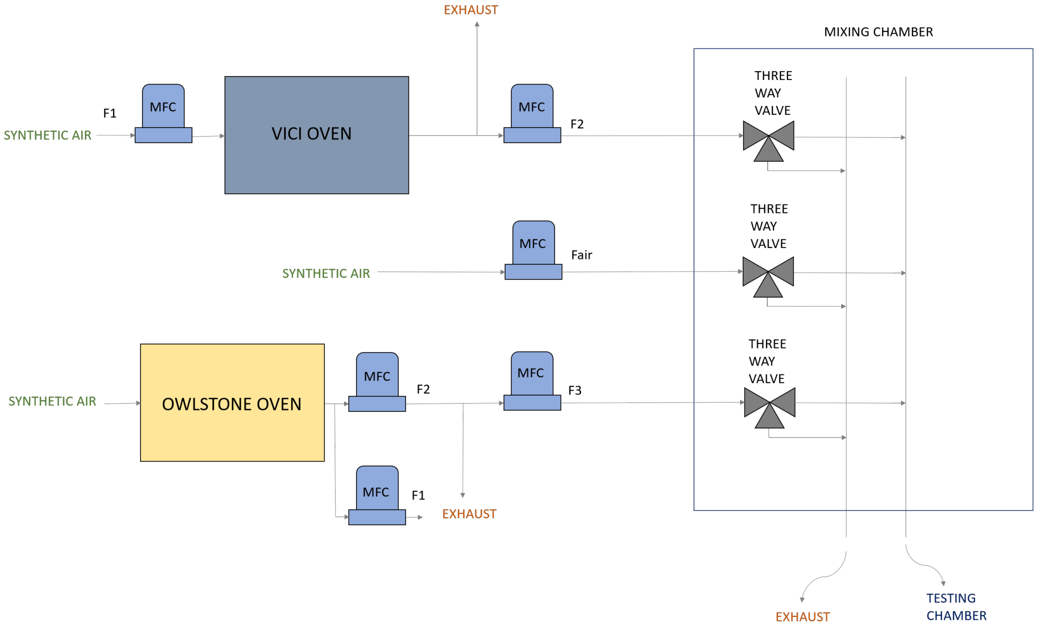

FIGURE 4.17: Scheme of the gas system used for the testing of the device.

The gas flow arriving to the testing chamber comes from the mixing chamber where the final mixing of analyte and synthetic air occurs. Within this chamber we find three different branch lines each of which can be connected (by means of a three way valve) to the testing chamber or to the exhaust line (which take the flux out of the building). All the three way valves which control this mixing are connected to a switching box controlled by the laptop connected as well to all the mass flow controllers (MFCs) present in the scheme except F1 coming from the Owlstone oven. It important to remember that a MFC is a device able to control the value of a flow moving from its input to its output, however to make this flow to exist and the device work properly is necessary to have a positive difference of pressure between output and input, for this reason in our system synthetic air comes from a higher pressure zone while exhaust from a lower pressure zone. Moving back to the mixing chamber for what concern the synthetic air line, this is connected directly to the synthetic air source through a MFC. VICI OVEN contains both at its input and at its output a MFC remotely controllable by the laptop, additionally an exhaust connection at its output is necessary to avoid a pressure instability and flux inversion. It is important to stress that the anayte in this oven as in the Owlstone case comes from the evaporation tube contained inside the ovens, this in physical terms are two flows which sum up. While VICI OVEN allows the control of the oven input in the OWLSTONE this is not possible, in this line the MFCs which control the F2 and F3 flows are the only controllable remotely by the laptop, F1 is instead set by a know knob on the oven panel. Since F2 and F1 are set by the user, the input flow of the oven (coming from the synthetic air generator) is automatically determined as the sum of F2 and F1. The complexity of this system allow us to have more degrees of freedom on the final concentration, in particular for the two ovens we have two different concentration formulas.

For VICI OVEN:

$$Concentration[ppb] = K * \frac{R}{F_1 + R} * \frac{F_2}{F_2 + F_{air}}$$

$$R : evaporation\, rate\, [\frac{mol}{min}]$$

$$K : units\, correction\, factor$$

For OWLSTONE OVEN:

$$Concentration[ppb] = K * \frac{R}{F_1 + F_2 + R} * \frac{F_3}{F_3 + F_{air}}$$

$$R : evaporation\, rate\, [\frac{mol}{min}]$$

$$K : units\, correction\, factor$$

Considering the full control of F_1, F_2, F_3 the system allow us to reach large ranges of concentrations (from around 20 ppb to around 1300 ppb) which otherwise would be limited by the operating range of the single MFCs and the control on the evaporation rate. Indeed the evaporation rate of the evaporation tube represent a parameter which is hard to control in real time; to keep track of this value the evaporation tubes were weighted weekly keeping track of the weight lost over time, correspondingly the flows were adjusted accordingly to obtain the final desired concentration.

Moving to the electronic part section of the measurement setup, as mentioned before each of the two devices is connected to the positive and the common needle of the probe station which through a partial BNC cable are then connected to the source meter. A KEITHLEY 2400 and KEITHLEY 2401 sourcemeter are used in the setup and controlled by the laptop throught the GPIB port. Apart from the sourcemeter, the switching box and the MFCs, from the laptop it is possible to control even the chamber temperature controller, this is fundamental if you want to obtain the response of the device over a temperature range. On the laptop several Python scripts allow to interface easily with the instruments and to automatize the measurements.

4.5 Gas sensing protocol

In general when a new device is tested a general protocol is followed, for some experiments some of this protocol steps are not followed or are different; it is good habit in general to be coherent within the same set of experiments. According to this, it is possible to launch each test with the relative Pyhton script. The procedure followed is:

- Stabilization
- IVsweep measurement
- Leakage measurement
- Sensing measurement

The first three steps are generally made at 300°C, the Sensing measurement is instead done at different temperature condition, in general these temperatures used represents the sensitivity peak temperatures for this type of devices. Connecting the device from ambient temperature to the probe station and applying a voltage bias of 1V the current will show a behavior over time characteristics of this devices, an example is shown in figure 4.18

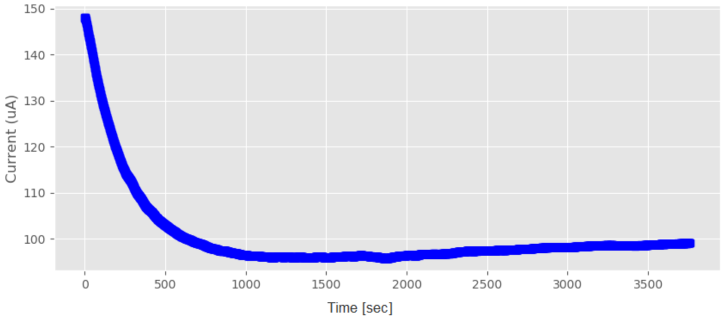

FIGURE 4.18: Example of current behavior of device connected to the 300°C probe station from ambient temperature and applying 1 V. As you can see after around 1 h from when the device is connected the current stabilizes.

In a time range of roughly 1 h the current decreases and slightly increases again reaching a stable point. In literature it is in general missing a full explaination of this phenomenon, however most likely it can be associated with the adsorption desorption of some species in the environment among which Oxygen is included. If a stable point is not reached and the measurement is started the final results will show a baseline drift which make the data evaluation difficult. For this reason as first step of the protocol the device is stabilized for around 1 hour at 300°C and 1V bias.

Once the device is ready to be measured it is fundamental to test whether is presents ohmic behavior, to do this the IVsweep is launched. During the IVsweep the current is measured for a variable applied voltage from -1V to 1V, the more the line is straight the more the behavior is ohmic, an example of of IVsweep result is shown in figure 4.19.

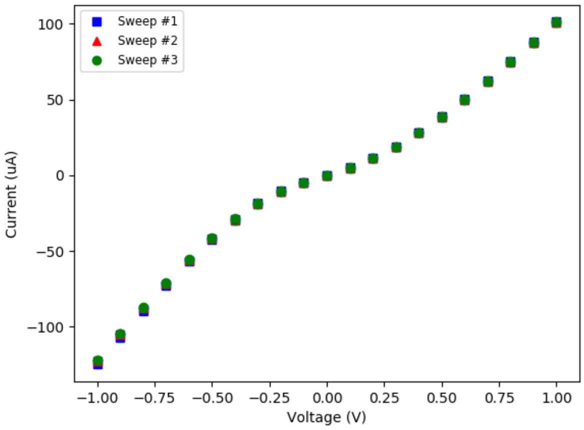

FIGURE 4.19: Example of IVsweep measurement of a sensor.

This measurement is fundamental because, if the behavior is asymmetric than a p-n longitudinal current is present, if the behavior is symmetric but non-linear than potential barriers, either at the electrode-film interface or within the film itself (grain-to-grain) as expected exists.

Since during the measurement even the device substrate is connected with the ground (GND) of the system, we run the risk of measuring a leakage current if the device has some internal leaks. Indeed as previously mentioned in section 4.1 the active part of the device is fabricated on 1 μm of SiO_2, however, for solution-based devices, the processing steps can damage the oxide or coat the edges of the substrate and create shorts. This does not happen for sputtered samples.
In all the cases is crucial to determine if any of these shorts are present in the device, for this reason the leakage current to the substrate is tested directly. Using the same principle and measurement code of the IVsweep but removing the GND needle from the Gold contact the leakage can be measured. So far no consistent leakage current has even be found on sputtering deposited device, in the case of solution based devices a leakage can more easily found. An example of leakage measurement on a not-leaking device is shown in figure 4.20.

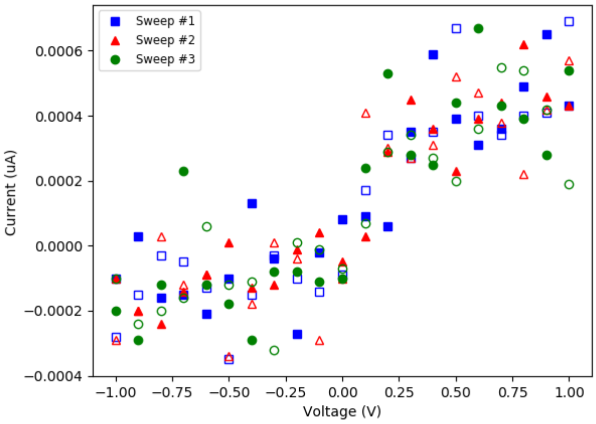

FIGURE 4.20: Example of leakage measurement of a sensor, no leaking is present in this case.

Sensing represents the core of the sensors testing, with this type of measurement it is possible to determine the sensor response as function of different parameters, in our case temperature, concentration and analyte: Acetone, Ethanol, Toluene. During the sensing the current is tracked over time, to do this a voltage bias of generally 1V is applied; another parameter which remains unchanged for the entire test is the incoming flow to the chamber which generally 500 sccm. This last value represents a value which as mentioned in the first of the chapter guarantees a negligible influence from the environment. While the current is measured, the device undergoes three different phases which can be summarized as:

- Baseline measurement: No analyte but just synthetic air is present.
- Gas sensing: Analyte is introduced in the chamber, the current/resistance of the device will change until reaching the steady state.
- Recovery: Analyte is removed and current/resistance of the device will move back to the baseline value (it is not always the case).

It is important to stress that since the voltage is constant for the entire measurement either referring to current or resistance is effectively equivalent, as we can easily convert from one parameter to the other. An example of sensing measurement (resistance) is shown in figure 4.21 where the different phases are highlighted.

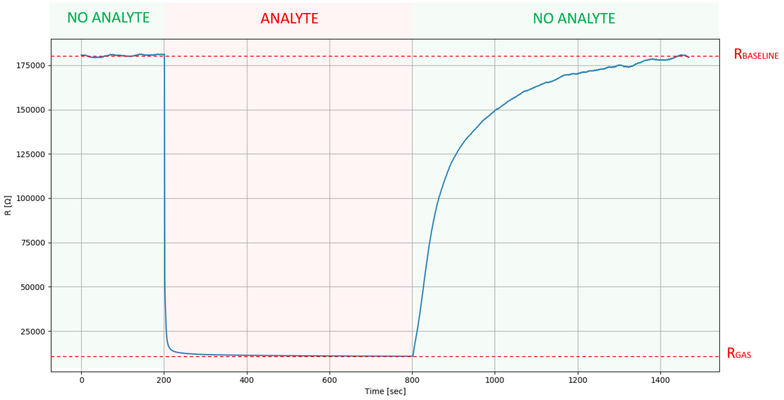

FIGURE 4.21: Example of sensing measurement plot. Resistance is tracked over time while the device undergoes the three different analyte phases.

4.5.1 Design parameters

Different gas sensor designers have different performance parameters to refer for their devices, in some case no information on the response is lost between them. To quantify the device performance of a sensing curve as the one shown in figure 4.21 several options are possible. The most important values to extract from the curve in figure 4.21 are $R_{baseline}$ and R_{gas}. The first is of course obtained from the baseline measurement from which an average value over the points is extracted to get rid of the slight fluctuations. The second is obtained from the gas exposure phase, in this case the steady-state value of the resistance is considered still averaged over the last few points. What is really problematic in this subject, is the adoption of a common way to define the sensitivity of the device, with a valid and easy to visualize parameter for both n-type and p-type devices and both reducing and oxidizing gases:

- n-type
  - Reducing gas: $R_{baseline} > R_{gas}$
  - Oxidizing gas: $R_{baseline} < R_{gas}$
- p-type
  - Reducing gas: $R_{baseline} < R_{gas}$
  - Oxidizing gas: $R_{baseline} > R_{gas}$

The most common methods of quantifying the response in literature (Pearce, 2003) are:

- Differential:

$$\Delta R = R_{baseline} - R_{gas}$$

- Relative:

$$S^* = \frac{R_{baseline}}{R_{gas}}$$

- Fractional:
$$S = \frac{R_{baseline} - R_{gas}}{R_{baseline}} = \frac{\Delta R}{R_{baseline}}$$

Clearly the responses, for a reducing gas on a n-type device, ΔR and S are positive and S^* is always bigger than one. Different is the case of still a n-type device which respond to an oxidizing gas where ΔR and S are negative and S^* is always smaller than one. The opposite situation occurs for a p-type gas, making the performance comparison between different gases and device difficult. In general since our experiments are all based on reducing gases (Acetone, Ethanol and Toluene) and n-type devices these parameters can be used without too many problems.

In general for a sensor, sensitivity represents the change in the output for a change in the input (Fraden, 1996, Johnson, 1999). Correspondingly, for the gas sensors case the sensitivity (S) can be represented as:

$$S = \frac{\Delta y}{\Delta x}$$

Where Δy is the change of the sensor output parameter and Δx is the change in the odorant concentration. An example of this is shown in section 1.2.2, indeed for Quartz Crystal Acustic Wave (QCM) gas sensors, sensitivity is defined as:

$$S = \frac{\Delta f}{\Delta c}$$

Where Δf is the frequency shift and Δc is the concentration change of the odorant. In general for sensitivity several approaches are adopted from the authors; for our experiments we will used mostly the shown S^*.

Chapter 5

Metal oxide N-P stack

Starting from the developed sputtering technique shown in Chapter 4, the idea is to deposit on the IDEs several thickness combinations of SnO_2/NiO bilayer films, measure their perfomances and characterize the resulting films. In particular we are interested in understanding what happens if first we keep the SnO_2 thickness constant varying only the NiO one, then vice-versa keeping the NiO thickness constant varying the SnO_2 one. In both cases the Tin-oxide layer is the lower layer (right deposited on top of the IDEs) in the two oxides stack.
In addition to this thickness study, is investigated a fundamental aspect of MOX gas sensors: the annealing impact on the performance. Using Rapid Thermal Annealing (RTA) we want to analyze what is the influence of this process on freshly deposited devices, in particular using two different atmospheres.

5.1 Deposition

To investigate how the NiO thickness variation influences the SnO_2 perfomance has been chosen 5 consecutive NiO thicknesses from 0 nm (no Nickel-oxide) to 20 nm in steps of 5 nm, this for two constant thicknesses of SnO_2 equal to 35 nm and 70 nm. The choice of 35 nm and 70 nm for SnO_2 comes from previous studies of the research group which reported good sensitivity for such thin-film gas sensing layers. The thickness values for NiO comes instead from the interest in a continuos/semi-discontinuos film to aim for a geometry like the one shown in figure 5.1, similar to the one of Woo et al., 2012.

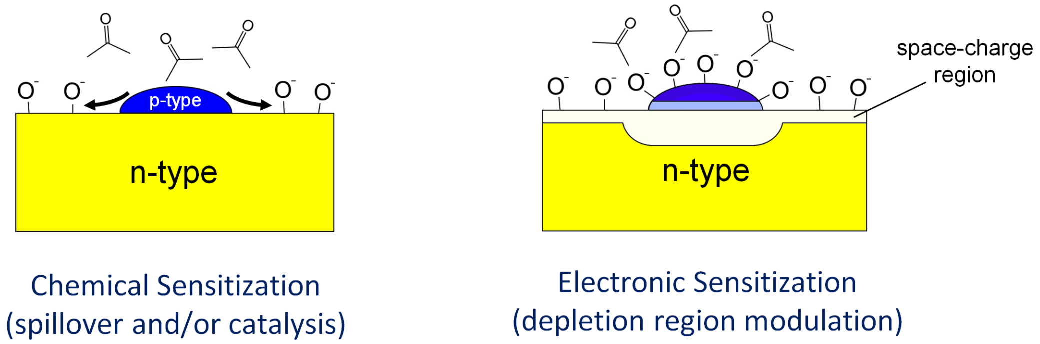

Chemical Sensitization (spillover and/or catalysis)

Electronic Sensitization (depletion region modulation)

FIGURE 5.1: Chemical and Electronic sensitization: possible physical explanations of the response enhancement in n-type gas sensing structures decorated with p-type ones. Adapted from *Sputtering of metal oxide semiconductor n-p stacks*.

Out of this idea several SnO_2/NiO bilayer films were deposited with the following thicknesses:

- 70 nm
- 70 + 5 nm
- 70 + 10 nm
- 70 + 15 nm
- 70 + 20 nm
- 35 nm
- 35 + 5 nm
- 35 + 10 nm
- 35 + 20 nm

It is important to specify that these thickness are nominal and are not exactly identical to the real ones, this since the deposition rate is not constant as it is assumed (and as will be further shown in the SEM results), a more precise control of the deposition rate is of course possible but requires a more extensive study not part of this one. Moreover in this study we are interested more in the relative (from thickness to thickness) effect of the thickness increase rather then the absolute one. In all the cases the deposited layer as will be shown in the next section are always fully characterized to get more precise numbers. As specified above we are not only interested in knowing how the NiO influences the SnO_2 behavior but even vice-versa: for this purpose a thickness of 20 nm for the NiO looks the more interesting, correspondingly additionally to the depositions with 20 nm thick NiO layer (+ 35 nm and 70 nm SnO_2), were deposited new bilayers with the following SnO_2/NiO thicknesses:

- 200 + 20 nm
- 20 + 20 nm

5.2 Rapid Thermal Annealing

In this study for each of the previous depositions were loaded on the machine three Silicon - Silicon dioxide square substrates each one containing 5 IDEs (devices) as shown in Chapter 4. One square (5 devices) was measured as deposited while the other two (5 + 5 devices) have gone through a rapid thermal annealing (RTA) process in different atmospheres. The used oven is an Allwin21 AccuThermo AW 810 RTP where power is generated by a lamp (figure 5.2). Gas lines allow us to anneal under different atmospheres, in our case we used either a N_2 atmosphere or a synthetic air one (80% N_2 and 20% O_2). It is important to stress that certainly the purpose of RTA in semiconductor industry is to activate dopants and repair damages from ion implantation; however in our case this allows us to reduce the amount of time required to have (theoretically) the same thermal budget than for example on a hot-plate. The purpose of this experiment is indeed first to see how the film changes and responds upon this annealing and second if this annealing could represent a fast alternative to the more time demanding conventional on-plate burn-in. In the recipe used the samples undergo the following cycle:

- Ramp: temperature is ramped from nominally 0°C to 600°C for 1200 sec.
- Steady: temperature is mainteined constant at 600°C for 30 min.
- Delay: temperature is ramped down from 600°C to nominally 0°C for 360 sec.

The two different atmosphere discussed are maintained for the entire process.

FIGURE 5.2: Allwin21 AccuThermo AW 810 rapid thermal annealer (RTA) used for the experiment.

5.3 Characterization

To have a first good insight of the deposited films, the samples were analyzed with a SEM (from ZEISS). Several images of different magnitudes (x10, x50, x100, x200) were selected with an impinging angle of 70°. Such configuration is good to estimate the profile of the layer but limitate of course the top view of each sample. Figure 5.3, 5.4 and 5.5 show these SEM measurements respectively for the bilayers respectively made of nominally 70 nm thick SnO_2, 35 nm thick SnO_2 and 20 nm thick NiO.

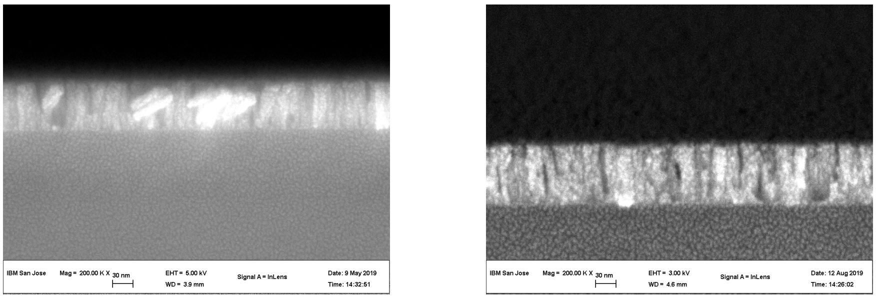

(A) nominally 70 nm SnO_2, SEM measured total thickness ≈ 79 nm.

(B) nominally 70 nm SnO_2 + 5 nm NiO, SEM measured total thickness ≈ 96 nm.

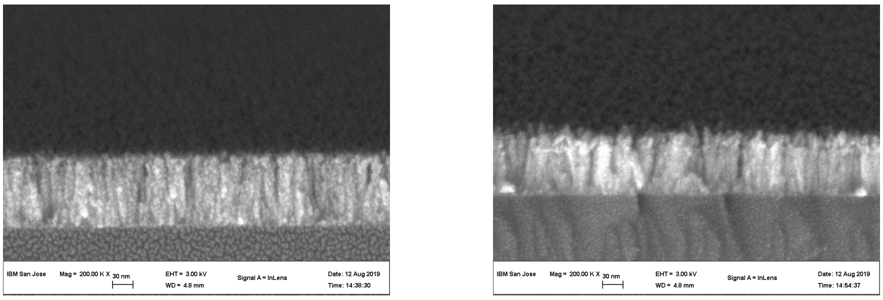

(C) nominally 70 nm SnO_2 + 10 nm NiO, SEM measured total thickness ≈ 113 nm.

(D) nominally 70 nm SnO_2 + 15 nm NiO, SEM measured total thickness ≈ 97 nm.

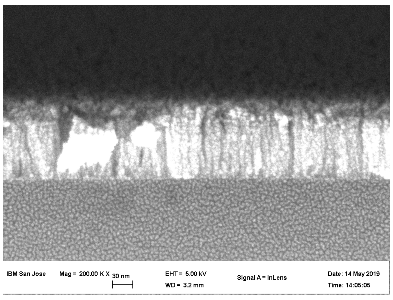

(E) nominally 70 nm SnO_2 + 20 nm NiO, SEM measured total thickness ≈ 104 nm.

FIGURE 5.3: SEM images corresponding to 70 nm SnO_2 + NiO bilayer depositions of different Nickel-oxide thicknesses. Images are taken at 70° with respect to bilayer cross-section, the measured thickness reported is already scaled by the trigonometrical factor.

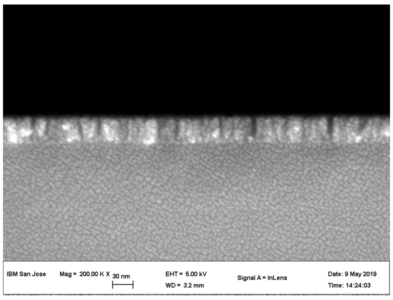

(A) nominally SnO_2, SEM measured total thickness ≈ 43 nm.

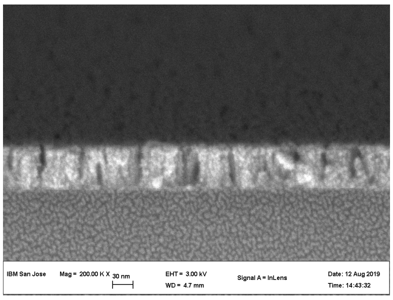

(B) nominally 35 nm SnO_2 + 5 nm NiO, SEM measured total thickness ≈ 68 nm.

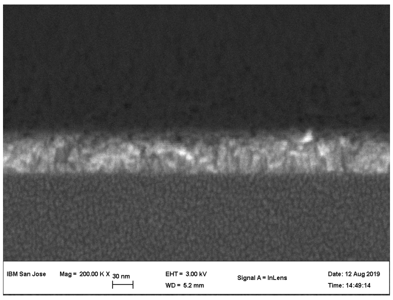

(C) nominally 35 nm SnO_2 + 10 nm NiO, SEM measured total thickness ≈ 64 nm.

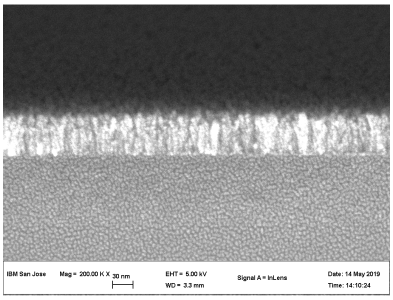

(D) nominally 35 nm SnO_2 + 15 nm NiO, SEM measured total thickness ≈ 63 nm.

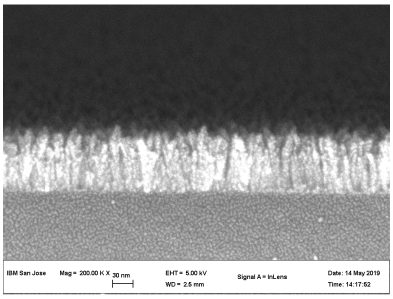

(E) nominally 35nm SnO_2 + 20 nm NiO, SEM measured total thickness ≈ 87 nm.

FIGURE 5.4: SEM images corresponding to 35nm SnO_2 + NiO bilayer depositions of different Nickel-oxide thicknesses. Images are taken at 70° with respect to bilayer cross-section, the measured thickness reported is already scaled by the trigonometrical factor.

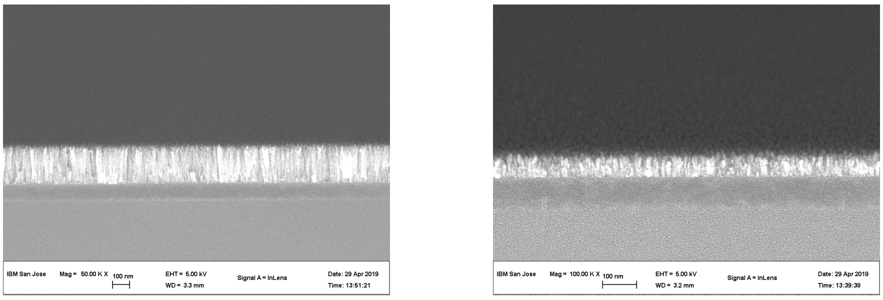

(A) nominally 200 nm SnO_2 + 20 nm NiO, SEM measured total thickness $\approx$ 229 nm.

(B) nominally 20 nm SnO_2 + 20 nm NiO, SEM measured total thickness $\approx$ 63 nm.

FIGURE 5.5: SEM images corresponding to SnO_2 + 20 NiO bilayer depositions of different Tin-oxide thicknesses. Images are taken at 70° with respect to bilayer cross-section, the measured thickness reported is already scaled by the trigonometrical factor.

As you can see, in the figures caption, additionally to the nominal thickness, is specified the one measured with the SEM specific tool. The discrepancy between these two values of the thickness is mainly related to a non-uniform deposition rate from both oxides, probably associated to the oxidation of the sputtered target. While the SnO_2 deposition is more controlled (as you will see later in the TEM characterization of figure 5.8), the NiO less so, in addition for the latter the SEM thickness is harder to be estimated because of its rough morphology (as will be shown in TEM). In these SEM images the darker upper part represents the top surface of the sensing layer while the lower part represent the $Si - SiO_2$ substrate. In between you can clearly distinguish the sensing layer cross-section. As you can see the film shows good uniformity in all the depositions as well as a columnar like morphology. It is important to remember that such morphology is highly desired if compared to a compact one since favours gas diffusion through the entire structure, fundamental to have a high response from the device. To have an insight of the deposited layers composition the bilayer made of 200 nm thick SnO_2 + 20 nm thick NiO was characterized with the XPS, in addition to this was characterized its nominally equivalent sample annealed in the RTA in a synthetic air atmosphere (80% N_2, 20% O_2): the idea is to undestand if during this annealing process Oxygen gets integrated into the sample changing the stoichiometry. Resulting XPS spectrum of the two samples is shown in figure 5.6.

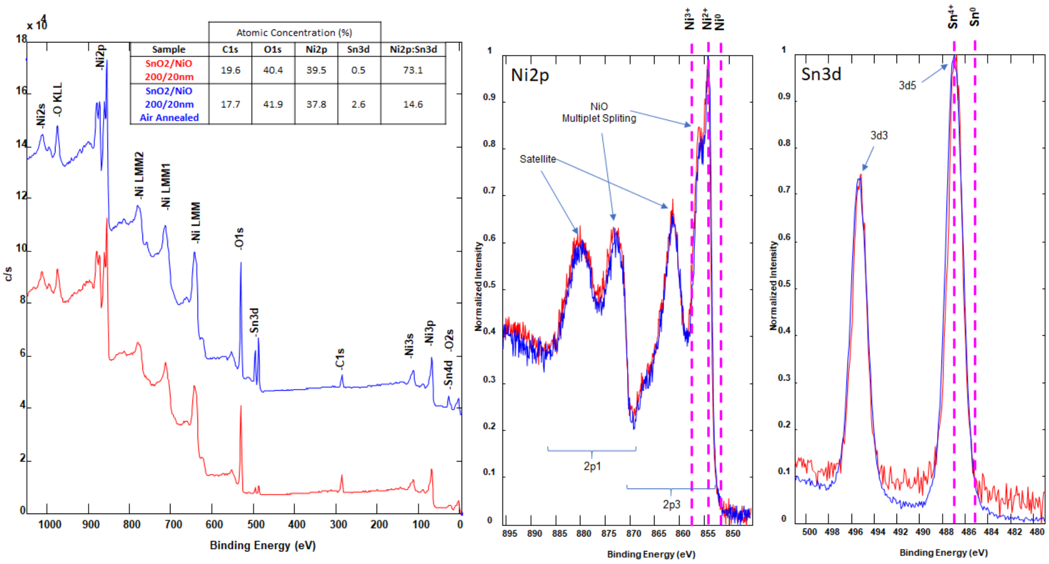

Sample	C1s	O1s	Ni2p	Sn3d	Ni2p:Sn3d
SnO2/NiO 200/20nm	19.6	40.4	39.5	0.5	73.1
SnO2/NiO 200/20nm Air Annealed	17.7	41.9	37.8	2.6	14.6

FIGURE 5.6: XPS analysis of two SnO_2/NiO bilayer samples 200/20 nm thick, one as deposited (not annealed), the second annealed in the RTA for 30 minutes at 600°C in synthetic air atmosphere (80% N2, 20% O2).

The presence in the spectrum of Sn^{4+} confirms the SnO_2 stoichiometry for the Tin-oxide. Characteristic peaks of Ni^{2+} confirm instead a NiO stoichiometry for the Nickel-oxide. Additionally to this, the XPS confirms the practical absence of any redox reaction occuring during the RTA annealing for 30 minutes at 600°C in synthetic air atmosphere.

Due to the intrinsic capabilities of the instruments is practically difficult to distinguish the two oxides phases which up to this point could be clearly intermixed: a TEM characterisation is then required. Since the SnO_2/NiO bilayer sample 70/5 nm thick is the one which aim the most at the depletion-spillover effect, this sample was analyzed with the TEM; this in addition to the N_2 RTA annealed and syntethic air RTA annealed counterpart to fully understand how these influence the film morphology.

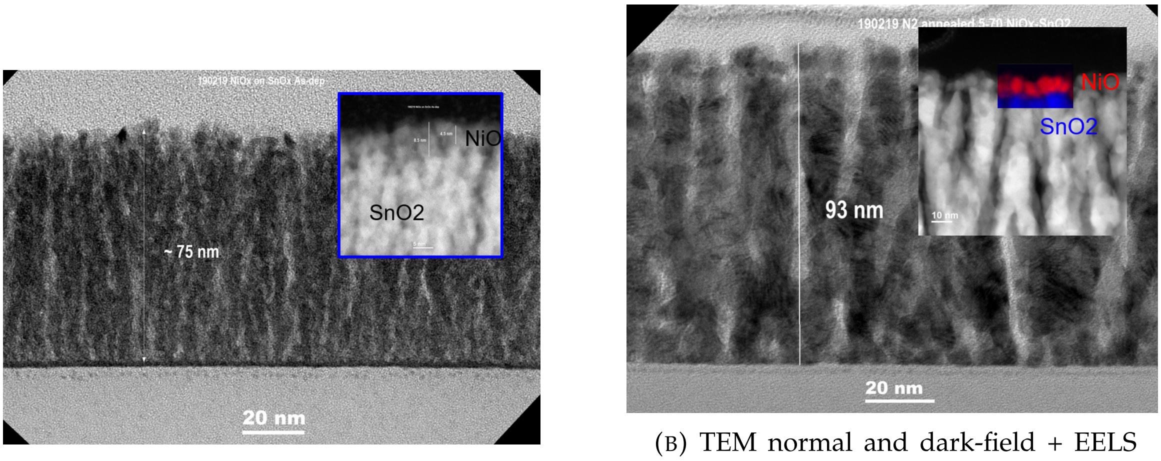

(A) TEM normal and dark-field imaging of nominal 70 nm SnO_2 + 5 nm NiO bilayer as deposited.

(B) TEM normal and dark-field + EELS imaging of nominal 70 nm SnO_2 + 5 nm NiO bilayer annealed in the RTA for 30 min at 600°C in N_2 atmosphere.

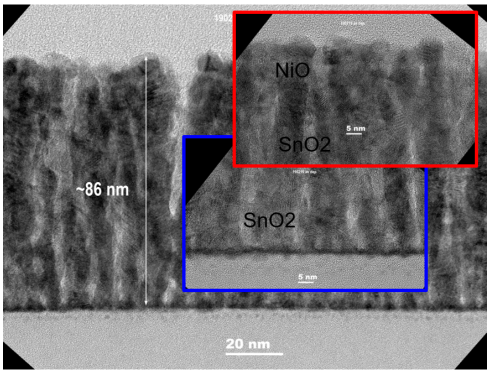

(C) TEM normal and high-resolution of nominal 70 nm SnO_2 + 5 nm NiO bilayer annealed in the RTA for 30 min at 600°C in synthetic air atmosphere (80% N_2, 20% O_2).

FIGURE 5.7: TEM images corresponding to bilayers of nominally 70 nm of SnO_2 + 5 nm of NiO in different post deposition conditions. (A) as desposited bilayer. (B) RTA annealed for 30 min at 600°C in N_2 atmosphere. (C) RTA annealed for 30 min at 600°C in synthetic air atmosphere (80% N_2, 20% O_2).

Figure 5.7a shows the cross section image of this as-deposited sample, clearly the result is not unsual if compared to the SEM one; magnification however allows us to distinguish the single grains contour, since the image is given by the superposition of different grains the periodicity in the texture does not exactly represent the real one. The measured thickness of both SnO_2 and NiO perfectly match the nominal one. Still in the same figure is shown the dark field image which allows us to distinguish the NiO and the SnO_2. This last image is particularly interesting since does not show any mixing of the oxides which remain separated with the presence however of a surface contact. Moving to the RTA N_2 annealed version of the same samples shown in figure 5.7b we see how this process influences the morphology. As first consequence the process seems to have triggered a grains growth and consequent thickness increase; this is however hard to estimate since in the last experiment was found a consistent gradient in the thickness deposition in the sputterer which might be the only reason behind this difference. Another evident effect of the RTA N_2 annealing is apparently the enhancement of the film cracking, cracks

within the columns seems to be larger if compared to the non-annealed case. Last partially evident effect of the process is the detachment of the two oxides. While in the as-deposited sample the two oxides have a good contact (without mixability), in this case (RTA N_2) the two phases show a barely visible detachment consequence of the de-wetting. In figure 5.7c is visible the result of the same (RTA) annealing in synthetic air (80% N_2, 20% O_2), the comments on the RTA N_2 annealed sample are still valid even for the synthetic air annealed one. Columnar-like morphology and crystallization are enhanced if compared to the as-deposited samples, the two oxide phases are detached.
TEM analysis was further extended to the bilayer nominally made of 35 nm thick SnO_2 and 10 nm thick NiO. Images of the different imaging results is shown in figure 5.8.

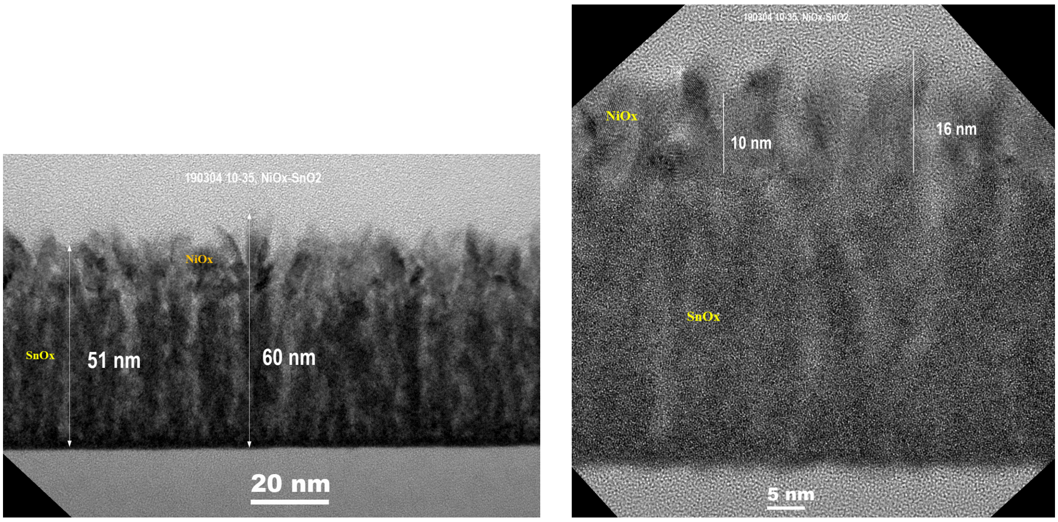

(A) Normal TEM image

(B) High-resolution image

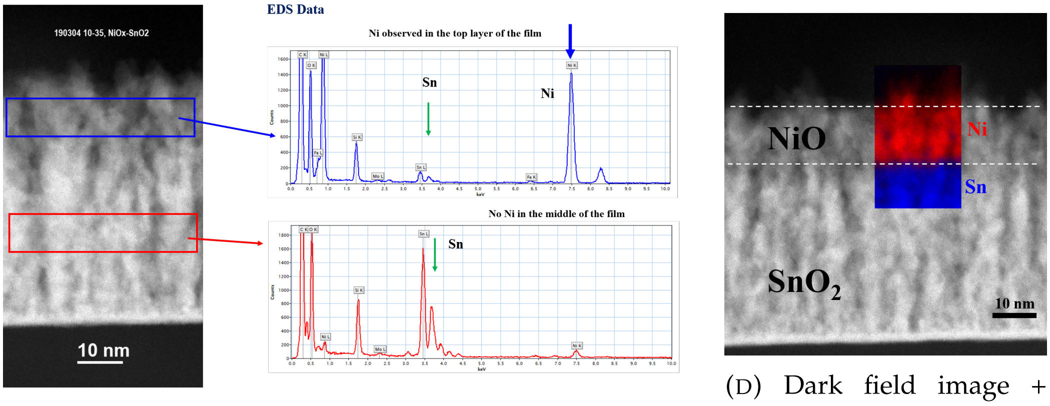

(C) Dark-field image and EDS spectrum

(D) Dark field image + EELS.

FIGURE 5.8: TEM analysis corresponding to a bilayer of nominally 35 nm of SnO_2 + 10 nm of NiO. (A) Normal TEM image. (B) High-resolution image. (C) Dark-field image and EDS spectrum. (D) Dark field image + EELS.

As you can see from figure 5.8a the morphology is similar to the previous figure 5.7, with a really rough but overall uniform film. Image 5.8b thanks to the resolution allows us to distinguish the two oxides, in particular we see that the regime of growth is consistently different, columnar-like for SnO_2 and flakes-like for NiO. For what concern the measured thickness if compared to the nominal one a discrepancy is present, additionally the *NiO* morphology does not allow to have a clear estimation of this. It important to mention that even if the deposited films show a real thickness which is a bit different from the nominal one, for our experiment we are more interested in the influence of the relative thickness between the samples. Still images 5.8c and 5.8d confirm the practical absence of a mixed interface between the two material but definitely a contact between them is present.

5.4 Sensing

To investigate the Nickel-oxide thickness modulation on 70 nm of SnO_2, two nominally equal devices (out of 5 for each square substrate as shown in chapter 4) were selected for each bilayer thickness, where the *NiO* thickness varies from 0 to 20 nm *NiO*. Sensing of these devices was done for around 200 ppb concentration of three different gases (Acetone, Ethanol, Toluene) at 300°C and 1V bias following the protocol of section 4.5. The $R_{baseline}$ over R_{gas} corresponding response is shown in figure 5.9.

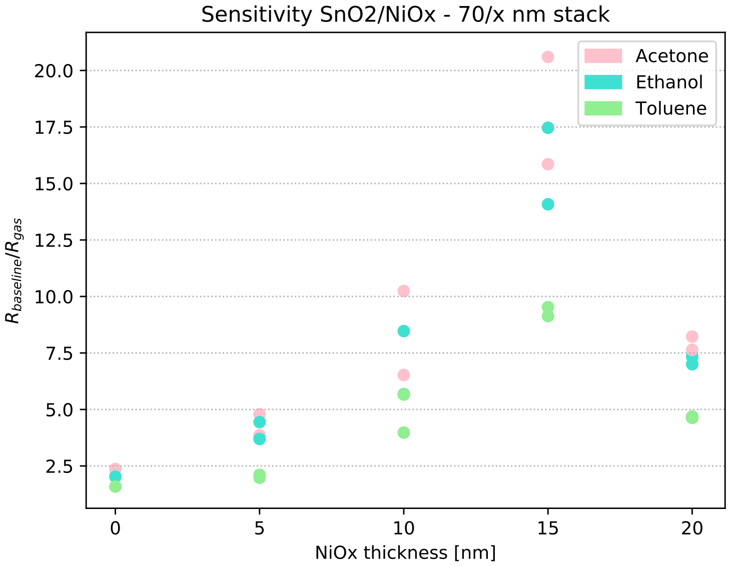

FIGURE 5.9: $R_{baseline}$ over R_{gas} response of different bilayers of 70 nm thick SnO_2 and variable *NiO* thickness for around 200 ppb concentration of the different gases at to 300°C and 1V bias.

Despite the lack of reproducibility between each nominally equal device we are able to see a trend. For a thickness of 15 nm the *NiO* shows the ability to enhance the SnO_2 perfomance for all the three gases. A possible simple explaination is the following. Adding first a 5 nm Nickel-oxide on top of the SnO_2 a space-charge-region (in the assumption of a good contact between the layers as it can be supposed from the TEM images) is generated, this region extends in both the layers acting as a non conductive region. For a thinner Nickel-oxide layer consequently its cross section is completely depleted, at the same time the SnO_2 is partially depleted too resulting in a thinner conductive path of the latter compared to the case where the Nickel-oxide is absent. Increasing the thickness from 5 nm to 15 nm increases correspondigly the depletion region in the SnO_2 and correspondingly the baseline resistance, this can be confirmed by the results shown figure 5.10.

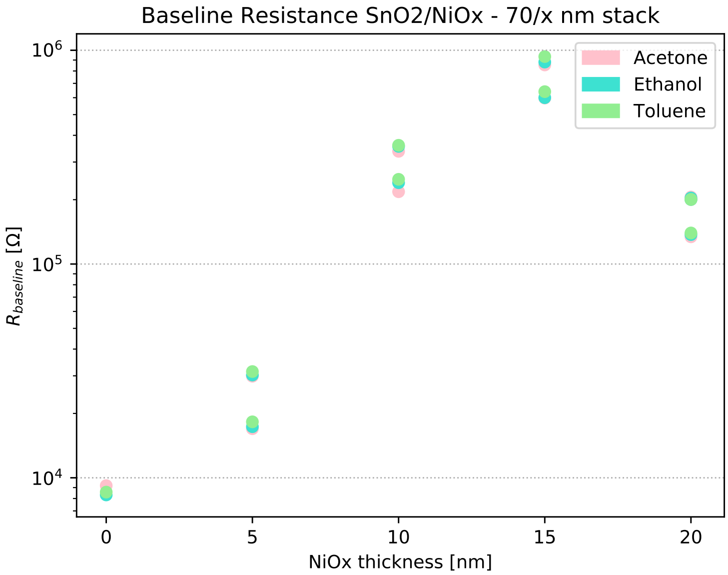

FIGURE 5.10: $R_{baseline}$ (semilogarithmic scale) of different bilayers of 70 nm SnO_2 and variable NiO thickness for around 200 ppb concentration of the different gases at to 300°C and 1V bias.

According to this model for a NiO thickness above 15 nm the space-charge-region does not cover completely the layer, a conduction path starts to create in the Nickel-oxide, decreasing consequently the baseline resistance. A simplified representation of this model is shown in figure 5.11.

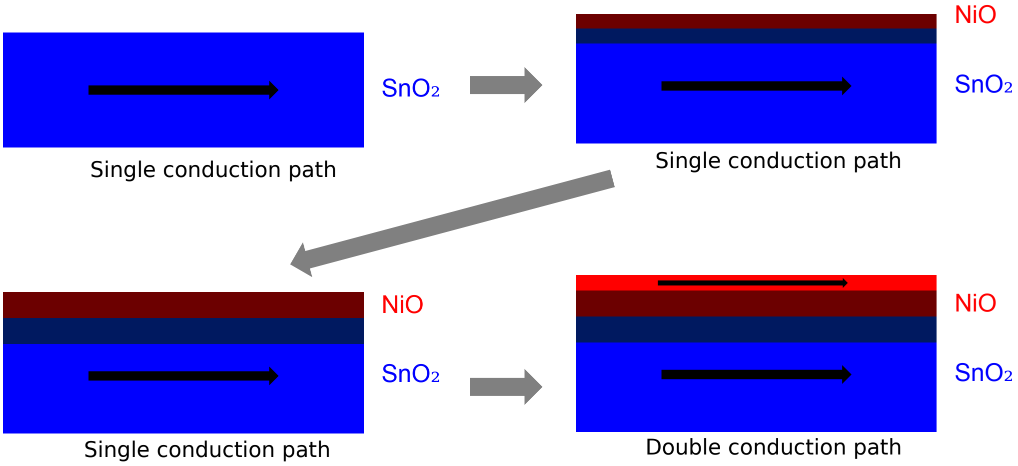

FIGURE 5.11: Representation of the SnO_2 depletion mechanism as hypothesis of the sensitivity dependence over the NiO thickness.

As shown the response enhancement correlates with a baseline resistance increase, this is partially true since in reality even the gas resistance is changing. While a possible physical explaination behind the baseline resistance increase was found, for the gas resistance increase case is definitely harder: several phenomena (gas trasduction, charge depletion, adsorption) are involved and correlated; so far as already shown in Chapter 3, none in literature has given a possible explaination yet. It is important to keep in mind that operating temperature is here 300°C, this information is important since as already explained the temperature is a fundamental parameter in such

devices and an enhancement of the response in such a temperature is not necessarily valid for other temperatures.
Parallel to the investigation of the Nickel-oxide thickness modulation on 70 nm of SnO_2, was investigated the same effect on a 35 nm thick SnO_2. In this case was measured all the five nominally equal devices for each bilayer thickness where the NiO thickness still varies from 0 to 20 nm but the 15 nm thickness is missing. Sensing of these devices was done just for around 200 ppb concentration of Acetone at 300°C and 1V bias following the protocol of section 4.5. The $R_{baseline}$ over R_{gas} corresponding behavior is shown in figure 5.12.

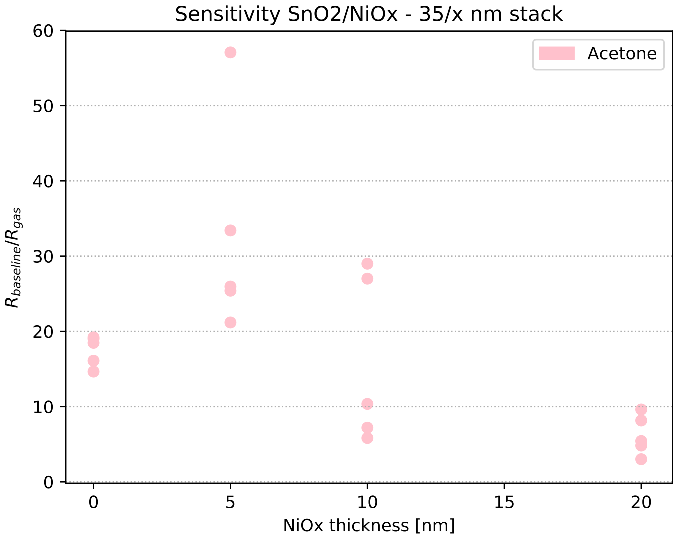

FIGURE 5.12: $R_{baseline}$ over R_{gas} response of different bilayers of 35 nm SnO_2 and variable NiO thickness for around 200 ppb concentration of different gases at to 300°C and 1V bias.

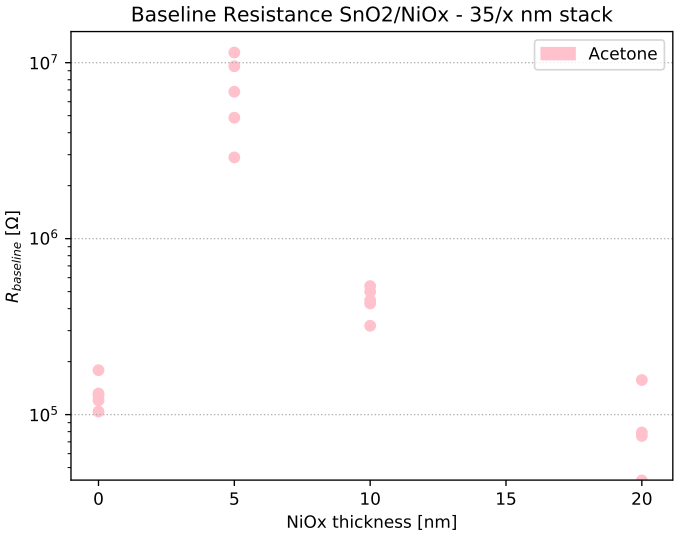

FIGURE 5.13: $R_{baseline}$ (semilogarithmic scale) of different bilayers of 35 nm SnO_2 and variable NiO thickness for around 200 ppb concentration of different gases at to 300°C, 1V bias and around 200 ppb concentration.

Analogous to the 15 nm in the previous case, a possible physical explanation for this response enhancement is that the 5 nm *NiO* generate a space-charge-region in the SnO_2 decreasing its resistance. Increasing further the *NiO* thickness a conductive path through the Nickel-oxide is created which lowers the baseline resistance again. As in the previous case the response enhancement is not solely related to the baseline resistance increase but even to the gas resistance: still some physical transduction phenomenon during the gas exposure still not defined.
To complete the thickness modulation analysis of the as-deposited samples, 5 devices nominally equal and made of a bilayer of 200 nm SnO_2 + 20 nm *NiO* the first and 20 nm SnO_2 + 20 nm *NiO* the second were sensing-measured still at 300°C for around 200 ppb of Acetone and 1V bias. Corresponding baseline resistance over gas resistance response was compared with the one of already measured *NiO* thick bilayer and is shown in figure 5.14.

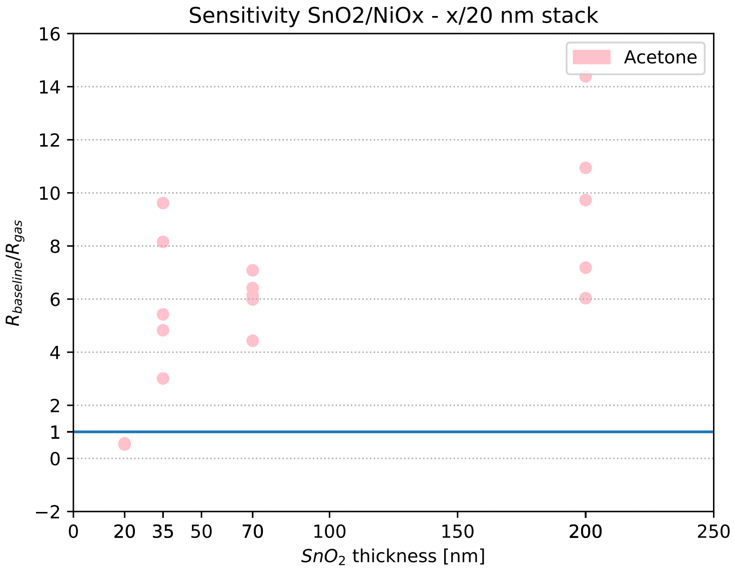

FIGURE 5.14: $R_{baseline}$ over R_{gas} response of different bilayers of 20 nm *NiO* and variable SnO_2 thickness for around 200 ppb concentration of Acetone at to 300°C and 1V bias.

Results show in this case the best response for the thickest film which however shows a relevant dispersion of the data. Interesting is the fact that for a SnO_2 thickness of 20 nm the device behavior is p-type with the gas resistance bigger than the baseline resistance: the response of all of these devices are all placed below the abscissa value equal to 1. As explained in section 3.3, if R_{gas} is bigger than $R_{baseline}$ (and sensitivity drops below 1) this is indicative of p-type behavior. Differently from the previous cases the baseline resistance does not follow the same trend response, in particular as you see from figure 5.15 its behavior is not consistent with the space-charge-region hypothesis formulated before. Lack of reproducibility still does not help to have a clear picture.

To further investigate the *NiO* modulation of SnO_2, the nominally equal but thermal annealed versions of the SnO_2/NiO bilayers with the Tin-oxide 70 nm and 35 nm thick were measured. Starting from 35 nm thick SnO_2 bilayer for each of the *NiO* thicknesses going from 0 nm (no Nickel-oxide) to 20 nm in steps of 5 nm (the 15 nm thickness is missing) were meaured 15 devices. Measurement was done still

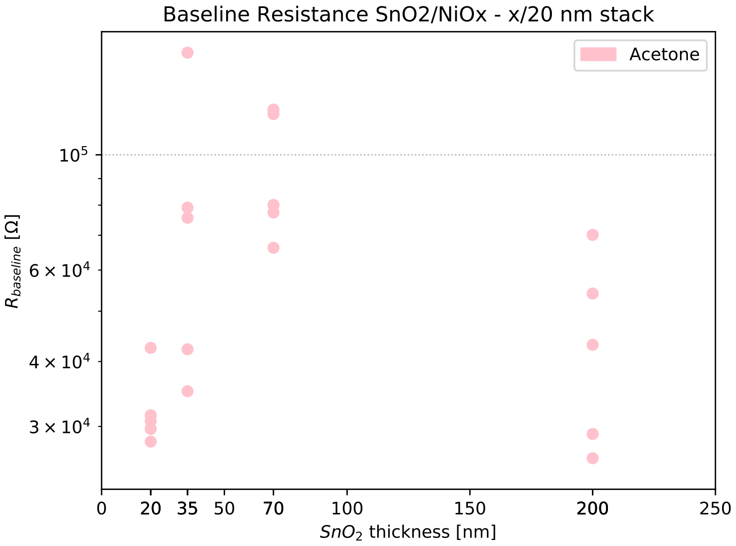

FIGURE 5.15: $R_{baseline}$ (semilogarithmic scale) of different bilayers of 20 nm NiO and variable SnO_2 thickness for around 200 ppb concentration of Acetone at to 300°C and 1V bias.

in around 200 ppb concentration of Acetone at 300°C and 1V bias. Five devices were measured as-deposited, five after RTA treatment in N_2 and the remaining five after RTA treatment in synthetic air (80% N_2, 20% O_2). Results of the baseline resistance over gas resistance response is shown in figure 5.16.

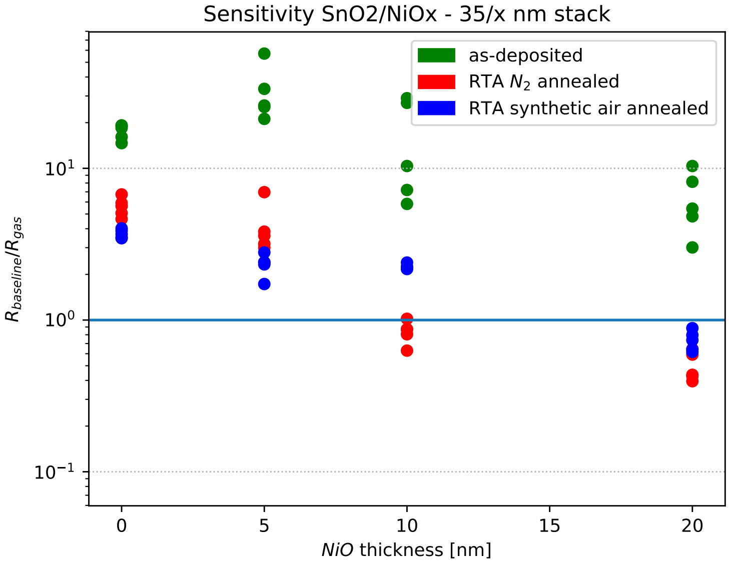

FIGURE 5.16: $R_{baseline}$ over R_{gas} response of different bilayers of 35 nm SnO_2, variable NiO thickness and different RTA annealing conditions for around 200 ppb concentration of Acetone at 300°C and 1V bias.

In general the annealing reduces considerably the devices sensitivity. Even in this case because of the lack of reproducibility between devices it is hard to define a perfectly clear trend, although it appears that the presence of NiO layers is not beneficial to the annealed device performance. As you can see, the thicker is the NiO

thickness the lower is the sensitivity, for such situation the SnO_2 depletion model hypothesized above can probably no longer be valid after this annealing. A possible explanation for this is that the SnO_2 and the NiO after this process completely detach, with the junction and the relative space-charge-region no longer present. This is probable especially if you consider the TEM results shown in figure 5.7, in which a de-wetting of the oxides is visible. An interesting result is the one of the annealed devices with a thicker NiO: for a 20 nm thick NiO the RTA N_2 and RTA synthetic air annealed samples show a sensitivity smaller than 1, as mentioned before this is indicative of p-type behavior. This is a clear sign that the current conduction occurs mainly through the p-type layer which for this thickness represents no longer a discontinuous film able to enhance and modulate the n-type layer but to conduct part of the current by himself. For such situation the responses from the two layers compensate to each other. Similar but not identical behavior is the one of the 10 nm thick NiO, here for the N_2 RTA annealed sample 4 devices out of 5 show inversion form p-type to n-type, for the synthetic air instead this behavior is not shown at all. This result is interesting since the two annealing atmospheres in this case show more than in the other cases to be consistently different. This last observation seems not in accordance at least with the XPS results of figure 5.6 where the synthetic air annealing in the RTA did not show any consistent change of stoichiometry with respect to the not annealed nominally identical version, consequently the same should be certainly valid even for the N_2 annealed version because of the inert characteristic of Nitrogen. Important informations are obtained from the baseline resistance, as you see in figure 5.17 the RTA annealing reduces consistently the conductivity (by 2-3 orders of magnitude).

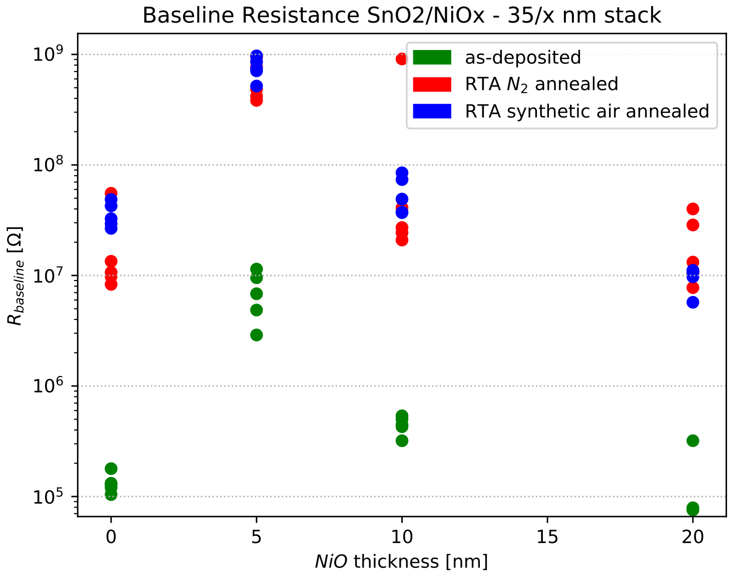

FIGURE 5.17: Baseline resistance (semilogarithmic scale) of different bilayers of 35 nm SnO_2 and variable NiO thickness for different gases; temperature equal to 300°C and voltage bias equal to 1V.

The explanation of this is straightforward, with the annealing the surface reconstruction occurs and the defects decreases which, are the base for the conduction of these otherwise non conductive materials. It is interesting to see that with respect to the not-annealed samples (where the baseline resistance has the trend on the sensitivity) the RTA annealed ones show a baseline resistance trend different from the one

of the sensitivity. Indeed if the bilayers are effectively detached the baseline resistance would be expected to be lower for the thicker films.
Starting from 70 nm thick SnO_2 bilayer for each of the NiO thicknesses going from 0 nm (no Nickel-oxide) to 20 nm in steps of 5 nm were measured 15 devices. Measurements were done still in around 200 ppb concentration of Acetone at 300°C and 1V voltage bias. Five device have been measured as deposited, five after RTA treatment in N_2 and the remaining five after RTA treatment in synthetic air (80% N_2, 20% O_2). Result of the baseline resistance over gas resistance response is shown in figure 5.18.

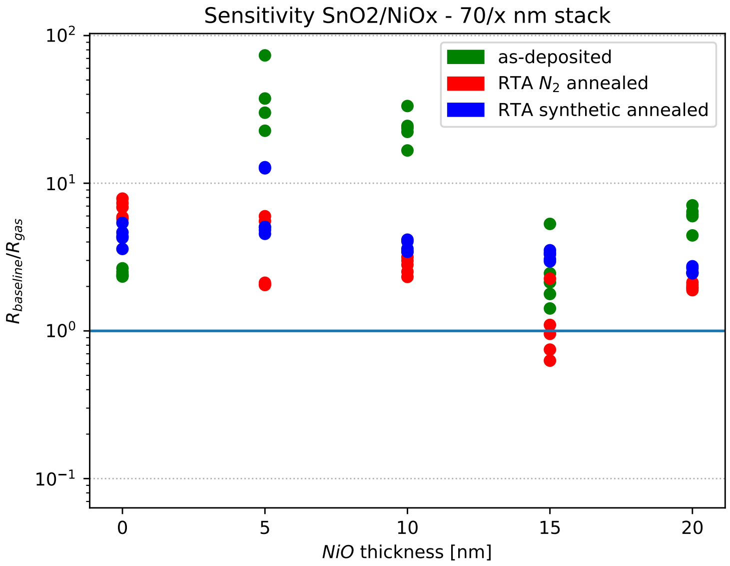

FIGURE 5.18: $R_{baseline}$ over R_{gas} response of different bilayers of 70 nm SnO_2, variable NiO thickness and different RTA annealing conditions for around 200 ppb concentration of Acetone at 300°C and 1V bias.

For what concern the as-deposited devices the results in this case show inconsistency compared to those shown earlier where the 15nm NiO showed the best response. For what concern the RTA annaled devices, the same trend shown above for the 35 nm thick SnO_2 bilayer is shown. Indeed the thicker is the NiO thickness the lower is the sensitivity, for such situation the SnO_2 depletion model hypothesized above can again no longer be valid after this annealing. The hypothesis of de-wetting of the oxides can be valid even in this situation. Interesting is the case of the 15 nm thickness for the Nickel-oxide, which shows a p-type behavior in case of Nitrogen annealing. It is certainly hard to give an explanation for the fact that these deposited devices (15 nm thick NiO) shown inconsistency with respect to the others, it is a matter of fact that user of the sputterer machine for this device was different from the one of the others but the sputtering recipe has remained however the same.

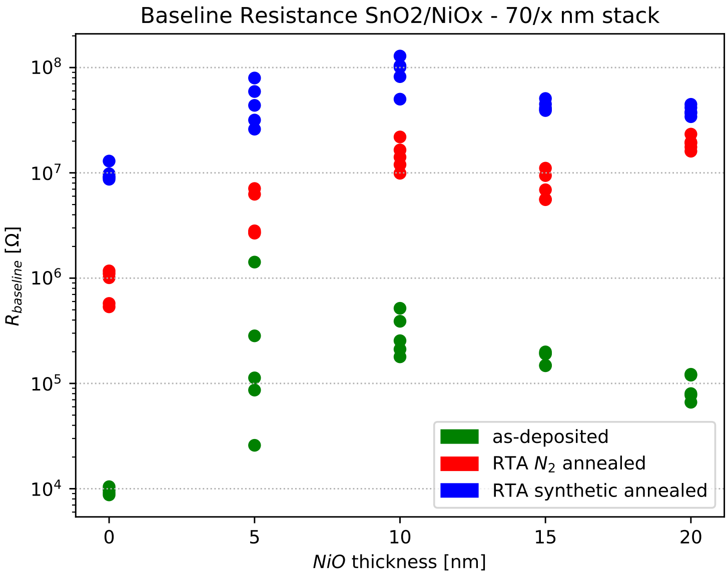

FIGURE 5.19: Baseline resistance (semilogarithmic scale) of different bilayers of 70 nm SnO_2 and variable NiO thickness for different gases; temperature equal to 300°C and voltage bias equal to 1V.

Even for this set of the devices (as for the 35 nm NiO case), the baseline resistance seems increase proportionally for each sample (by 2-3 orders of magnitude). This is shown in figure 5.19. Again this is most probably associated with surface reconstruction and defects decreases after annealing.

5.5 Conclusions

In this chapter was described the thickness systematic analysis of three different set of SnO_2/NiO bilayers. The idea was to see how, modulating the thickness of one of the two layers (while keeping the other constant), the response and characteristics of the devices is influenced. In addition it was investigated the influence of the Rapid Thermal Annealing (RTA) treatment on these devices at 600°C for 30 min in N_2 and synthetic air (80% N_2, 20% O_2) atmosphere. A first set of devices was fabricated with bilayers of 70 nm thick SnO_2 and a respective NiO thickness of 0, 5, 10, 15 and 20 nm. A second set of devices was fabricated with bilayers of 35 nm thick SnO_2 and a respective NiO thickness of 0, 5, 10 and 20 nm. In addition to the 70/20 nm and 35/20 nm thick SnO_2/NiO bilayers were fabricated a 20/20 nm and a 200/20 nm thick, this, to complete a third set of devices with bilayers of fixed NiO thickness and variable SnO_2 one. Devices were tested and characterized.

The most outstanding result shows that adding NiO on top of 70 nm of SnO_2 it is possible to enhance its response with a peak around 15 nm, where the sensitivity increases around 5 times for Acetone and Ethanol, and around 4 times for Toluene with respect to the NiO-less case. The same trend is followed by the baseline resistance, maximum at 15 nm: according to both results, a SnO_2 depletion model was hypothesized. According to this model, when the NiO is added to SnO_2, a space-charge-region is created, decreasing the Tin-oxide conduction section and consequently its resistance: this is translated into a response increase of the device, as a consequence of the modulation effect explained in section 3.3.1. According to our model, a further increase of the NiO to 20 nm creates an additional conduction path in the Nickel-oxide which decreases the modulation effect. A relevant accordance to this model was found in the TEM analysis and in the sensing of the set with 35 nm thick SnO_2, where both sensitivity and resistance show the same trend with a peak around 5 nm, in this case only Acetone was tested. In partial disagreement with the expressed model is the set with 20 nm thick NiO where, while the baseline resistance shows a maximum for the 70/20 nm thick bilayer, the best sensitivity is shown by the 200/20 nm thick one and further decreases in the thinner films. Most probably for such situation there is a more complex mechanism than the one described.

Results from the RTA annealing on the 35 nm thick SnO_2 set show the baseline resistance to increase for all the device by 2-3 orders of magnitude, this is coherent with the fact that annealing removes vacancies and defects decreasing the number of carriers. If this is in good agreement with the SnO_2 model hypothesized, the sensitivity in turn shows instead a different trend. Indeed, for all the RTA annealed bilayers with respectively 35 nm and 70 nm thick SnO_2, the Nickel-oxide seems to decrease the device response; with the 35/20 nm bilayer showing p-type behavior. A possible explanation is that p-type response of Nickel-oxide compensates (and in some situation, cancels) the n-type one of the Tin-oxide one, indeed as TEM shows, after both N_2 and synthetic air annealing the two layers seem to detach one from the other. As a consequence the space-charge-region, and in turn the SnO_2 modulation effect from the NiO, no longer exist. A further result shown by TEM it the cracks enhancement after both the annealing treatments.

In general, considering the "exploratory" nature of the experiment, good results have been obtained. What does not allow us to derive final conclusions, is the data dispersion and the lack of understanding in the undergoing mechanisms. For this reason more work need to be done in order to improve control and reproducibility in the fabrication process.
Fundamental for the NiO enhancement investigation would be to work on experiments which address the basic physical mechanisms occurring (like to demonstrate that a space-charge-region effectively is created) and define a model which can further be used in design. In this sense, the 35 and 70 nm thicknesses for the SnO_2 of the bilayer represent again good values for this investigation.
Despite the results from RTA were not optimal, a further investigation of the impact of this process can be considered for a lower temperatures (probably 400°C); a morphological analysis of this follows in the next chapter. Moreover working again on the same deposited and annealing device would be interesting to test stability over time, to see if effectively RTA annealing has good prospectives to be used on these devices and to further be used in design.

Chapter 6

Annealing systematics

As already discussed in Chapter 5 and section 3.2 annealing represents a key processing step in MOX gas sensors fabrication. The purpose of this experiment is to investigate the impact of several annealing techniques of three different MOX sensing films trying to find the optimal solution to apply on new devices. Differently from the Rapid Thermal Annealing (RTA) analysis of Chapter 5 this experiment is limited to a morphology characterization without IDEs measurement, at the same time, however, it is not limited to only RTA but to oven annealing and hot-plate annealing (further details in the next section).

6.1 Deposition & Annealing

Three different sensing layers were deposited with the sputterer using DC and RF power:

- 90 nm monolayer of SnO_2 deposited in RF but following the same stoichiometric (gases ratio), power and pressure conditions of the usual DC recipe of section 4.2.2. Within the experiment will be defined for simplicity as "90-RF".
- 70/10 nm bilayer of respectively SnO_2/NiO deposited in DC. Within the experiment will be defined for simplicity as "70/10-DC".
- 35/10 nm bilayer of respectively SnO_2/NiO deposited in DC. Within the experiment will be defined for simplicity as "35/10-DC".

It is important to mention that for 70/10-DC and 35/10-DC the specified thickness is the nominal one, while for 90-RF is the one measured with the SEM. Depositions were made on conventional Silicon - Silicon dioxide witness wafers.
After each deposition, the substrate was cleaved to obtain single pieces for each of the following annealing treatments:

- Rapid Thermal Annealing (RTA): performed both in N_2 and synthetic air atmosphere (80% N_2 and 20% O_2), with nominal temperatures of 400°C and 600°C for 30 minutes, ramp-up and ramp-down time was 3 minutes with steps of 50°C.
  The used oven is same Allwin21 AccuThermo AW 810 RTP of the experiment in Chapter 5, where power is generated by a lamp (figure 5.2).
- Hot-plate Annealing: performed in atmospheric air with nominal temperatures of 400°C for 16, 24 and 48 hours, the devices were directly put on the hot-plate without any temperature ramp. The hot-plate used is the Thermolyte one shown in figure 6.1b.

- Oven Annealing: performed in atmospheric air with nominal temperatures of 400 and 600°C for 16 hours, the devices were directly put in the oven without temperature ramp. The oven used is the Thermo Scientific one shown in figure 6.1b.

(A) Hot plate used for the annealing experiment. (B) Oven used for the annealing experiment.

FIGURE 6.1

Additionally to all the previous samples a single sample for each deposition was preserved to any annealing treatment (as-deposited) to be used as a reference.

6.2 Characterization

To fully characterize morphology and composition, the device were characterized with SEM, XRD and TEM. To follow, is a summary of the results based on the different annealing techniques followed by some considerations.

6.2.1 Not annealead

In figure 6.2 you can see the three films as deposited, no annealing was applied to these. Despite the layer in figure 6.2a was deposited in RF it does not show any difference in the morphology, with respect to the others DC deposited (figure 6.2b and 6.2c). As expected a columnar-like morphology is observed with a good degree of porosity. This similarity between RF-90 (6.2a), 70/10-DC (6.2b) and 35/10-DC (6.2c) prove that the presence of the NiO layer does not impact significantly the morphology of the underneath SnO_2. For what concern the XRD, for the three samples no diffraction peak was detected (flat spectrum) for this reason no image of the resulting spectrum is shown.

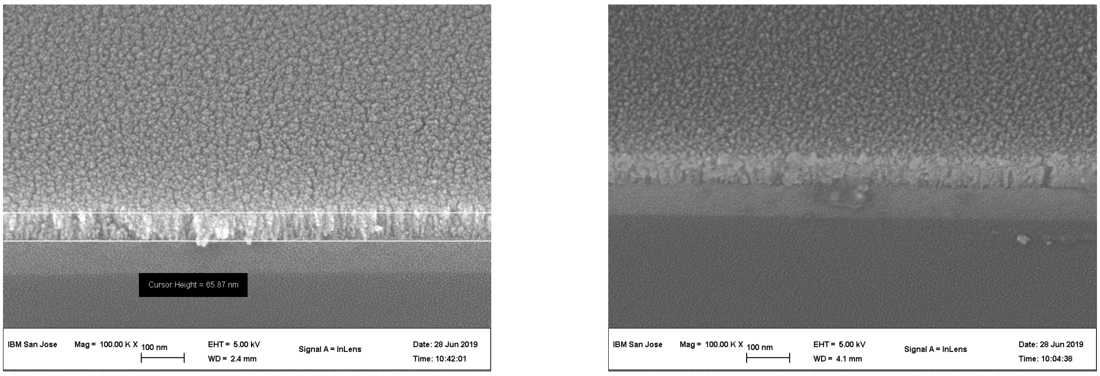

(A) SEM image of the 90 nm monolayer of SnO_2 deposited in RF.

(B) SEM image of the 70/10 nm bilayer of respectively SnO_2/NiO deposited in DC.

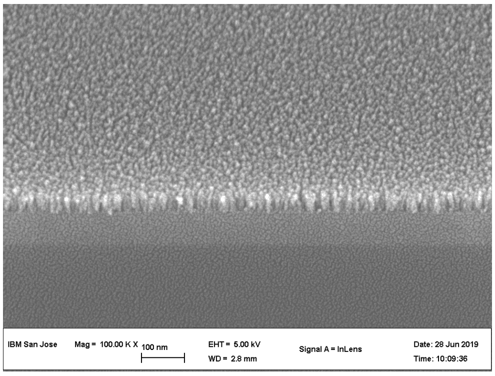

(C) SEM image of the 35/10 nm bilayer of respectively SnO_2/NiO deposited in DC.

FIGURE 6.2

6.2.2 RTA annealing

Since the results from both RTA annealing in synthetic air (80% N_2, 20% O_2) and N_2 atmosphere were consistently the same, only the one in synthetic air environment are reported.

400°C

As you can see in figure 6.3b after annealing the RF-90 film show crystallinity, compared to this almost no peaks are present in the 70/10-DC (figure 6.4b) and the 35/10-DC (figure 6.5b) films where the XRD pattern recognition tool finds however some doubtful presence of NiO and NiO_2.
Moving to the SEM images (figures 6.3a, 6.4a and 6.5a), as expected after the results of Chapter 5, the films show a slight presence of cracks almost absent in the 35/10-DC sample. A deeper insight of this cracks morphology is difficult to obtain, moreover this complicates any eventual diffusion reaction modelization of the film.

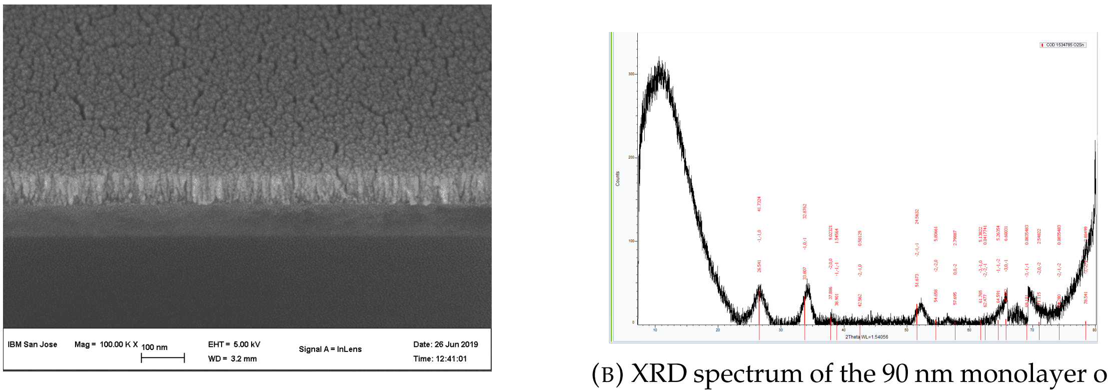

(A) SEM image of the 90 nm monolayer of SnO_2 deposited in RF and annealed in RTA for 30 min at 400°C.

(B) XRD spectrum of the 90 nm monolayer of SnO_2 deposited in RF and annealed in RTA for 30 min at 400°C.

FIGURE 6.3

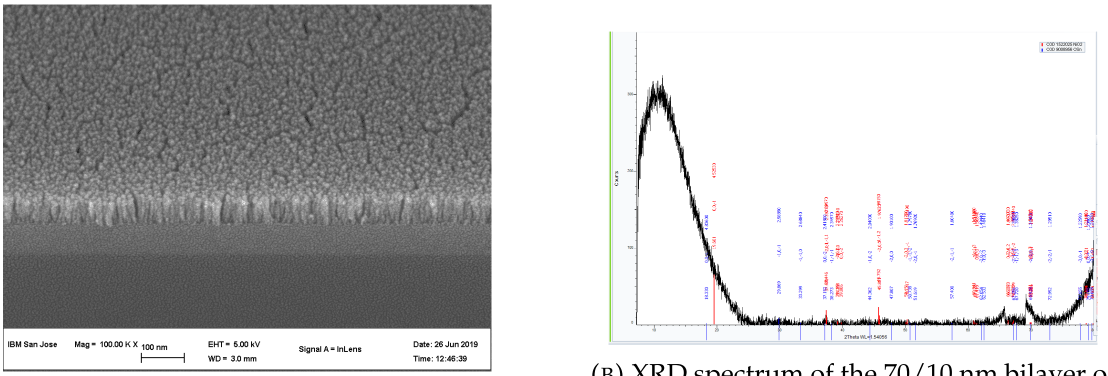

(A) SEM image of the 70/10 nm bilayer of respectively SnO_2/NiO deposited in DC and annealed in RTA for 30 min at 400°C.

(B) XRD spectrum of the 70/10 nm bilayer of respectively SnO_2/NiO deposited in DC and annealed in RTA for 30 min at 400°C.

FIGURE 6.4

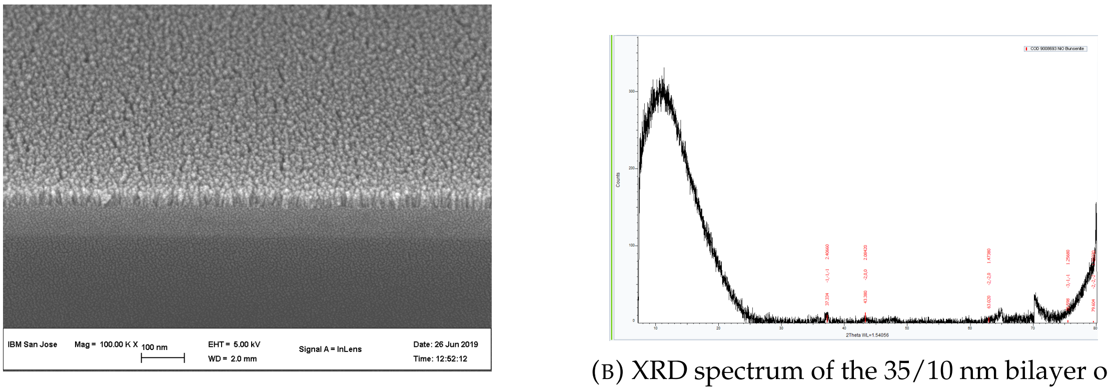

(A) SEM image of the 35/10 nm bilayer of respectively SnO_2/NiO deposited in DC and annealed in RTA for 30 min at 400°C.

(B) XRD spectrum of the 35/10 nm bilayer of respectively SnO_2/NiO deposited in DC and annealed in RTA for 30 min at 400°C.

FIGURE 6.5

600°C

Compared to the 6.2.2 case more consistent XRD peaks appear (figures 6.6b, 6.7b and 6.8b), in particular clear peaks of SnO_2 crystallinity start to be evident for the bilayers, which shows a preferential crystal growth in the (-1,0,-1) plane. As expected the thicker bilayer (70/10 nm) give a stronger signal than the thinner one (35/10 nm). Nickel-oxide crystallinity is found even in this case with peaks more consistent than in the 400°C case. Comparing the SEM images (6.6a, 6.7a and 6.8a) of the film with the 6.2.2 ones the cracks are definitely more evident, probably because of the more harsh annealing treatment compared to the previous one. For RF-90 a higher crystallinity compared to the 6.2.2 case is found with a peaks intensity which doubles.

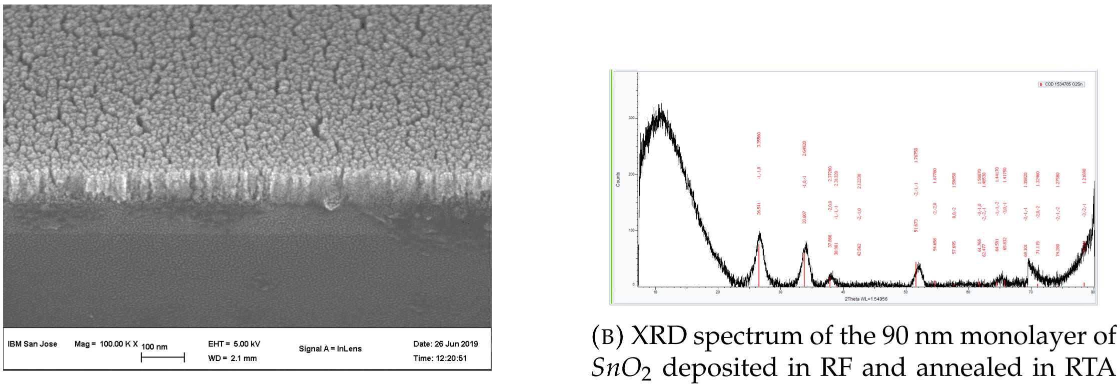

(A) SEM image of the 90 nm monolayer of SnO_2 deposited in RF and annealed in RTA for 30 min at 600°C.

(B) XRD spectrum of the 90 nm monolayer of SnO_2 deposited in RF and annealed in RTA for 30 min at 600°C.

FIGURE 6.6

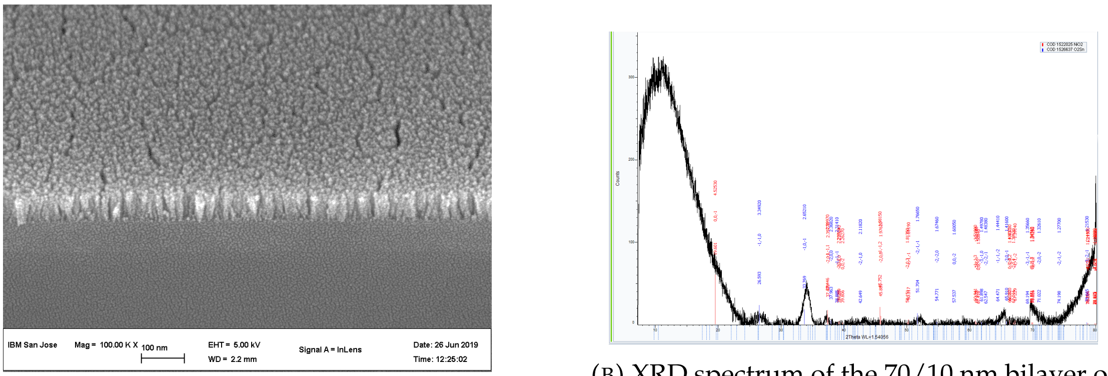

(A) SEM image of the 70/10 nm bilayer of respectively SnO_2/NiO deposited in DC and annealed in RTA for 30 min at 600°C.

(B) XRD spectrum of the 70/10 nm bilayer of respectively SnO_2/NiO deposited in DC and annealed in RTA for 30 min at 600°C.

FIGURE 6.7

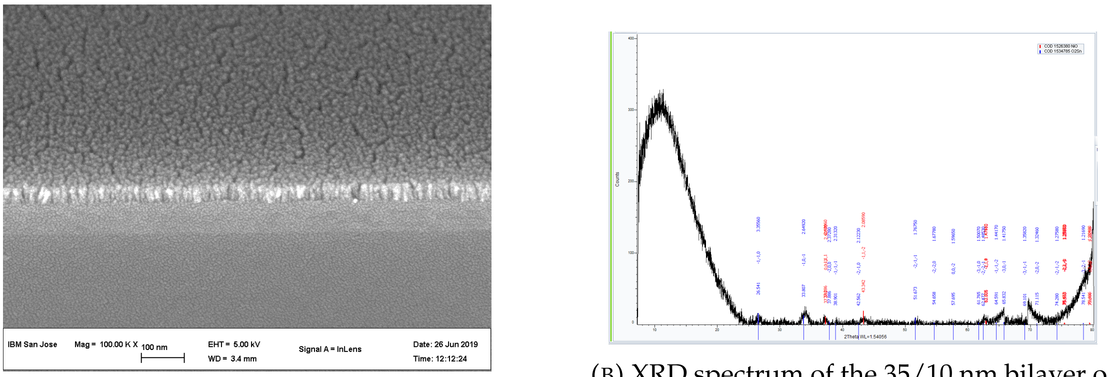

(A) SEM image of the 35/10 nm bilayer of respectively SnO_2/NiO deposited in DC and annealed in RTA for 30 min at 600°C.

(B) XRD spectrum of the 35/10 nm bilayer of respectively SnO_2/NiO deposited in DC and annealed in RTA for 30 min at 600°C.

FIGURE 6.8

6.2.3 Hot Plate annealing

16h

For what concern 90-RF (figure 6.9b) a crystallinity similar to the RTA 600°C case is evident. While in 35/10-DC no crystallinity is present (except for some NiO low intensity peaks detected by the XRD pattern recognition tool as shown in figure 6.11b), for 70/10-DC some SnO_2 crystallinity is evident. It is still interesting to see that as in the RTA 600°C case and for 70/10-DC only, the Tin-oxide has a preferential crystal growth in the (-1,0,-1) plane. Cracks are visible only from the SEM images (figure 6.9a and 6.10a) of the 90-RF and 70/10-DC samples where however are less pronunced than the ones derived from the RTA 600°C annealing.

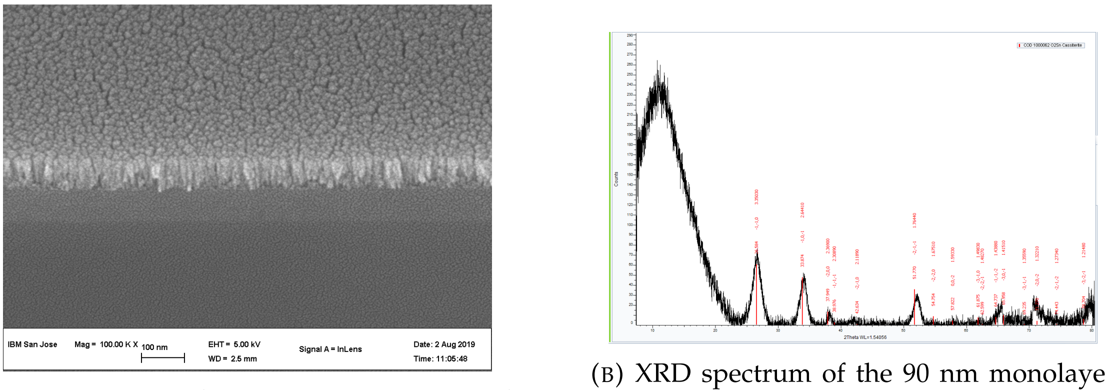

(A) SEM image of the 90 nm monolayer of SnO_2 deposited in RF and annealed on the hot plate at 400°C for 16 hours.

(B) XRD spectrum of the 90 nm monolayer of SnO_2 deposited in RF and annealed on the hot plate at 400°C for 16 hours.

FIGURE 6.9

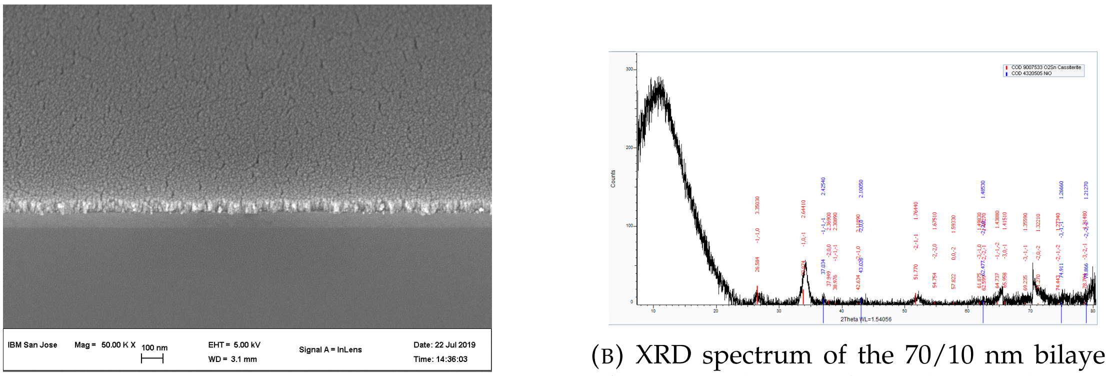

(A) SEM image of the 70/10 nm bilayer of respectively SnO_2/NiO deposited in DC and annealed on the hot plate at 400°C for 16 hours.

(B) XRD spectrum of the 70/10 nm bilayer of respectively SnO_2/NiO deposited in DC and annealed on the hot plate at 400°C for 16 hours.

FIGURE 6.10

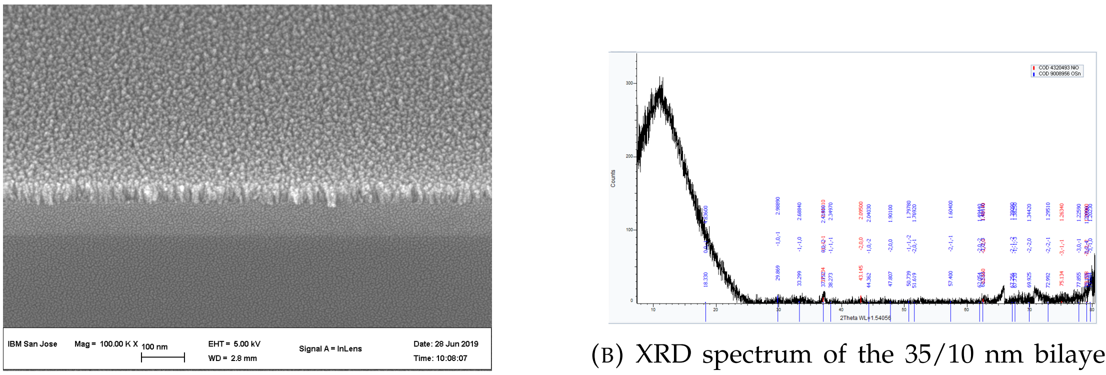

(A) SEM image of the 35/10 nm bilayer of respectively SnO_2/NiO deposited in DC and annealed on the hot plate at 400°C for 16 hours.

(B) XRD spectrum of the 35/10 nm bilayer of respectively SnO_2/NiO deposited in DC and annealed on the hot plate at 400°C for 16 hours.

FIGURE 6.11

24h

For a 24 hours annealing the XRD results are similar to the ones of the 16 hours annealing for both the RF deposited single layer and the DC deposited bilayers (figures 6.12b, 6.13b and 6.14b). Peaks intensities are almost unchanged with the case before, as well as the grain size. For what concern the films cracking (figure 6.12a, 6.13a, 6.14a) no cracks are present in 35/10-DC, while the other films show more cracks than then RTA 600°C case.

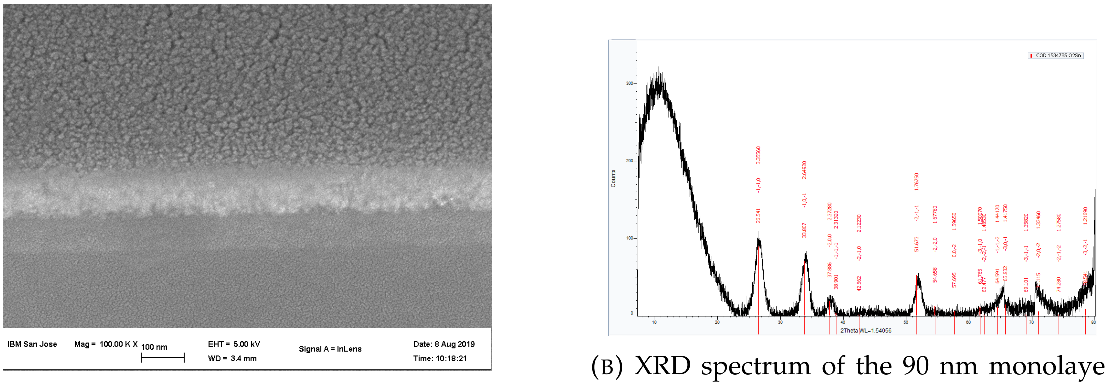

(A) SEM image of the 90 nm monolayer of SnO_2 deposited in RF and annealed on the hot plate at 400°C for 24 hours.

(B) XRD spectrum of the 90 nm monolayer of SnO_2 deposited in RF and annealed on the hot plate at 400°C for 24 hours.

FIGURE 6.12

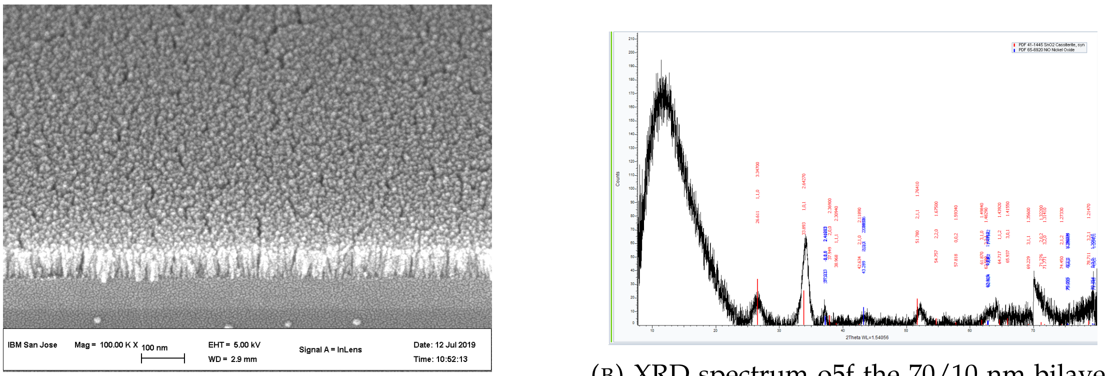

(A) SEM image of the 70/10 nm bilayer of respectively SnO_2/NiO deposited in DC and annealed on the hot plate at 400°C for 24 hours.

(B) XRD spectrum o5f the 70/10 nm bilayer of respectively SnO_2/NiO deposited in DC and annealed on the hot plate at 400°C for 24 hours.

FIGURE 6.13

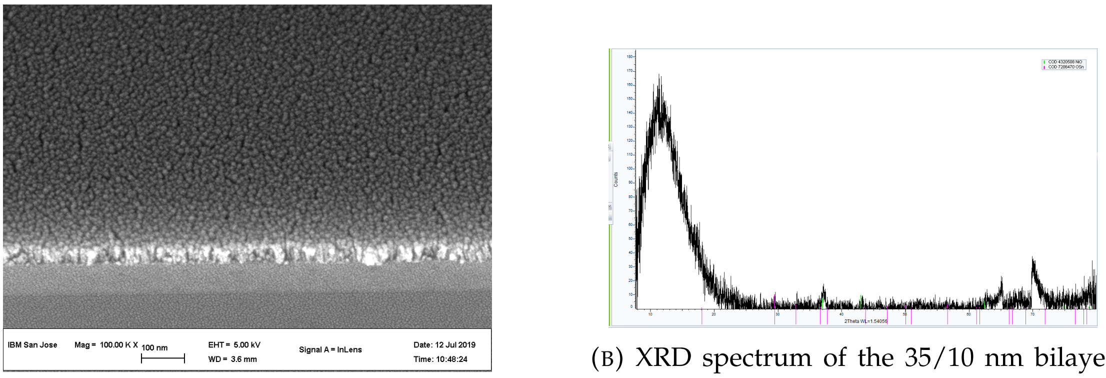

(A) SEM image of the 35/10 nm bilayer of respectively SnO_2/NiO deposited in DC and annealed on the hot plate at 400°C for 24 hours.

(B) XRD spectrum of the 35/10 nm bilayer of respectively SnO_2/NiO deposited in DC and annealed on the hot plate at 400°C for 24 hours.

FIGURE 6.14

48h

Still for a 48 hours annealing the XRD results are similar to the previous cases (16 hours and 24 hours), for both the RF deposited single layer and the DC deposited bilayers (figures 6.12b, 6.13b and 6.14b). Peaks intensities are almost unchanged with the case before, as well as the grain size. Still here as in the previous case no SnO_2 can be detected from the 35/10-DC sample where however the XRD pattern recognition tool detects a light presence of NiO.

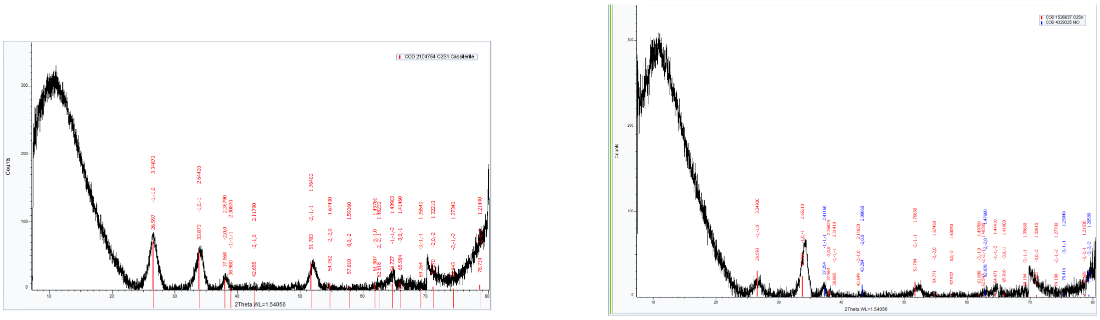

(A) XRD spectrum of the 90 nm monolayer of SnO_2 deposited in RF and annealed on the hot plate at 400°C for 48 hours.

(B) XRD spectrum of the 70-10 nm bilayer of respectively SnO_2/NiO deposited in DC and annealed on the hot plate at 400°C for 48 hours.

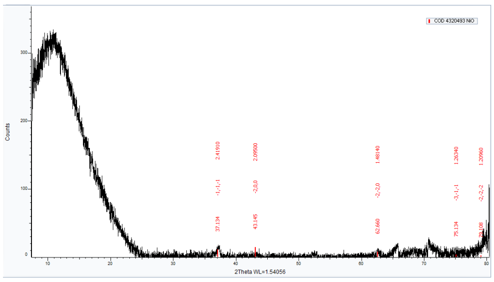

(C) XRD spectrum of the 35-10 nm bilayer of respectively SnO_2/NiO deposited in DC and annealed on the hot plate at 400°C for 48 hours.

FIGURE 6.15

6.2.4 Oven annealing

400°C

Good evidence of crystallinity is shown (figure 6.16a) for the 90nm-RF deposited sample, comparable to the one of the RTA 600°C and Hot-plate annealing. Almost no peaks are present in the bilayers (figure 6.16b and 6.16c) where the XRD pattern recognition tool find however some presence of NiO.

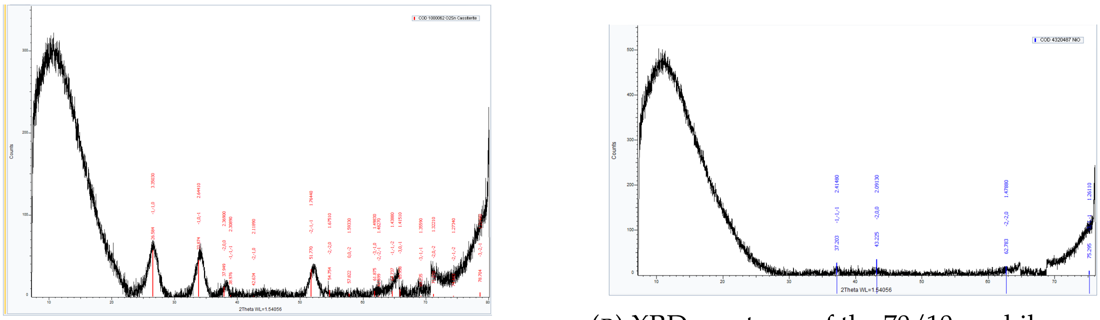

(A) XRD spectrum of the 90 nm monolayer of SnO_2 deposited in RF and annealed in the oven at 400°C for 16 hours.

(B) XRD spectrum of the 70/10 nm bilayer of respectively SnO_2/NiO deposited in DC and annealed in the oven at 400°C for 16 hours.

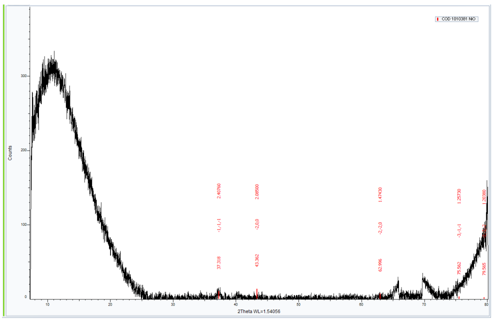

(C) XRD spectrum of the 35/10 nm bilayer of respectively SnO_2/NiO deposited in DC and annealed in the oven at 400°C for 16 hours.

FIGURE 6.16

600°C

The presence of crystallinity is determined for all the layers. For the 90 nm RF film the intensity of the peaks increase 3 times (figure 6.17b). Consistent presence of SnO_2 is evident in all the bilayers, with NiO peaks intensity which are more consistent than in the other annealing cases. For both the bilayers Tin-oxide show the same (-1,0,-1) preferential plane for the crystal growth. As figure 6.10a shows, cracks on the 70/10-DC film are present, interesting is the morphology obtained in the 90 nm RF single layer after this annealing, as you can see in figure 6.17a the columnar-like structure present in all the samples so far, turned into a more granular one.

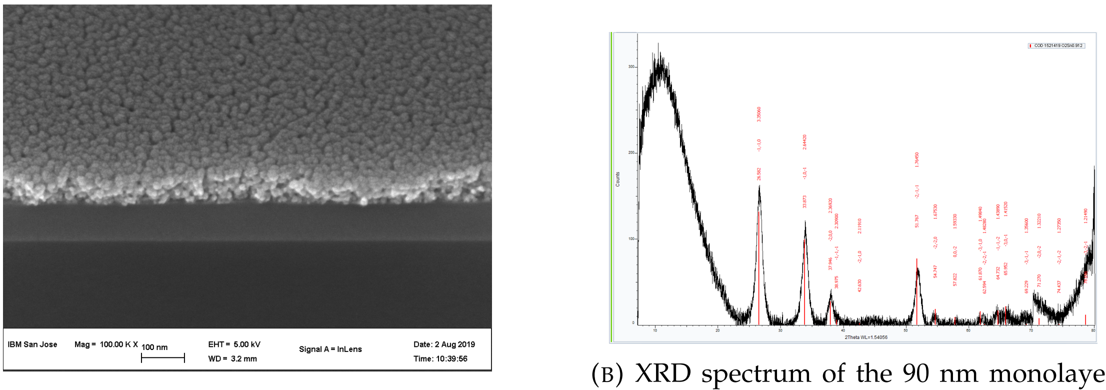

(A) SEM image of the 90 nm monolayer of SnO_2 deposited in RF and annealed in the oven at 600°C for 16 hours.

(B) XRD spectrum of the 90 nm monolayer of SnO_2 deposited in RF and annealed in the oven at 600°C for 16 hours.

FIGURE 6.17

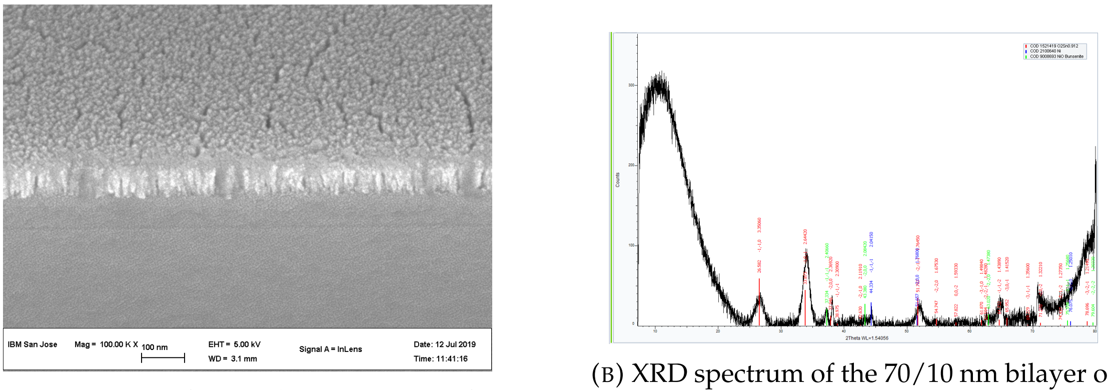

(A) SEM image of the 70/10 nm bilayer of respectively SnO_2/NiO deposited in DC and annealed in the oven at 600°C for 16 hours.

(B) XRD spectrum of the 70/10 nm bilayer of respectively SnO_2/NiO deposited in DC and annealed in the oven at 600°C for 16 hours.

FIGURE 6.18

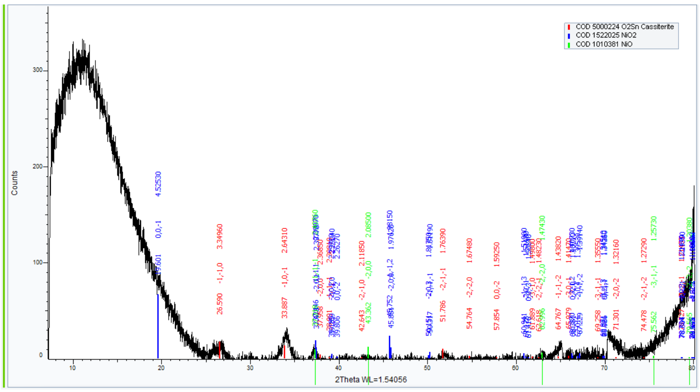

FIGURE 6.19: XRD spectrum of the 35/10 nm bilayer of respectively SnO_2/NiO deposited in DC and annealed in the oven at 600°C for 16 hours.

TEM

To have a better insight of the Nickel-oxide/Tin-oxide interface, TEM measurements were performed on the as-deposited and Hot plate 400°C 24 hours annealed sample 70/10 nm thick DC deposited. Due to time constraints, it was not possible to perform a similar analysis of the other differently annealed samples. In figure 6.20a and 6.20b you can see the TEM of the 70/10-DC film respectively before and after the 24 hours 400°C annealing treatment. In the as-deposited sample EELS shows no intermixing between the two oxides, while TEM image shows a uniform and proper contact between the two layers, with the most likely presence of a p-n junction where the depletion regions are created. As in the previous experiment (Chapter 5) the deposited NiO thickness is found to be 10/15 nm higher than the nominal one because of the not constant deposition rate. Comparing the two images a clear detachment between the NiO and SnO_2 is present after the annealing, this result is similar to the one of Chapter 5 where the RTA treatment was found to have the same but less pronounced effect on the bilayer. As already hypothesized the two materials have a low intersolubility, correspondingly Nickel-oxide de-wet from Tin-oxide upon heat treatment.

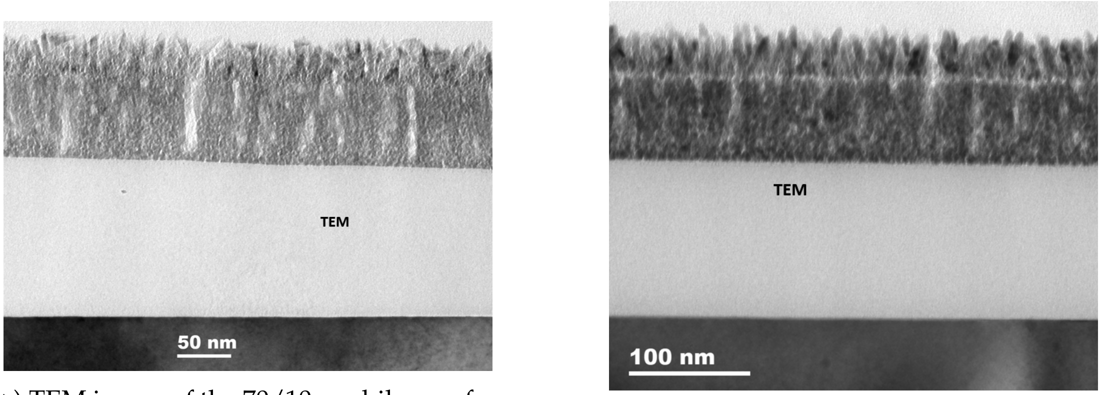

(A) TEM image of the 70/10 nm bilayer of respectively SnO_2/NiO deposited in DC, not further annealing has been applied to this layer.

(B) TEM image of the 70/10 nm bilayer of respectively SnO_2/NiO deposited in DC and annealed on the hot plate at 400°C for 24 hours.

FIGURE 6.20

Looking at the Z-contrast images shown in figure 6.21a and 6.21b, the treatment seems to increase the crystallinity, this was somewhat expected and clear already by the XRD analysis which on the contrary does not show the crystallinity already present in the film as deposited. For what concern the cracks question, evidences of film cracking enhancement were visible already from the SEM images, unfortunately this is not evident in the TEM images which show cracks already in the deposited unannaealed film.

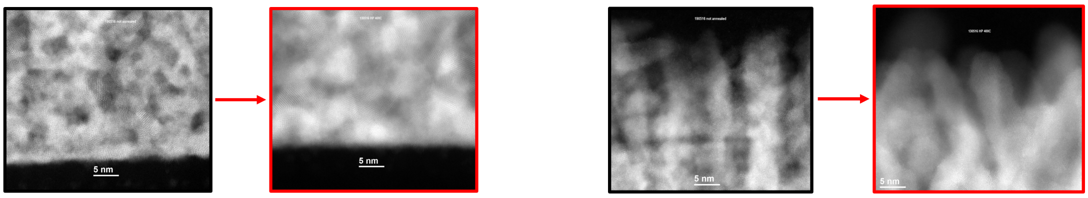

(A) Z-contrast TEM image of the SnO_2 of the SnO_2/NiO bilayer as deposited and after the 24 hours at 400°C annealing treatment.

(B) Z-contrast TEM image of the NiO of the SnO_2/NiO bilayer as deposited and after the 24 hours at 400°C annealing treatment..

FIGURE 6.21

6.3 Conclusions

In this chapter was described the investigation of the morphological and crystallographic impact of several annealing techniques on the three different sensing layers (sputtered), with the aim to find an optimal design solution. The three sensing films selected were a 90 nm RF deposited SnO_2 single layer film, a 70/10 nm SnO_2/NiO DC deposited bilayer and a 35/10 nm SnO_2/NiO DC deposited bilayer. The annealing processes selected were: Rapid Thermal Annealing (RTA) at 400°C and 600°C for 30 min in N_2 and synthetic air (80% N_2, 20% O_2) atmosphere, oven annealing at 400 and 600°C for 16 hours and finally hot-plate annealing at 400°C for 16, 24 and 48 hours. In addition, for each of the deposited film, a single sample was preserved to any treatment to be used as a reference. To characterize the results SEM, XRD and TEM were used.

Results show interesting differences between the annealing treatments and the films. It appears that either if the film is deposited in RF or in DC, no crystallinity is detected from the XRD without annealing, moreover the morphology is columnar-like as in the case shown in Chapter 5. Differences arise instead with annealing treatments, in particular while the RF does not show any preferential crystal growth, the DC bilayer preferential plane in this sense is the (-1,0,-1) . As expected for all the treatments the two DC SnO_2/NiO bilayers (35/10 nm and 70/10 nm) have the same crystallographic pattern with a higher relative intensity for the thicker film. For all the annealing treatments the 90 nm RF film shows crystallinity, higher for the higher temperature treatments (RTA 600°C, Oven annealing 600°C). In particular a morphological change from columnar-like structure to granular like follows the 600°C oven annealing. This represent a film-annealing combination which considering the high porosity of the result, is worthy to be investigated. Another interesting result is that for this film the hot-plate treatment, independently from time (16, 24 and 48 hours) seems to produce the same results: this might be the proof of the stability of the film from reconstruction. For this film as for the bilayers, RTA treatments in the two atmospheres (N_2 and synthetic air) show to be equivalent. For what concern the bilayer, XRD shows crystallization of the SnO_2 for RTA 600°C, Oven annealing 600°C and for Hot plate annealing. Again (as for the 90 nm RF film) the latter gives the same results for 16, 24 and 48 hours treatments and the best crystallinity for the less presence of cracks in the film. For the previous reasons Hot Plate annealing represents an interesting treatment to be investigated and eventually to use in design. Consistent diffraction peaks of Nickel-oxide are present in the RTA 600°C, Oven 600°C and in all the Hot-plate treatments, it is worth to mention that doubtful peaks of the same material are found from the XRD pattern recognition tool in all the other treatments. A further analysis on this crystallization would be possible depositing a thicker film. A fundamental result comes from the TEM analysis of the 70/10 nm sample as deposited and annealed on the hot-plate for 24 hours, indeed after the results of Chapter 5, this shows that annealing generate de-wetting of the Nickel-oxide layer from the Tin-oxide layer avoiding the formation of any junction between the two. TEM further shows that a slight crystallinity is already present before the hot-plate annealing, while EELS shows that the oxides are since the deposition not intermixed.

In general, these results, give interesting hints on the further directions to be investigated.

Hot-plate annealing represents a treatment with interesting properties if it is considered the low morphological change (less if cracks are considered), it would be interesting to explore the stability generated on this treatment in SnO_2/NiO bilayers and eventually RF deposited films. A future exploratory experiment is the application of this treatment on a systematic thickness analysis, as in the case shown in Chapter 5.

RF deposition shows interesting properties and represents a further degree of freedom in design, especially from the crystallographic point view. It would be interesting in this sense to compare two equally thick bilayers fabricated in DC and RF (sputtering), as it would to add in this investigation the hot-plate at 400°C and oven annealing at 600°C treatment.

For the characterization, it would also be interesting to extend the TEM analysis made for the Hot-plate annealing to the other annealing treatments (except RTA 600°C already made in Chapter 5).

Chapter 7

Conclusions

During these 6 months of activity with the Sensor Group at the IBM ARC, Metal Oxide gas sensors were fabricated, characterized and tested. In particular, the project was focused on the investigation of SnO_2/NiO bilayer metal-oxide-semiconductor gas sensors deposited by a relatively cheap and easy deposition technique such as sputtering. In this frame, two important experiments have been carried out: a thickness systematic analysis and an annealing systematic analysis of the bilayers.

Concerning the thickness systematics, the idea was to see how modulating the thickness of one of the two layers (while keeping the other constant) would influence the response and characteristics of the devices were influenced. In addition it was investigated the influence of the Rapid Thermal Annealing (RTA) treatment on these devices at 600°C for 30 min in N_2 and synthetic air (80% N_2, 20% O_2) atmosphere. A first set of devices was fabricated (in a cleanroom environment) with bilayers of 70 nm thick SnO_2 and a respective NiO thickness of 0, 5, 10, 15 and 20 nm. A second set of devices was fabricate with bilayers of 35 nm thick SnO_2 and a respective NiO thickness of 0, 5, 10 and 20 nm. In addition to the 70/20 nm and 35/20 nm thick SnO_2/NiO bilayers were fabricated a 20/20 nm and a 200/20 nm thick one, this, to complete a third set of devices with bilayers of fixed NiO thickness and variable SnO_2 one. Devices were then tested on a gas sensing setup and characterized with conventional characterization techniques (SEM, TEM, XPS). In general, considering even the "exploratory" nature of the experiment, good results were obtained. What this study showed was that adding a NiO layer of specific thickness on top of 70 nm and 35 nm thick SnO_2 it is possible to enhance up to 5 times its sensitivity. According to this a SnO_2 depletion model was derived which, however it did not agree with the set of devices with 20 nm thick NiO. For what concern the RTA treatment this seemed to increase the baseline resistance of the devices and make the NiO enhancement effects totally disappear. Following this experiment a fundamental aspect to address is the reproducibility of the fabrication, indeed while the results obtained showed a quite clear trends dispersion was present in most of them. For this reason a more controllable and reproducible fabrication process would be necessary for next experiments, to improve the relevance of the results. Nevertheless, since a response enhancement was effectively shown in some conditions, a further investigation working again around the 35 and 70 nm thickness for SnO_2 will be necessary. More specifically, it would be necessary to demonstrate the validity of the formulated SnO_2 depletion model or eventually build a new one capable to explain the response enhancement shown. Despite the results for RTA were not optimal, the prospectives of this techniques can again be investigated by testing the stability of the already tested (annealed) devices. Eventually if a good stability is demonstrated, the same study for a 400°C treatment can be repeated.

For what concern the annealing systematics, the idea was to see how with the different annealing techniques impact morphology and crystallinity of the three different (sputterimg) sensing layers. The three sensing films selected were a 90 nm RF deposited SnO_2 single layer film, a 70/10 nm SnO_2/NiO DC deposited bilayer and a 35/10 nm SnO_2/NiO DC deposited bilayer. The annealing processes selected were: Rapid Thermal Annealing (RTA) at 400°C and 600°C for 30 min in N_2 and synthetic air (80% N_2, 20% O_2) atmosphere, oven annealing at 400 and 600°C for 24 hours and finally hot-plate annealing at 400°C for 16, 24 and 48 hours. In addition, for each of the deposited film a single sample was preserved to any treatment to be used as a reference. To characterize the results, conventional characterization techniques (SEM, TEM, XPS) were used. In general, good results were obtained giving some hints on design solutions. In particular the experiment showed that while the RF and the DC deposited films show a similar morphology, the first crystallize more easily than the second, which at the same time shows a preferential crystal growth in the (-1,0,-1) plane. A fundamental result was that all the annealing treatments create cracks in the film. Interesting results were then obtained from the Hot-plate annealing of all the films, indeed the same crystallinity was obtained independently if the treatment was for 16, 24 or 48 hours, as proof of possible stability of the device from reconstruction. For this reason hot-plate represents a interesting technique which will sure be added to a thickness systematic experiment as the one shown in Chapter 5. Considering also the relevant results from the crystallography point of view shown by the RF films, an interesting analysis would be to deposit two nominally equal SnO_2/NiO bilayers (same thicknesses of the ones in Chapter 5) but deposited one in DC and the other in RF to test their performances. In addition testing on these bilayers even the effect of hot-plate annealing treatment at 400°C and oven annealing treatment at 600°C.

In conclusion, this 6 months activity with the Sensor Group has brought a large number of interesting results (sometimes more sometimes less), which brought the group a step forwards in the Gas Sensor Project. All that, considering a project which, from the first moment, has shown interesting challenges which can be certainly overcome with the expertise of the Sensor Group leading to the final development of an electronic nose.

Appendix A

Images

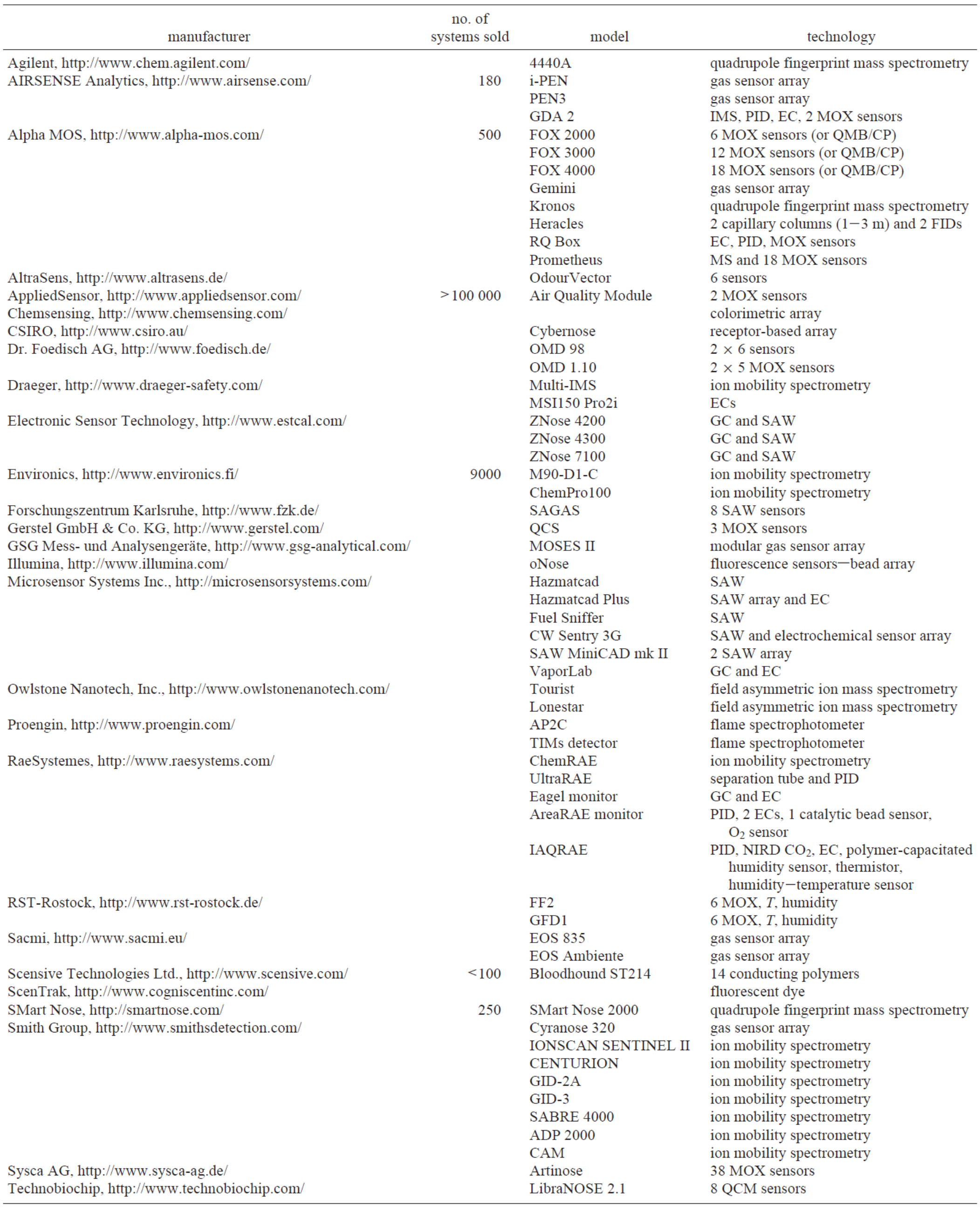

manufacturer	no. of systems sold	model	technology
Agilent, http://www.chem.agilent.com/		4440A	quadrupole fingerprint mass spectrometry
AIRSENSE Analytics, http://www.airsense.com/	180	i-PEN	gas sensor array
		PEN3	gas sensor array
		GDA 2	IMS, PID, EC, 2 MOX sensors
Alpha MOS, http://www.alpha-mos.com/	500	FOX 2000	6 MOX sensors (or QMB/CP)
		FOX 3000	12 MOX sensors (or QMB/CP)
		FOX 4000	18 MOX sensors (or QMB/CP)
		Gemini	gas sensor array
		Kronos	quadrupole fingerprint mass spectrometry
		Heracles	2 capillary columns (1−3 m) and 2 FIDs
		RQ Box	EC, PID, MOX sensors
		Prometheus	MS and 18 MOX sensors
AltraSens, http://www.altrasens.de/		OdourVector	6 sensors
AppliedSensor, http://www.appliedsensor.com/	>100 000	Air Quality Module	2 MOX sensors
Chemsensing, http://www.chemsensing.com/			colorimetric array
CSIRO, http://www.csiro.au/		Cybernose	receptor-based array
Dr. Foedisch AG, http://www.foedisch.de/		OMD 98	2 × 6 sensors
		OMD 1.10	2 × 5 MOX sensors
Draeger, http://www.draeger-safety.com/		Multi-IMS	ion mobility spectrometry
		MSI150 Pro2i	ECs
Electronic Sensor Technology, http://www.estcal.com/		ZNose 4200	GC and SAW
		ZNose 4300	GC and SAW
		ZNose 7100	GC and SAW
Environics, http://www.environics.fi/	9000	M90-D1-C	ion mobility spectrometry
		ChemPro100	ion mobility spectrometry
Forschungszentrum Karlsruhe, http://www.fzk.de/		SAGAS	8 SAW sensors
Gerstel GmbH & Co. KG, http://www.gerstel.com/		QCS	3 MOX sensors
GSG Mess- und Analysengeräte, http://www.gsg-analytical.com/		MOSES II	modular gas sensor array
Illumina, http://www.illumina.com/		oNose	fluorescence sensors−bead array
Microsensor Systems Inc., http://microsensorsystems.com/		Hazmatcad	SAW
		Hazmatcad Plus	SAW array and EC
		Fuel Sniffer	SAW
		CW Sentry 3G	SAW and electrochemical sensor array
		SAW MiniCAD mk II	2 SAW array
		VaporLab	GC and EC
Owlstone Nanotech, Inc., http://www.owlstonenanotech.com/		Tourist	field asymmetric ion mass spectrometry
		Lonestar	field asymmetric ion mass spectrometry
Proengin, http://www.proengin.com/		AP2C	flame spectrophotometer
		TIMs detector	flame spectrophotometer
RaeSystemes, http://www.raesystems.com/		ChemRAE	ion mobility spectrometry
		UltraRAE	separation tube and PID
		Eagel monitor	GC and EC
		AreaRAE monitor	PID, 2 ECs, 1 catalytic bead sensor, O_2 sensor
		IAQRAE	PID, NIRD CO_2, EC, polymer-capacitated humidity sensor, thermistor, humidity−temperature sensor
RST-Rostock, http://www.rst-rostock.de/		FF2	6 MOX, *T*, humidity
		GFD1	6 MOX, *T*, humidity
Sacmi, http://www.sacmi.eu/		EOS 835	gas sensor array
		EOS Ambiente	gas sensor array
Scensive Technologies Ltd., http://www.scensive.com/	<100	Bloodhound ST214	14 conducting polymers
ScenTrak, http://www.cogniscentinc.com/			fluorescent dye
SMart Nose, http://smartnose.com/	250	SMart Nose 2000	quadrupole fingerprint mass spectrometry
Smith Group, http://www.smithsdetection.com/		Cyranose 320	gas sensor array
		IONSCAN SENTINEL II	ion mobility spectrometry
		CENTURION	ion mobility spectrometry
		GID-2A	ion mobility spectrometry
		GID-3	ion mobility spectrometry
		SABRE 4000	ion mobility spectrometry
		ADP 2000	ion mobility spectrometry
		CAM	ion mobility spectrometry
Sysca AG, http://www.sysca-ag.de/		Artinose	38 MOX sensors
Technobiochip, http://www.technobiochip.com/		LibraNOSE 2.1	8 QCM sensors

FIGURE A.1: Commercially available electronic noses. Adapted from Rock et al., 2008.

Bibliography

Albert, Keith J. et al. (2000). “Cross-Reactive Chemical Sensor Arrays”. In: *Chemical Reviews* 100.7. PMID: 11749297, pp. 2595–2626. DOI: 10.1021/cr980102w. eprint: https://doi.org/10.1021/cr980102w. URL: https://doi.org/10.1021/cr980102w.

Arshak, K. et al. (June 2004). “A Review of Gas Sensors Employed in Electronic Nose Applications”. In: *Sensor Review* 24, pp. 181–198. DOI: 10.1108/02602280410525977.

Barsan, Nicolae and Udo Weimar (2001). “Conduction Model of Metal Oxide Gas Sensors”. In: *Journal of Electroceramics* 7, pp. 143–167.

Brattain, Walter H. and John Bardeen (1953). “Surface Properties of Germanium”. In: *Bell System Technical Journal* 32.1, pp. 1–41. DOI: 10.1002/j.1538-7305.1953.tb01420.x. eprint: https://onlinelibrary.wiley.com/doi/pdf/10.1002/j.1538-7305.1953.tb01420.x. URL: https://onlinelibrary.wiley.com/doi/abs/10.1002/j.1538-7305.1953.tb01420.x.

Brinke, J. Ten et al. (1998). “Development of New Volatile Organic Compound (VOC) Exposure Metrics and their Relationship to “Sick Building Syndrome” Symptoms”. In: *Indoor Air* 8.3, pp. 140–152. DOI: 10.1111/j.1600-0668.1998.t01-1-00002.x. eprint: https://onlinelibrary.wiley.com/doi/pdf/10.1111/j.1600-0668.1998.t01-1-00002.x. URL: https://onlinelibrary.wiley.com/doi/abs/10.1111/j.1600-0668.1998.t01-1-00002.x.

Burge, P. S. (Feb. 2004). “Sick building syndrome”. In: *Occupational and environmental medicine* 61.2. 14739390[pmid], pp. 185–190. ISSN: 1470-7926. DOI: 10.1136/oem.2003.008813. URL: https://www.ncbi.nlm.nih.gov/pubmed/14739390.

Carey, W. Patrick. and Bruce R. Kowalski (1986). “Chemical piezoelectric sensor and sensor array characterization”. In: *Analytical Chemistry* 58.14, pp. 3077–3084. DOI: 10.1021/ac00127a037. eprint: https://doi.org/10.1021/ac00127a037. URL: https://doi.org/10.1021/ac00127a037.

Chen, J. et al. (2005). “Alpha-Fe2O3 Nanotubes in Gas Sensor and Lithium-Ion Battery Applications”. In: *Advanced Materials* 17.5, pp. 582–586. DOI: 10.1002/adma.200401101. eprint: https://onlinelibrary.wiley.com/doi/pdf/10.1002/adma.200401101. URL: https://onlinelibrary.wiley.com/doi/abs/10.1002/adma.200401101.

Cocina, Isabella, Matteo Falasconi, and Veronica Sberveglieri (Nov. 2012). “Electronic Noses as Flexible Tools to Assess Food Quality and Safety: Should We Trust Them?” In: *IEEE Sensors Journal* 12.11, pp. 3232–3237. DOI: 10.1109/JSEN.2012.2195306.

Comini, E. et al. (2002). “Stable and highly sensitive gas sensors based on semiconducting oxide nanobelts”. In: *Applied Physics Letters* 81.10, pp. 1869–1871. DOI: 10.1063/1.1504867. eprint: https://doi.org/10.1063/1.1504867. URL: https://doi.org/10.1063/1.1504867.

Comini, Elisabetta (2006). “Metal oxide nano-crystals for gas sensing”. In: *Analytica Chimica Acta* 568.1. Molecular Electronics and Analytical Chemistry, pp. 28 –40. ISSN: 0003-2670. DOI: https://doi.org/10.1016/j.aca.2005.10.069. URL: http://www.sciencedirect.com/science/article/pii/S0003267005018283.

Creaser, Colin S. et al. (2004). "Ion mobility spectrometry: a review. Part 1. Structural analysis by mobility measurement". In: *Analyst* 129 (11), pp. 984–994. DOI: `10.1039/B404531A`. URL: `http://dx.doi.org/10.1039/B404531A`.

Dainty, R.H. (1996). "Chemical/biochemical detection of spoilage". In: *International Journal of Food Microbiology* 33.1. Specific Spoilage Organisms, pp. 19 –33. ISSN: 0168-1605. DOI: `https://doi.org/10.1016/0168-1605(96)01137-3`. URL: `http://www.sciencedirect.com/science/article/pii/0168160596011373`.

Datta, Niyanta et al. (2012). "Selective H2S sensing characteristics of hydrothermally grown ZnO-nanowires network tailored by ultrathin CuO layers". In: *Sensors and Actuators B: Chemical* 166-167, pp. 394 –401. ISSN: 0925-4005. DOI: `https://doi.org/10.1016/j.snb.2012.02.079`. URL: `http://www.sciencedirect.com/science/article/pii/S0925400512002304`.

Devi, G. Sarala, S. Manorama, and V.J. Rao (1995). "Gas Sensitivity of SnO2/CuO Heterocontacts". In: *Journal of the Electrochemical Society* 142.8, pp. 2754–2757. DOI: `10.1149/1.2050087`.

Devi, G.Sarala et al. (2002). "Synthesis of mesoporous TiO2-based powders and their gas-sensing properties". In: *Sensors and Actuators B: Chemical* 87.1, pp. 122 –129. ISSN: 0925-4005. DOI: `https://doi.org/10.1016/S0925-4005(02)00228-9`. URL: `http://www.sciencedirect.com/science/article/pii/S0925400502002289`.

European Parliament, Council of the European Union: Directive 2008/50/EC of the European Parliament and of the Council of 21 May 2008 on Ambient Air Quality and Cleaner Air for Europe. Accessed: 2019-09-18. URL: `http://eur-lex.europa.eu/legal-content/EN/TXT/?uri=celex%3A32008L0050`.

Fasoli, Andrea. *Sputtering of metal oxide semiconductor n-p stacks*. Presented at ISOEN 2019 Fukoka (Japan) on May 29th 2019.

Fraden, J. (1996). *AIP Handbook of Modern Sensors*. New York, USA: AIP, New York.

Ghosh, Manoranjan and A K Raychaudhuri (Sept. 2008). "Shape transition in ZnO nanostructures and its effect on blue-green photoluminescence". In: *Nanotechnology* 19.44, p. 445704. DOI: `10.1088/0957-4484/19/44/445704`. URL: `https://doi.org/10.1088%2F0957-4484%2F19%2F44%2F445704`.

Goschnick, J. and M. Harms (2002). "Landmine Detection with an Electronic Nose Mounted on an Airship". In: *Detection of Explosives and Landmines: Methods and Field Experience*. Ed. by Hiltmar Schubert and Andrey Kuznetsov. Dordrecht: Springer Netherlands, pp. 83–91. ISBN: 978-94-010-0397-1. DOI: `10.1007/978-94-010-0397-1_9`. URL: `https://doi.org/10.1007/978-94-010-0397-1_9`.

Göpel, Wolfgang and Klaus Dieter Schierbaum (1995). "SnO2 sensors: current status and future prospects". In: *Sensors and Actuators B: Chemical* 26.1, pp. 1 –12. ISSN: 0925-4005. DOI: `https://doi.org/10.1016/0925-4005(94)01546-T`. URL: `http://www.sciencedirect.com/science/article/pii/092540059401546T`.

Gurlo, Alexander (2006). "Interplay between O2 and SnO2: Oxygen Ionosorption and Spectroscopic Evidence for Adsorbed Oxygen". In: *ChemPhysChem* 7.10, pp. 2041–2052. DOI: `10.1002/cphc.200600292`. eprint: `https://onlinelibrary.wiley.com/doi/pdf/10.1002/cphc.200600292`. URL: `https://onlinelibrary.wiley.com/doi/abs/10.1002/cphc.200600292`.

Hübner, M. et al. (2011). "Influence of humidity on CO sensing with p-type CuO thick film gas sensors". In: *Sensors and Actuators B: Chemical* 153.2, pp. 347 –353. ISSN: 0925-4005. DOI: `https://doi.org/10.1016/j.snb.2010.10.046`. URL: `http://www.sciencedirect.com/science/article/pii/S0925400510008646`.

Heiland, G. and D. Kohl (1988). *Chemical Sensor Technology, Vol. 1*. Ed. by T. Seiyama. Kodansha, Tokyo. Chap. 2, pp. 15–38.

Henrich, V.A. and P.A. Cox (1994). *The Surface Science of Metal Oxides*. Ed. by Cambridge University Press, 312–316.

Hwang, In-Sung et al. (2009). “Enhanced H2S sensing characteristics of SnO2 nanowires functionalized with CuO”. In: *Sensors and Actuators B: Chemical* 142.1, pp. 105 – 110. ISSN: 0925-4005. DOI: https://doi.org/10.1016/j.snb.2009.07.052. URL: http://www.sciencedirect.com/science/article/pii/S0925400509006145.

Ionescu, R. et al. (2003). “Response model for thermally modulated tin oxide-based microhotplate gas sensors”. In: *Sensors and Actuators B: Chemical* 95.1. Selected Papers from Eurosensors XVI, pp. 203 –211. ISSN: 0925-4005. DOI: https://doi.org/10.1016/S0925-4005(03)00420-9. URL: http://www.sciencedirect.com/science/article/pii/S0925400503004209.

Iwamoto, Masakazu et al. (1978). “Study of metal oxide catalysts by temperature programmed desorption. 4. Oxygen adsorption on various metal oxides”. In: *The Journal of Physical Chemistry* 82.24, pp. 2564–2570. DOI: 10.1021/j100513a006. eprint: https://doi.org/10.1021/j100513a006. URL: https://doi.org/10.1021/j100513a006.

Jing, Zhihong and Jinhua Zhan (2008). “Fabrication and Gas-Sensing Properties of Porous ZnO Nanoplates”. In: *Advanced Materials* 20.23, pp. 4547–4551. DOI: 10.1002/adma.200800243. eprint: https://onlinelibrary.wiley.com/doi/pdf/10.1002/adma.200800243. URL: https://onlinelibrary.wiley.com/doi/abs/10.1002/adma.200800243.

Johnson, Curtis D. (1999). *Process Control Instrumentation Technology*. 6th. Upper Saddle River, NJ, USA: Prentice Hall PTR. ISBN: 0139382003.

Jones, A.P. (1999). “Indoor air quality and health”. In: *Atmospheric Environment* 33.28, pp. 4535 –4564. ISSN: 1352-2310. DOI: https://doi.org/10.1016/S1352-2310(99)00272-1. URL: http://www.sciencedirect.com/science/article/pii/S1352231099002721.

Kawakami, Keiichi and Hiroaki Yanagida (1979). “Effects of Water Vapour on the Electrical Conductivity of the Interface of Semiconductor Ceramic-Ceramic Contacts”. In: *Journal of the Ceramic Association, Japan* 87.1002, pp. 112 –115. DOI: 10.2109/jcersj1950.87.1002_112. URL: http://www.sciencedirect.com/science/article/pii/S0925400510008646.

Khlebarov, Zdravko P., Any I. Stoyanova, and Diana I. Topalova (1992). “Surface acoustic wave gas sensors”. In: *Sensors and Actuators B: Chemical* 8.1, pp. 33 –40. ISSN: 0925-4005. DOI: https://doi.org/10.1016/0925-4005(92)85005-H. URL: http://www.sciencedirect.com/science/article/pii/092540059285005H.

Kim, Hae-Ryong et al. (2010). “Ultra-fast responding and recovering C2H5OH sensors using SnO2 hollow spheres prepared and activated by Ni templates”. In: *Chem. Commun.* 46 (28), pp. 5061–5063. DOI: 10.1039/C0CC00213E. URL: http://dx.doi.org/10.1039/C0CC00213E.

Kim, Hae-Ryong et al. (2011a). “The Role of NiO Doping in Reducing the Impact of Humidity on the Performance of SnO2-Based Gas Sensors: Synthesis Strategies, and Phenomenological and Spectroscopic Studies”. In: *Advanced Functional Materials* 21.23, pp. 4456–4463. DOI: 10.1002/adfm.201101154. eprint: https://onlinelibrary.wiley.com/doi/pdf/10.1002/adfm.201101154. URL: https://onlinelibrary.wiley.com/doi/abs/10.1002/adfm.201101154.

Kim, Hyo-Joong and Jong-Heun Lee (2014). “Highly sensitive and selective gas sensors using p-type oxide semiconductors: Overview”. In: *Sensors and Actuators B: Chemical* 192, pp. 607 –627. ISSN: 0925-4005. DOI: https://doi.org/10.1016/j.snb.2013.11.005. URL: http://www.sciencedirect.com/science/article/pii/S0925400513013476.

Kim, Hyo-Joong et al. (2011b). "Template-free solvothermal synthesis of hollow hematite spheres and their applications in gas sensors and Li-ion batteries". In: *J. Mater. Chem.* 21 (18), pp. 6549–6555. DOI: `10.1039/C0JM03516E`. URL: `http://dx.doi.org/10.1039/C0JM03516E`.

Kim, Il-Doo et al. (2006). "Ultrasensitive Chemiresistors Based on Electrospun TiO2 Nanofibers". In: *Nano Letters* 6.9. PMID: 16968017, pp. 2009–2013. DOI: `10.1021/nl061197h`. eprint: `https://doi.org/10.1021/nl061197h`. URL: `https://doi.org/10.1021/nl061197h`.

Kim, Sun-Jung et al. (2012). "One-pot hydrothermal synthesis of CuO–ZnO composite hollow spheres for selective H2S detection". In: *Sensors and Actuators B: Chemical* 168, pp. 83 –89. ISSN: 0925-4005. DOI: `https://doi.org/10.1016/j.snb.2012.01.045`. URL: `http://www.sciencedirect.com/science/article/pii/S0925400512000688`.

Kılıç, Çetin and Alex Zunger (Apr. 2002). "Origins of Coexistence of Conductivity and Transparency in SnO 2". In: *Physical review letters* 88, p. 095501. DOI: `10.1103/PhysRevLett.88.095501`.

Kohl, D. (Oct. 2001). "TOPICAL REVIEW: Function and applications of gas sensors". In: *Journal of Physics D Applied Physics* 34, R125–R149. DOI: `10.1088/0022-3727/34/19/201`.

Kolmakov, A. et al. (2003). "Detection of CO and O2 Using Tin Oxide Nanowire Sensors". In: *Advanced Materials* 15.12, pp. 997–1000. DOI: `10.1002/adma.200304889`. eprint: `https://onlinelibrary.wiley.com/doi/pdf/10.1002/adma.200304889`. URL: `https://onlinelibrary.wiley.com/doi/abs/10.1002/adma.200304889`.

Kolmakov, Andrei and Martin Moskovits (2004). "CHEMICAL SENSING AND CATALYSIS BY ONE-DIMENSIONAL METAL-OXIDE NANOSTRUCTURES". In: *Annual Review of Materials Research* 34.1, pp. 151–180. DOI: `10.1146/annurev.matsci.34.040203.112141`. eprint: `https://doi.org/10.1146/annurev.matsci.34.040203.112141`. URL: `https://doi.org/10.1146/annurev.matsci.34.040203.112141`.

Korotcenkov, G. (Jan. 2005). "Gas response control through structural and chemical modification of metal oxides: State of the art and approaches, G. Korotcenkov, Sens. Actuators B 107(1) (2005) 209-232." In: *Sensors and Actuators B Chemical* 107, pp. 209–232.

— (2008). "The role of morphology and crystallographic structure of metal oxides in response of conductometric-type gas sensors". In: *Materials Science and Engineering: R: Reports* 61.1, pp. 1 –39. ISSN: 0927-796X. DOI: `https://doi.org/10.1016/j.mser.2008.02.001`. URL: `http://www.sciencedirect.com/science/article/pii/S0927796X08000156`.

Korotcenkov, G. and Beongki Cho (Jan. 2011). "Instability of metal oxide-based conductometric gas sensors and approaches to stability improvement, G. Korotcenkov, B.K. Cho, Sens. Actuators B 156 (2011) 527-538." In: *Sensors and Actuators B Chemical* 156, pp. 527–538.

Leidinger, M. et al. (2014). "Selective detection of hazardous VOCs for indoor air quality applications using a virtual gas sensor array". In: *Journal of Sensors and Sensor Systems* 3.2, pp. 253–263. DOI: `10.5194/jsss-3-253-2014`. URL: `https://www.j-sens-sens-syst.net/3/253/2014/`.

Li, Chao et al. (2003). "In2O3 nanowires as chemical sensors". In: *Applied Physics Letters* 82.10, pp. 1613–1615. DOI: `10.1063/1.1559438`. eprint: `https://doi.org/10.1063/1.1559438`. URL: `https://doi.org/10.1063/1.1559438`.

Li, Xiao-Lin et al. (2004). "Highly Sensitive WO3 Hollow-Sphere Gas Sensors". In: *Inorganic Chemistry* 43.17. PMID: 15310226, pp. 5442–5449. DOI: `10.1021/ic049522w`.

eprint: https://doi.org/10.1021/ic049522w. URL: https://doi.org/10.1021/ic049522w.

Lu, Honglang et al. (June 2006). "Micro-Type Powder-Sputtered Thin Film Gas Sensors with Long-Term Stability". In: *2006 IEEE International Conference on Mechatronics and Automation, ICMA 2006* 2006. DOI: 10.1109/ICMA.2006.257619.

Mathur, Sanjay et al. (2005). "Size-Dependent Photoconductance in SnO2 Nanowires". In: *Small* 1.7, pp. 713–717. DOI: 10.1002/smll.200400168. eprint: https://onlinelibrary.wiley.com/doi/pdf/10.1002/smll.200400168. URL: https://onlinelibrary.wiley.com/doi/abs/10.1002/smll.200400168.

Matsuura, Yoshinobu and Kei Takahata (1991). "Stabilization of SnO2 sintered gas sensors". In: *Sensors and Actuators B: Chemical* 5.1, pp. 205 –209. ISSN: 0925-4005. DOI: https://doi.org/10.1016/0925-4005(91)80248-I. URL: http://www.sciencedirect.com/science/article/pii/092540059180248I.

Micone, P.G. and C. Guy (2007). "Odour quantification by a sensor array: An application to landfill gas odours from two different municipal waste treatment works". In: *Sensors and Actuators B: Chemical* 120.2, pp. 628 –637. ISSN: 0925-4005. DOI: https://doi.org/10.1016/j.snb.2006.03.026. URL: http://www.sciencedirect.com/science/article/pii/S0925400506002103.

Moon, Hi Gyu et al. (Aug. 2012). "Self-activated ultrahigh chemosensitivity of oxide thin film nanostructures for transparent sensors". In: *Scientific reports* 2, p. 588. DOI: 10.1038/srep00588.

Morrison, S.R. (1990). *The Chemical Physics of Surfaces*. Ed. by New York Plenum Press. 2nd.

Muñoz, Beth C., Gregory Steinthal, and Steven Sunshine (Jan. 1999). "Conductive polymer-carbon black composites-based sensor arrays for use in an electronic nose". In: 19.4, pp. 300–305. ISSN: 0260-2288. DOI: 10.1108/02602289910294745. URL: https://doi.org/10.1108/02602289910294745.

Na, Chan Woong, Hyung Sik Woo, and Jong Heun Lee (Jan. 2012a). "Design of highly sensitive volatile organic compound sensors by controlling NiO loading on ZnO nanowire networks". English. In: *RSC Advances* 2.2, pp. 414–417. ISSN: 2046-2069. DOI: 10.1039/c1ra01001h.

Na, Chan Woong et al. (2012b). "Transformation of ZnO Nanobelts into Single-Crystalline Mn3O4 Nanowires". In: *ACS Applied Materials & Interfaces* 4.12, pp. 6565–6572. ISSN: 1944-8244.

Nagle H.T., Gutierrez-Osuna R. and S.S. Schiffman (1998). ""The how and why of electronic hoses"". In: *IEEE Spectrum* 35.9, pp. 22–31.

Natale, Corrado et al. (Oct. 2003). "Lung cancer identification by the analysis of breath by means of an array of non-selective gas sensors". In: *Biosensors and bioelectronics* 18, pp. 1209–18. DOI: 10.1016/S0956-5663(03)00086-1.

Neri, Giovanni (Mar. 2015). "First Fifty Years of Chemoresistive Gas Sensors". In: *Chemosensors* 3, pp. 1–20. DOI: 10.3390/chemosensors3010001.

Nguyen, Pho et al. (2003). "Epitaxial Directional Growth of Indium-Doped Tin Oxide Nanowire Arrays". In: *Nano Letters* 3.7, pp. 925–928. DOI: 10.1021/nl0342186. eprint: https://doi.org/10.1021/nl0342186. URL: https://doi.org/10.1021/nl0342186.

Nimmermark, S. (Nov. 2001). "Use of electronic noses for detection of odour from animal production facilities: a review". In: *Water Science and Technology* 44.9, pp. 33–41. ISSN: 0273-1223. DOI: 10.2166/wst.2001.0503. eprint: https://iwaponline.com/wst/article-pdf/44/9/33/424405/33.pdf. URL: https://doi.org/10.2166/wst.2001.0503.

Pearce, T. C. (Tim C.) (2003). *Handbook of machine olfaction : electronic nose technology*. English. Weinheim ; [Cambridge?] : Wiley-VCH. ISBN: 3527303588.

Persaud, Krishna and George Dodd (1982). “Analysis of discrimination mechanisms in the mammalian olfactory system using a model nose”. In: *Nature* 299.5881, pp. 352–355. ISSN: 1476-4687. DOI: 10.1038/299352a0. URL: https://doi.org/10.1038/299352a0.

Potyrailo, Radislav A. (2016). “Multivariable Sensors for Ubiquitous Monitoring of Gases in the Era of Internet of Things and Industrial Internet”. In: *Chemical Reviews* 116.19. PMID: 27602947, pp. 11877–11923. DOI: 10.1021/acs.chemrev.6b00187. eprint: https://doi.org/10.1021/acs.chemrev.6b00187. URL: https://doi.org/10.1021/acs.chemrev.6b00187.

Rajamaki, Tiina et al. (Mar. 2005). “An Electronic Nose and Indicator Volatiles for Monitoring of the Composting Process”. In: *Water, Air, and Soil Pollution* 162.1, pp. 71–87. ISSN: 1573-2932. DOI: 10.1007/s11270-005-5994-8. URL: https://doi.org/10.1007/s11270-005-5994-8.

Reimann, Peter and Andreas Schütze (June 2013). “Sensor Arrays, Virtual Multisensors, Data Fusion, and Gas Sensor Data Evaluation”. In: pp. 67–107. DOI: 10.1007/5346_2013_52.

Rock, Frank, Nicolae Barsan, and Udo Weimar (2008). “Electronic Nose: Current Status and Future Trends”. In: *Chemical Reviews* 108.2. PMID: 18205411, pp. 705–725. DOI: 10.1021/cr068121q. URL: https://doi.org/10.1021/cr068121q.

Schaller, Emmanuelle, Jacques O. Bosset, and Felix Escher (1998). “‘Electronic Noses’ and Their Application to Food”. In: *LWT - Food Science and Technology* 31.4, pp. 305 –316. ISSN: 0023-6438. DOI: https://doi.org/10.1006/fstl.1998.0376. URL: http://www.sciencedirect.com/science/article/pii/S0023643898903760.

Schütze, Andreas et al. (2017). “Highly Sensitive and Selective VOC Sensor Systems Based on Semiconductor Gas Sensors: How to?” In: *Environments* 4.1. ISSN: 2076-3298. DOI: 10.3390/environments4010020. URL: https://www.mdpi.com/2076-3298/4/1/20.

Segantini, Matteo (2017). “Nanostructure-based Sensor Arrays for Organic Volatile Compound Fingerprinting”. MA thesis. Politecnico di Torino, Grenoble INP - Phelma, Ecole Polytechnique Fédérale de Lausanne.

Seiyama, Tetsuro et al. (Oct. 1962). “A New Detector for Gaseous Components Using Semiconductive Thin Films.” In: *Analytical Chemistry* 34.11, pp. 1502–1503. DOI: 10.1021/ac60191a001. URL: https://doi.org/10.1021/ac60191a001.

Shaver, P. J. (Oct. 1967). “ACTIVATED TUNGSTEN OXIDE GAS DETECTORS”. In: *Applied Physics Letters* 11.8, pp. 255–257. DOI: 10.1063/1.1755123. URL: https://doi.org/10.1063/1.1755123.

Shurmer, Harold V. and Julian W. Gardner (1992). “Odour discrimination with an electronic nose”. In: *Sensors and Actuators B: Chemical* 8.1, pp. 1 –11. ISSN: 0925-4005. DOI: https://doi.org/10.1016/0925-4005(92)85001-D. URL: http://www.sciencedirect.com/science/article/pii/092540059285001D.

Sputter Deposition. Accessed: 2019-09-09. URL: http://clearmetalsinc.com/technology/.

Straumal, B. et al. (2009). “Increase of Mn solubility with decreasing grain size in ZnO”. In: *Journal of the European Ceramic Society* 29.10, pp. 1963–1970.

Sysoev, Victor V. et al. (2007). “A Gradient Microarray Electronic Nose Based on Percolating SnO2 Nanowire Sensing Elements”. In: *Nano Letters* 7.10. PMID: 17924710, pp. 3182–3188. DOI: 10.1021/nl071815+. eprint: https://doi.org/10.1021/nl071815+. URL: https://doi.org/10.1021/nl071815+.

Taguchi, Naoyoshi. *Gas Detecting Device*. Application No. US3695848DA, Filed Apr 7th., 1970, Issued Mar. 10th., 1972.

Tamaki, Jun et al. (1992). “CuO-SnO2 element for highly sensitive and selective detection of H2S”. In: *Sensors and Actuators B: Chemical* 9.3, pp. 197 –203. ISSN: 0925-4005. DOI: `https://doi.org/10.1016/0925-4005(92)80216-K`. URL: `http://www.sciencedirect.com/science/article/pii/092540059280216K`.

Thevenin, P.O et al. (Apr. 2001). “Deactivation of high temperature combustion catalysts”. In: *Applied Catalysis A: General* 212, pp. 189–197. DOI: `10.1016/S0926-860X(00)00846-2`.

Thornquist, Lisa (2019). “SPUTTERED P-TYPE ON N-TYPE THIN FILM MOS SENSORS FOR VOC SENSING”. MA thesis. San José State University.

Tricoli, Antonio, Markus Graf, and Sotiris E. Pratsinis (2008). “Optimal Doping for Enhanced SnO2 Sensitivity and Thermal Stability”. In: *Advanced Functional Materials* 18.13, pp. 1969–1976. DOI: `10.1002/adfm.200700784`. eprint: `https://onlinelibrary.wiley.com/doi/pdf/10.1002/adfm.200700784`. URL: `https://onlinelibrary.wiley.com/doi/abs/10.1002/adfm.200700784`.

Tsow, Francis et al. (Jan. 2010). “A Wearable and Wireless Sensor System for Real-Time Monitoring of Toxic Environmental Volatile Organic Compounds”. In: *Sensors Journal, IEEE* 9, pp. 1734 –1740. DOI: `10.1109/JSEN.2009.2030747`.

Védrine, Jacques (Nov. 2016). “Heterogeneous catalytic partial oxidation of lower alkanes (C 1 –C 6) on mixed metal oxides”. In: *Journal of Energy Chemistry* 25.6, pp. 936–946. DOI: `10.1016/j.jechem.2016.10.007`. URL: `https://hal.sorbonne-universite.fr/hal-02188605`.

Walt, David R et al. (1998). “Optical sensor arrays for odor recognition”. In: *Biosensors and Bioelectronics* 13.6, pp. 697 –699. ISSN: 0956-5663. DOI: `https://doi.org/10.1016/S0956-5663(98)00024-4`. URL: `http://www.sciencedirect.com/science/article/pii/S0956566398000244`.

Wan, Q. et al. (2004). “Fabrication and ethanol sensing characteristics of ZnO nanowire gas sensors”. In: *Applied Physics Letters* 84.18, pp. 3654–3656. DOI: `10.1063/1.1738932`. eprint: `https://doi.org/10.1063/1.1738932`. URL: `https://doi.org/10.1063/1.1738932`.

Wang, Qinglei et al. (2007). “Grain boundary blocking and segregation effects in yttrium-doped polycrystalline titanium dioxide”. In: *Solid State Ionics* 178.3, pp. 187 –194. ISSN: 0167-2738. DOI: `https://doi.org/10.1016/j.ssi.2006.12.006`. URL: `http://www.sciencedirect.com/science/article/pii/S0167273806007223`.

Wang, Tie-Shi et al. (2012). “Synthesis and enhanced H2S gas sensing properties of Alpha-MoO3/CuO p–n junction nanocomposite”. In: *Sensors and Actuators B: Chemical* 171-172, pp. 256 –262. ISSN: 0925-4005. DOI: `https://doi.org/10.1016/j.snb.2012.03.058`. URL: `http://www.sciencedirect.com/science/article/pii/S0925400512003218`.

Wilson, Alphus Dan (2012). “Review of Electronic-nose Technologies and Algorithms to Detect Hazardous Chemicals in the Environment”. In: *Procedia Technology* 1. First World Conference on Innovation and Computer Sciences (INSODE 2011), pp. 453 –463. ISSN: 2212-0173. DOI: `https://doi.org/10.1016/j.protcy.2012.02.101`. URL: `http://www.sciencedirect.com/science/article/pii/S2212017312001028`.

Woo, Hyung-Sik et al. (June 2012). “Highly sensitive and selective trimethylamine sensor using one-dimensional ZnO–Cr2O3 hetero-nanostructures”. In: *Nanotechnology* 23, pp. 245–501. DOI: `10.1088/0957-4484/23/24/245501`.

World Health Organization. WHO Guidelines for Indoor Air Quality: Selected Pollutants. Accessed: 2019-09-18. URL: `http://www.euro.who.int/__data/assets/pdf_file/0009/128169/e94535.pdf`.

Xie, Lu (2013). “Simulations of plasma sputtering deposition and thin film growth”. English. Tesi di laurea. Université d’Orléans.

Yamazoe, Noboru and Kengo Shimanoe (Jan. 2008). “Theory of power laws for semiconductor gas sensors”. English. In: *Sensors and Actuators, B: Chemical* 128.2, pp. 566–573. ISSN: 0925-4005. DOI: `10.1016/j.snb.2007.07.036`.

Yang, P. et al. (May 2002). “Controlled growth of ZnO nanowires and their optical properties”. English. In: *Advanced Functional Materials* 12.5, pp. 323–331. ISSN: 1616-301X. DOI: `10.1002/1616-3028(20020517)12:5<323::AID-ADFM323>3.0.CO;2-G`.

Zhang, Daihua et al. (2004). “Detection of NO2 down to ppb Levels Using Individual and Multiple In2O3 Nanowire Devices”. In: *Nano Letters* 4.10, pp. 1919–1924. DOI: `10.1021/nl0489283`. eprint: `https://doi.org/10.1021/nl0489283`. URL: `https://doi.org/10.1021/nl0489283`.

Zhang, Lei et al. (Nov. 2012). “Classification of multiple indoor air contaminants by an electronic nose and a hybrid support vector machine”. In: *Sensors and Actuators B: Chemical* 174, 114–125. DOI: `10.1016/j.snb.2012.07.021`.

Zhou, Xiaohua et al. (2001). “Sensing behavior and mechanism of La2CuO4–SnO2 gas sensors”. In: *Sensors and Actuators B: Chemical* 77.1. Proceeding of the Eighth International Meeting on Chemical Sensors IMCS-8 - Part 2, pp. 443 –446. ISSN: 0925-4005. DOI: `https://doi.org/10.1016/S0925-4005(01)00721-3`. URL: `http://www.sciencedirect.com/science/article/pii/S0925400501007213`.